

National Formosa University  
Department of Electro-Optical Engineering  
Doctoral Dissertation

Design of Bipolar Optical Code Division Multiple  
Access Techniques Using Phase Modulator for  
Polarization Coding in Wireless Optical  
Communication  
無線光通信中使用相位調製器極化編碼的雙極光碼  
分多址技術的設計

Graduate Student: Eddy Wijanto  
Advisor: 1. Prof. Hsu-Chih Cheng  
2. Prof. Chun-Ming Huang

June, 2021  
Huwei, Yunlin, Taiwan, Republic of China

Design of Bipolar Optical Code Division Multiple Access  
Techniques Using Phase Modulator for Polarization Coding in  
Wireless Optical Communication  
無線光通信中使用相位調製器極化編碼的雙極光碼分多址  
技術的設計

Graduate Student: 陳漢龍 (Eddy Wijanto)

Advisor: 1. 鄭旭志 (Prof. Hsu-Chih Cheng)

2. 黃俊銘 (Prof. Chun-Ming Huang)

National Formosa University  
Department of Electro-Optical Engineering  
Doctoral Dissertation

A Dissertation Submitted to Department of Electro-Optical Engineering  
College of Electrical and Computer Engineering  
National Formosa University  
in Partial Fulfillment of the Requirements  
for the Degree of Doctor of Philosophy  
in  
Electro-Optical Engineering

June 11<sup>th</sup>, 2021  
Huwei, Yunlin, Taiwan, Republic of China

# National Formosa University

## Oral Examination Committee Verification

Department of Electro-Optical Engineering

Mr. Eddy Wijanto

Dissertation Title: Design of Bipolar Optical Code Division Multiple Access Techniques Using Phase Modulator for Polarization Coding in Wireless Optical Communication

Fulfill the Doctoral's Requirement; reviewed and verified by this committee.

Oral Examination Committee Members:

張耀堂 Chang, Yao Tang	
曾信賓	顏志達
鄭旭志	黃俊銘

Advisor: 鄭旭志 Cheng, Hsu-Chih  
黃俊銘 Huang, Chun-Ming

Head of Dept.:



2021 / 06 / 11

# Design of Bipolar Optical Code Division Multiple Access Techniques Using Phase Modulator for Polarization Coding in Wireless Optical Communication

Student : Eddy Wijanto

Advisors: Professor Hsu-Chih Cheng

Advisors: Professor Chun-Ming Huang

Department of Electro-Optical Engineering

National Formosa University

## Abstract

In this dissertation, bipolar optical code division multiple access (Bi-OCDMA) technique based on spectral amplitude coding (SAC) was proposed by using phase modulator to realize the polarization coding through the free-space optical channel. The proposed Bi-OCDMA system was designed to improve the transmission rate and system performance of previous Bi-OCDMA structure with optical switch and dual electro-optical modulator (EOM). The model was investigated by simulating with OptiSystem. First simulation aims to verify the feasibility of bipolar scheme of the proposed structure by utilizing modified M-sequence as signature code. Noises in optical communication system, such as amplified spontaneous emission (ASE) noise, thermal noise, and shot noise, were included in the simulation to approach the real application. The initial simulation results exhibit that the proposed Bi-OCDMA system could be implemented in the free-space optical communication. The structure of the proposed system alleviates the multiple access interference (MAI). The second simulation observed the performance of several different well-known SAC codes, i.e., MD code, MQC

code, modified M-sequence code, and Walsh-Hadamard code, with the proposed Bi-OCDMA architecture for two users in different weather conditions, both for additive white Gaussian noise (AWGN) and turbulence-induced fading channel. The simulation results indicated that Walsh-Hadamard code has the superior performance among other codes. The simulations also show that MD code can be implemented in the proposed Bi-OCDMA scheme for medium distance FSO application. In the extreme weather condition, Walsh-Hadamard code suffered the highest performance degradation with the increase of FSO range.

Keywords: bipolar, free-space optical communication, multiple access interference (MAI), optical code division multiple access (OCDMA), phase modulator, polarization coding



National Formosa University

# 無線光通信中使用相位調製器極化編碼的雙極光碼分多址技術的設計

學生：陳漢龍

指導教授：鄭旭志  
黃俊銘

國立虎尾科技大學光電工程系光電與材料科技博士班

## 摘要

在這篇論文中提出了一種基於頻譜幅度編碼 (SAC) 的雙極光碼分多址 (Bi-OCDMA) 技術，該技術通過使用相位調製器來實現通過自由空間光信道的偏振編碼。提出的 Bi-OCDMA 系統旨在通過光開關和雙電光調製器 (EOM) 來提高以前的 Bi-OCDMA 結構的傳輸速率和性能。通過使用 OptiSystem 進行模擬，進而研究了該模型。首次模擬旨在通過使用修改後的 M 序列作為簽名代碼來驗證所提出方法的雙極方案的可行性。模擬中包括各種類型的噪聲，例如放大的自發發射 (ASE) 噪聲，熱噪聲和散粒噪聲，以貼近實際應用。初步的模擬結果顯示，所提出的 Bi-OCDMA 系統可以在自由空間光通信中實現。所提出的系統的結構設計減輕了多址干擾 (MAI)。第二次模擬觀察了幾種不同的著名 SAC 代碼 (MD 代碼，MQC 代碼，修改的 M 序列代碼和 Walsh-Hadamard 代碼) 的性能，並針對不同天氣條件下的兩個使用者採用了建議的 Bi-OCDMA 架構，既適用於加性高斯白噪聲 (AWGN)，也適用於湍流引起的衰弱通道。模擬結果顯示，Walsh-Hadamard 代碼具有比其他代碼更好的性能。模擬結果也顯示，在中

等的 FSO 應用中，可以在所提出的 Bi-OCDMA 方案中實現 MD 碼。在極端天氣條件下，隨著 FSO 範圍的增加，Walsh-Hadamard 碼的性能衰退幅度最大。

關鍵詞：雙極性，自由空間光通信，多址干擾 (MAI)，光碼分多址 (OCDMA)，相位調製器，偏振編碼

國立虎尾科技大學



National Formosa University

## Acknowledgements

The First and foremost, gratefully praises to the God, the Almighty, for His unlimited love and blessings throughout my study and research work until the successfully completion of my dissertation entitled Design of Bipolar Optical Code Division Multiple Access Techniques Using Phase Modulator for Polarization Coding in Wireless Optical Communication.

I would like to express my sincere gratefulness to my Supervisor, Prof. Hsu-Chih Cheng, Professor and Chairman of Department of Electro-Optical Engineering, National Formosa University, Taiwan, Republic of China, for the opportunity to join the research and providing precious guidance from the beginning until the completion of this research. His vision, innovation, and motivation have deeply inspired me. It was a great privilege and honor to study under his guidance. I also would like to thank my Co-Supervisor, Prof. Chun-Ming Huang, for his caring and patience help during the discussion on research work and dissertation preparation.

I also would like to thank the Ministry of Education, Taiwan, Republic of China, who has given me a scholarship as a lecturer in south east Asia countries through the Elite Lecturer Scholarship program. I would like to express my gratitude to Prof. Shou-Yin Yang, Dean of Office of International Affairs, National Formosa University and Dr. Jui-Lin Lee, Director of International Students Affairs, National Formosa University, and all of Office of International Affairs staffs for the assistance, guidance, and great help given for international student so that everything runs smoothly during my study. My special thanks go to Prof. Wen-Kai Kuo, former Dean of Office of International Affairs, National Formosa University, who has introduced National Formosa University to me, also for his kindly help and support during my study at National Formosa University.

I am extremely grateful to my wife, Lince Terang, for her love, prayers, patient, care, and continuing support to complete this dissertation. Also, I express




my thanks to all of my family for their prayers and valuable support.

I would like to thank to Krida Wacana Christian University, the university where I work in Indonesia, which has provided the opportunity for me to continue my studies at National Formosa University. First, my gratitude and appreciation go to late Pdt. Em. Dr. Aristarchus Sukarto, B.A., M.Th, former Rector of Krida Wacana Christian University for his support and motivation to always learn and develop myself and continue to doctoral studies. I also would like to express my gratitude and appreciation to Dr. Amelia Makmur, S.T., M.T., former Vice Rector I, Krida Wacana Christian University, for all of her continuing support and help as my leader and as my friend. I also would like to thank Dr. dr. Wani Devita Gunardi, Sp.MK (K), Rector of Krida Wacana Christian University, Dr. Oki Sunardi, Dean of Faculty of Engineering and Computer Science, Krida Wacana Christian University, and Indra Karnadi, Ph.D, Chairman of Electrical Engineering Department, Krida Wacana Christian University for their supports.

Finally, my appreciation also go to all the people, who is directly or indirectly, have supported me to accomplish the research and finish this dissertation work.

Huwei, Yunlin, Taiwan, R.O.C.

June 2021



Eddy Wijanto

# Table of Contents

English Abstract .....	i
Chinese Abstract .....	iii
Acknowledgement .....	v
Table of Contents .....	vii
List of Tables .....	viii
List of Figures .....	ix
Chapter 1 Introduction.....	1
1.1 Research Background .....	1
1.2 Research Motivation .....	4
1.3 Research Objectives .....	7
1.4 Dissertation Structure .....	7
Chapter 2 General Concept and Literature Review.....	9
2.1 General Concept.....	9
2.1.1 Laser.....	9
2.1.2 Optical Coupler.....	13
2.1.3 Modulator.....	15
2.1.4 Erbium Doped Fiber Amplifier.....	19
2.1.5 Optical Switch.....	20
2.1.6 Optical Polarizer.....	22
2.1.7 Fiber Gratings.....	27
2.1.8 Optical Circulator.....	30
2.1.9 Photodetector.....	32
2.2 Literature Review.....	38
Chapter 3 Design and Simulation Setup of The Proposed Bipolar OCDMA Scheme.....	54
3.1 Design of Bipolar OCDMA System with Phase Modulator Scheme....	54
3.2 Simulation setup of bipolar OCDMA system with phase modulator scheme.....	62
3.2.1 Components of bipolar OCDMA system with phase modulator scheme	62
3.2.2 Noises and Channel Model of Bipolar OCDMA System.....	74
Chapter 4 Simulation Results and Analysis of The Proposed Bipolar OCDMA Scheme.....	79
4.1 Feasibility of Bipolar OCDMA System with Phase Modulator Scheme for Single-User.....	79
4.2 Performance of Bipolar OCDMA System with Phase Modulator Scheme for Multi-User in Different Channel Condition.....	102
Chapter 5 Conclusion.....	116
Reference .....	118
Extended Abstract .....	

## List of Tables

Table 3.1	Modified M-sequence codes of length 8 with spectral polarization coding.....	56
Table 3.2	Components for single-user bipolar OCDMA simulation.....	63
Table 3.3	Simulation parameters.....	73
Table 3.4	International visibility code.....	77
Table 3.5	Signature code for two users.....	77
Table 4.1	Performance degradation with the increasing of FSO range in AWGN channel.....	108
Table 4.2	Performance degradation with the increasing of FSO range in AWGN and turbulence-induced fading channel..	112
Table 4.3	Performance degradation with the increasing of FSO range in different turbulence condition.....	115

National Formosa University

## List of Figures

Figure 2.1	Laser concepts.....	10
Figure 2.2	Laser types (a) Continuous wave laser, (b) Pulsed laser.....	12
Figure 2.3	Optical coupler scheme.....	14
Figure 2.4	Modulation type (a) Direct modulation, (b) External modulation.....	16
Figure 2.5	Phase modulation.....	18
Figure 2.6	EDFA principle.....	20
Figure 2.7	P- and S-polarizations.....	23
Figure 2.8	Linear polarization.....	24
Figure 2.9	Circular polarization.....	24
Figure 2.10	Elliptical polarization.....	25
Figure 2.11	FBG principle.....	29
Figure 2.12	Optical circulator structure.....	30
Figure 2.13	Optical circulator principle.....	31
Figure 2.14	Photoelectric effect.....	32
Figure 2.15	PIN photodiode structure.....	34
Figure 2.16	APD photodiode structure.....	35
Figure 3.1	Proposed Bi-OCDMA encoder with phase modulator scheme.....	57
Figure 3.2	Proposed Bi-OCDMA decoder with phase modulator scheme.....	60
Figure 3.3	Proposed Bi-OCDMA system with phase modulator scheme for two users.....	62
Figure 3.4	Polarization splitter structure.....	67
Figure 3.5	Polarization combiner structure.....	68

Figure 4.1	Output from bit sequence generator when bit “0” was transmitted.....	80
Figure 4.2	CW laser array spectra (a) Upper CW laser array, (b) Lower CW laser array.....	80
Figure 4.3	Output from PSK pulse generator when bit “0” was transmitted (a) Upper PSK pulse generator, (b) Lower PSK pulse generator.....	81
Figure 4.4	Output from electrical bias when bit “0” was transmitted (a) Upper electrical bias, (b) Lower electrical bias.....	82
Figure 4.5	Output from electrical gain when bit “0” was transmitted (a) Upper electrical gain, (b) Lower electrical gain.....	82
Figure 4.6	Spectra measured after modulated with phase modulator when bit “0” was transmitted (a). Upper phase modulator, (b) Lower phase modulator.....	83
Figure 4.7	Spectra observed after coupling with upper optical coupler#2 when bit “0” was transmitted (a) Port#1, (b) Port#2.....	83
Figure 4.8	Spectra after coupling with lower optical coupler#2 when bit “0” was transmitted (a) Port#1, (b) Port#2.....	84
Figure 4.9	Encoded spectra after polarization splitting when bit “0” was transmitted (a) Horizontal polarization at upper side, (b) Vertical polarization at upper side, (c) Horizontal polarization at lower side, (d) Vertical polarization at lower side.....	85
Figure 4.10	Spectra after combined with polarization combiner when bit “0” was transmitted.....	86
Figure 4.11	Spectra after passing through free-space optics channel	

	when bit “0” was transmitted.....	86
Figure 4.12	Output spectra after polarization splitting when bit “0” was transmitted (a) Horizontal polarization, (b) Vertical polarization.....	87
Figure 4.13	Output spectra before photodetection when bit “0” was transmitted (a) Horizontal polarization at upper branch, (b) Vertical polarization at upper branch, (c) Total signals at upper branch, (d) Horizontal polarization at lower branch, (e) Vertical polarization at lower branch, (f) Total signals at lower branch.....	88
Figure 4.14	Output electrical signals of the proposed Bi-OCDMA system when bit “0” was transmitted (a) Separated electrical and noise signals, (b) Combined electrical and noise signals.....	89
Figure 4.15	Output from bit sequence generator when bit “1” was transmitted.....	89
Figure 4.16	Output from PSK pulse generator when bit “1” was transmitted (a) Upper PSK pulse generator, (b) Lower PSK pulse generator.....	90
Figure 4.17	Output from electrical bias when bit “1” was transmitted (a) Upper electrical bias, (b) Lower electrical bias.....	91
Figure 4.18	Output from electrical gain when bit “1” was transmitted (a) Upper electrical gain, (b) Lower electrical gain.....	91
Figure 4.19	Spectra measured after modulated with phase modulator when bit “1” was transmitted (a) Upper phase modulator, (b) Lower phase modulator.....	92
Figure 4.20	Spectra after coupling with upper optical coupler#2 when bit “1” was transmitted (a) Port#1, (b)	

	Port#2.....	93
Figure 4.21	Spectra after coupling with lower optical coupler#2 when bit “1” was transmitted (a) Port#1, (b) Port#2.....	93
Figure 4.22	Encoded spectra after polarization splitting when bit “1” was transmitted (a) Horizontal polarization at upper side, (b) Vertical polarization at upper side, (c) Horizontal polarization at lower side, (d) Vertical polarization at lower side.....	94
Figure 4.23	Spectra after combined with polarization combiner when bit “1” was transmitted.....	95
Figure 4.24	Spectra after passing through free-space optics channel when bit “1” was transmitted.....	95
Figure 4.25	Output spectra after polarization splitting when bit “1” was transmitted (a) Horizontal polarization, (b) Vertical polarization.....	96
Figure 4.26	Output spectra before photodetection when bit “1” was transmitted (a) Horizontal polarization at upper branch, (b) Vertical polarization at upper branch, (c) Total signals at upper branch, (d) Horizontal polarization at lower branch, (e) Vertical polarization at lower branch, (f) Total signals at lower branch.....	97
Figure 4.27	Output electrical signals of the proposed Bi-OCDMA system when bit “1” was transmitted (a) Separated electrical and noise signals, (b) Combined electrical and noise signals.....	98
Figure 4.28	Binary sequence generated from PRBS.....	99
Figure 4.29	Output signals from the proposed bi-OCDMA system	

	without noise.....	99
Figure 4.30	Output signals from the proposed bi-OCDMA system with the effects of noise.....	100
Figure 4.31	Output spectra before photodetection for mismatch decoder when bit “0” was transmitted (a) Total signals at upper branch, (b) Total signals at lower branch.....	100
Figure 4.32	Output electrical signals of the proposed Bi-OCDMA system for mismatch decoder when bit “0” was transmitted.....	101
Figure 4.33	Performance of the proposed system in AWGN channel with different input power (a) Min. Log of BER, (b) Max. Q-Factor.....	103
Figure 4.34	Performance of the proposed system in AWGN and turbulence-induced fading channel with different input power (a) Min. Log of BER, (b) Max. Q-Factor.....	103
Figure 4.35	Performance of photodetector in AWGN channel (a) Min. Log of BER, (b) Max. Q-Factor.....	104
Figure 4.36	Performance of photodetector in AWGN and turbulence-induced fading channel (a) Min. Log of BER, (b) Max. Q-Factor.....	105
Figure 4.37	Performance of the proposed system in drizzle weather condition for AWGN channel (a) Min. Log of BER, (b) Max. Q-Factor.....	105
Figure 4.38	Performance of the proposed system in light rain weather condition for AWGN channel (a) Min. Log of BER, (b) Max. Q-Factor.....	106
Figure 4.39	Performance of the proposed system in average rain weather condition for AWGN channel (a) Min. Log of	



	BER, (b) Max. Q-Factor.....	106
Figure 4.40	Performance of the proposed system in strong rain weather condition for AWGN channel (a) Min. Log of BER, (b) Max. Q-Factor.....	107
Figure 4.41	Performance of the proposed system in storm weather condition for AWGN channel (a) Min. Log of BER, (b) Max. Q-Factor.....	107
Figure 4.42	Performance of the proposed system in drizzle weather condition for AWGN and turbulence-induced fading channel (a) Min. Log of BER, (b) Max. Q-Factor.....	109
Figure 4.43	Performance of the proposed system in light rain weather condition for AWGN and turbulence-induced fading channel (a) Min. Log of BER, (b) Max. Q-Factor.....	110
Figure 4.44	Performance of the proposed system in average rain weather condition for AWGN and turbulence-induced fading channel (a) Min. Log of BER, (b) Max. Q-Factor.....	110
Figure 4.45	Performance of the proposed system in strong rain weather condition for AWGN and turbulence-induced fading channel (a) Min. Log of BER, (b) Max. Q-Factor.....	111
Figure 4.46	Performance of the proposed system in storm weather condition for AWGN and turbulence-induced fading channel (a) Min. Log of BER, (b) Max. Q-Factor.....	111
Figure 4.47	Performance of the proposed system in weak turbulence condition (a) Min. Log of BER, (b) Max. Q-Factor.....	113
Figure 4.48	Performance of the proposed system in medium turbulence condition (a) Min. Log of BER, (b) Max. Q-	

	Factor.....	114
Figure 4.49	Performance of the proposed system in strong turbulence condition (a) Min. Log of BER, (b) Max. Q-Factor.....	114

國立虎尾科技大學



National Formosa University

# Chapter 1 Introduction

## 1.1 Research Background

The fifth generation (5G) network development requires millisecond end-to-end round-trip latency, high speed connection, large bandwidth, accurate synchronization, high reliability, and operating with a fairly low-cost from a commercial point of view. From 2010 to 2030, the rapidly growth of data traffic (almost 20,000 times) has driven the requirements for communication network technology to provide higher coverage and availability as well as denser networks [1]. The upcoming networks also need to support continuous development of new applications, such as machine to machine (M2M) and internet of things (IoT) applications, including smart home, smart city, e-health, telemedicine, autonomous vehicles, surveillance systems, and virtual reality platforms.

First developed in the 1970s, with the nature of small size, light weight, high bandwidth, longer distance, low latency, resistance to electromagnetic interference, precise synchronization, high reliability, low security risk, and flexible application, optical fiber network becomes one of the prospective technologies to fulfil the increasing demands of the 5G technology. The optical fiber network exhibits a small-time delay because light transmission is high-speed, which improves the propagation delay. With a low attenuation, optical fibers also minimize the need to process and repeat signal transmissions. Nevertheless, in the last mile application, optical fiber cables become high-cost options for users since the complex installation and the need of special equipment.

With the limitation of wired optical networks, free-space optical (FSO) communication which is first developed in the 1960s has become one of the alternative technologies. FSO communication combines the advantages of wireless communication and fiber optic communication. Invisible beams of light are used in FSO to provide optical connections with comparable data rates and

very low error rates compared to optical fiber. FSO communication is a line-of-sight wireless communication scheme designed with short optical links, typically in the range from 200 to 2000 m [2]. On the communications side, the FSO technology is considered as a part of the wireless optical communications applications. FSO is being proposed as a 5G backhaul and fronthaul solution because of its ability to transmit massive amounts of data at extremely high speeds. Another supplementary benefit of FSO is the built-in security where FSO is basically a narrow beam of light, so that it is very difficult to detect and therefore difficult to intercept. The drawback of the FSO is power attenuation due to the atmospheric turbulence under various weather conditions and does not work well when there is a rain or dense fog.

An essential part of a FSO system to support dense network is multiplexing techniques, which enable multiple users transmitting data through a single link. Wavelength division multiplexing (WDM) is the common multiplexing technology in optical communication system. WDM utilizes different light wavelengths to send data over the same channel. Along with the advantageous of its simplicity, WDM has limitation in the spectral dispersion.

Time division multiplexing (TDM) is another way to implement effective spectrum sharing for multi-user scheme in optical networks. In this technique, a single channel or band is divided into time slots. TDM usually benefit for compressed video and other high-speed data with the limitation of complex implementation due to synchronization. TDM also sensitive to narrowband fading effect in the channel.

Further method to increase the utilization of the bandwidth is optical code division multiple access (OCDMA). This technology enables multiple users to use the same wavelength with different signature code. In OCDMA, the available channel bandwidth can be accessed in same portion by users. Consequently, the available resources of the network can be equally shared between the OCDMA system users. OCDMA employs a variety of optical codes to allow for the rapid

introduction of new services for various forms of traffic. It is possible to set different code rates for high and low priority traffic. Therefore, OCDMA plays a critical role in providing users with value-added services.

The OCDMA demodulation scheme can be divided into two categories: non-coherent OCDMA and coherent OCDMA. For encoding optical signals, the non-coherent OCDMA system uses light intensity. Unipolar encoding is the most commonly used in the non-coherent OCDMA system, which has the characteristics of simple design and low-cost; however, this scheme only works with low data rate, for example voice data. Meanwhile, coherent systems use a matching filter to adjust the phase of an optical signal to encode the input light phase. The auto-correlation intensity peak in the coherent system after the square-law detection with the photodetector is superior over the non-coherent scheme, remarks the excellent correlation properties of coherent OCDMA. The coherent systems utilizing bipolar encoding which is suitable to be used for high-rate transmission in spectral amplitude code (SAC) OCDMA systems. Due to the pseudo-orthogonality of bipolar codes, the value of a cross-correlation function between any two codewords can be approximated to 0, resulting in low multiple access interference (MAI) and improved system performance. The major shortage of bipolar codes is the needs of matching filter for controlling the optical phase. Hence, a simple and low-cost bipolar OCDMA scheme is needed.

Meanwhile, for transmission over an atmospheric turbulence channel, polarization state of a light beam is the most stable parameter compared with the amplitude and phase [3]. Polarization domain has the potential to improve both the system capacity and the spectral efficiency (SE) by utilizing the state of polarization (SOP) of light [4]. The SOP is also unaffected by atmospheric turbulence, making it resistant to scintillation and allowing for higher data transmission rates with lower BER. OCDMA with spectral-polarization coding (SPC) provides high immunity to laser phase noise and frequency chirp, as well as effective suppression of phase-induced intensity noise (PIIN).

For the modulation, there are many types of modulation techniques has been introduced, one of them is phase modulation (PM), which is one of the modulation techniques that encodes a message signal in form of instantaneous phase variations of a carrier wave. Phase modulator is the simplest electro-optical modulator (EOM) with the superiority in improving the immunity toward the noise to improve the overall system performance.

## **1.2 Research Motivation**

The demand for communication networks with high bandwidth, high data rates, and high quality has steadily increased over the last few decades. In comparison to conventional communication channels, such as copper, optical fiber has the enormous property of high bandwidth and high data rates. The optical fiber is light in weight and has a low data loss rate, resulting in higher data quality.

The basic principle of optical fiber communication is to transform an electrical signal into an optical signal and then transmit it via an optical fiber. The optical signal is converted back to an electrical signal at the receiving-end. With the limitation of optical fiber, wireless optical communication become prospective option, which mainly changes the medium from optical fiber to air, and uses visible or invisible light as the carrier wave to transmit data, voice, and images wirelessly. FSO communication is a secured and cost-effective method by using a broad bandwidth on an unregulated spectrum technique. FSO links have a number of advantages, including the unlicensed spectrum availability, high-speed links, large channel capacity, wide bandwidth, low beam divergence, no electromagnetic and radio frequency (RF) interference, highly secure information transmission, enterprise connectivity, and last mile access with relatively lower cost.

In the late of 1980, the OCDMA techniques, which is a technology combining code division multiple access (CDMA) technology and optical fiber communication technology, has been proposed for optical access network to accommodate more spectral bandwidth and a large number of users. Recently,

OCDMA increasingly attract many researchers. The OCDMA system employs optical orthogonality coding technology for each channel, ensuring that each user has their own unique code and that there is no interference between them. OCDMA is a multiplexing technique based on the principle of spectrum spreading, which enables power to be distributed across a wide frequency band and spread the transmitted signal into a noise like, that is difficult to detect by unintended receivers, ensuring the security of the OCDMA system. The OCDMA attracts the attention in regard to its ability to overcome the bottleneck problem for large data applications with massive data rate. Moreover, the users' interferences that affecting the performance of an OCDMA system can be reduced with the orthogonality of the code sequences. Another advantage of this method is that it simultaneously exploits overall bandwidth, which improve the available resources management. Shot noise, beat noise, thermal noise, and MAI, all of which exist among multiple users, limit the performance of the OCDMA system, with MAI being the most dominant source of noise. The most important OCDMA technique in high-speed optical networks is SAC, since there are no frequency or time synchronizations, which makes it a flexible coding scheme. The SAC technique is a proficient scheme in relieving the effects of MAI and its intensity noise. Broadband incoherent sources, such as light emitting diodes (LED), are commonly used for the SAC-OCDMA. This scheme allows for a greater number of active users than available wavelengths. Furthermore, this system provides a more attractive approach for asynchronous and burst environments. By using codes with defined in-phase cross-correlation  $\lambda$ , the SAC technique effectively eliminates the influence of MAI.

The problems of MAI can be overcome by designing optimal codes and deploying suitable architectures to support large number of users. Numerous code schemes, such as maximum length sequence (M-sequence), Walsh–Hadamard code, multi-diagonal (MD) code, diagonal double weight (DDW) code, modified double weight (MDW) code, and enhanced DDW code have been designed and

implemented in the SAC-OCDMA to eliminate the MAI among multiple users. These codes endured from the limitations by large code lengths, variable cross-correlation, and restriction of the code to design it for flexible number of users. The bandwidth inefficiency, detection method, code generation complexity, and cross-correlation are all major issues in SAC-OCDMA codes.

The number of users determines the performance of the OCDMA system, which is dependent on the cardinality of the OCDMA code. The codes with large cardinality are used in OCDMA systems to maximize the number of users. However, in OCDMA systems, increase the code cardinality is a challenging task. Furthermore, compare to unipolar codes used in non-coherent OCDMA system, bipolar codes that utilized in coherent OCDMA system have pseudo-orthogonality feature where the value of a cross-correlation function between any two codewords can be eliminated, which results in relatively low MAI that further improves system performance.

With the increasingly requirements for data transmission rates and efficiency along with the prospective of SAC-OCDMA technique, this dissertation proposed the bipolar OCDMA scheme by utilizing phase modulator for polarization coding in free-space optical channel for single and multi-user scheme. The proposed bipolar OCDMA maintain the SAC principles that relieve the MAI and has the feature of high transmission rate, high security, and immunity to noise. The proposed structure improves the transmission rate and performance compare to the bipolar system with optical switch [5] and dual EOM scheme [6]. Since the significant influence factors toward the performance of the SAC-OCDMA system are the weather conditions and turbulence-induced channel fading. These factors impact the quality of the received signal and link performance improvement. The performance measurement of the proposed bipolar OCDMA design take into consideration the different channel conditions with several well-known SAC codes.



### **1.3 Research Objectives**

The purposes of this dissertation can be outlined as follows:

1. Design the bipolar OCDMA system with high transmission rate, high security, and immunity to noise by using phase modulator for polarization coding, applied in free-space optical communication.
2. Observe and analyze the feasibility of the proposed bipolar OCDMA architecture in the single-user scheme.
3. Verify the feature of MAI elimination of the proposed bipolar OCDMA structure.
4. Observe and analyze the performance of different type of photodetector on the proposed bipolar OCDMA system.
5. Observe and analyze the effect of different input power on the performance of the proposed bipolar OCDMA system.
6. Observe and analyze the performance of the proposed bipolar OCDMA system in the multi-user scheme with different SAC codes for different weather conditions in additive white Gaussian noise (AWGN) channel.
7. Observe and analyze the performance of the proposed bipolar OCDMA system in the multi-user scheme with different SAC codes for different weather conditions in AWGN and turbulence-induced fading channel.
8. Observe and analyze the performance of the proposed bipolar OCDMA system in the multi-user scheme with different SAC codes for different turbulence-induced fading conditions.

### **1.4 Dissertation Structure**

The dissertation focuses on design of bipolar optical code division multiple access by using phase modulator for polarization coding along with the feasibility verification, MAI elimination testing, and performance measurements in different channel condition. The testing and measurements were conducted with simulation by OptiSystem 10 with the inclusion of noises in the OCDMA system to mimic

the real conditions. The simulation was done for both single-user and multi-user scheme. This dissertation consists of six chapters.

The first chapter is an introduction to the background and motivation of research in optical code division multiple access technology and bipolar signal transmission combined with wireless optical communication system architecture along with the objective of the work and structure of the dissertation.

The second chapter introduces the general concept of optical communication along with the devices in the optical communication, such as laser, optical coupler, modulator, erbium doped fiber amplifier, optical switch, optical polarizer, fiber gratings, optical circulator, and photodetector. This chapter covered recent literature reviews in the fields of optical communications, SAC-OCDMA, bipolar systems, and other related literatures.

The third chapter is the design of bipolar OCDMA proposed in this dissertation along with the simulation setup. The architecture of the proposed encoder and decoder for bipolar signal transmissions combined with OCDMA by utilizing phase modulator for wireless optical communication system was defined in this chapter. Specification of components used, along with the noise and channel models that implemented in the simulation was evaluated in this chapter.

The fourth chapter is the simulation results and analysis. The simulation was conducted to verify the feasibility of the proposed system to generate bipolar OCDMA. MAI elimination property of the proposed structure also tested in this simulation. Further simulation was done to measure the performance in two different channel conditions, namely AWGN channel and AWGN with turbulence-induced fading channel.

The fifth chapter is the conclusion of the dissertation and the proposed future works in the topic of bipolar OCDMA.

## Chapter 2 General Concept and Literature Review

### 2.1 General Concept

#### 2.1.1 Laser

Laser stands for “light amplification by the stimulated emission of radiation” is a device that emits and amplifies light by atoms or molecules stimulation at particular wavelengths. A laser emits a very narrow beam of radiation that usually covers only a small range of visible, infrared, and ultraviolet wavelengths.

Albert Einstein proposed the first laser ideas in 1916, stating that under the proper circumstance, atoms may release excess energy as light, either spontaneously or when stimulated by light. The concept then firstly observed by German physicist, Rudolf Walther Ladenburg in 1928, however there were no practical use at that time and the practical applications took decade to develop. Helium-neon lasers, which could produce a visible red beam and were used for alignment, surveying, construction, and irrigation, were the first lasers with widespread commercial applications. In the middle of the 1970s, laser scanners in supermarkets were the first large-scale application for lasers.

Laser emission is based on the quantum mechanics rules, where the structure of the atom or molecule determines the discrete amount of stored energy. When an atom's electrons are all in the closest possible orbits to its nucleus, it reaches its lowest energy level, known as the ground state. As one or more electrons in an atom consume enough energy, they will excite to the outer orbits and form excited states. These states are unstable, when electrons fall from higher to lower energy levels, they emit light, which is the extra energy.

The relationships between energy, frequency, and wavelength of laser can be express with:

$$E_2 - E_1 = h\nu \quad (1)$$

where  $E$  is energy measured in joules,  $h$  denotes the Planck constant:  $h = 6.626$

$\times 10^{-34}$  (Js), and  $\nu$  is frequency in hertz. Figure 2.1 depict the concepts of laser.

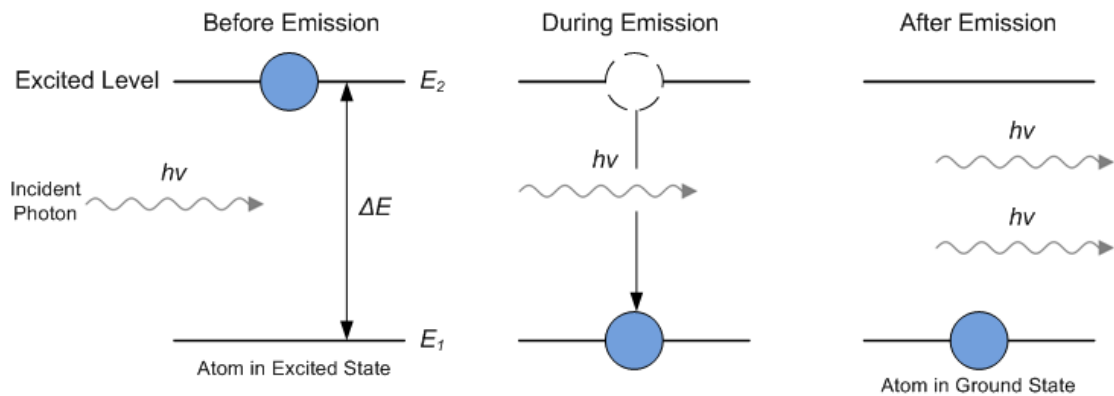


Figure 2.1 Laser concepts

When lower-energy configurations predominate, a spontaneously emitted photon is more likely to be absorbed and lift an electron from a lower-energy configuration to a higher-energy configuration. By emitting a second photon, the higher-energy configuration is excited to fall to a lower-energy configuration. However, a cascade of photons will be generated when higher-energy configurations predominate. This is known as a population inversion, and it can be achieved by illuminating bright light on the laser material or passing an electric current through it.

The basic model has only two energy levels, where the expanded laser systems consist of three or more energy levels. The material is first excited to a short-lived high-energy state in a three-level laser, and then spontaneously falls to a metastable state. The metastable state absorbs and stores the excitation energy, resulting in a population inversion that is further excited to emit radiation, eventually causing the population to fall into the ground state. The ground state must be depopulated for the three-level laser to operate. Since three-level lasers can only generate pulses, when atoms or molecules emit light, they accumulate in the ground state, which absorbs the stimulated emission and quiets the laser action. The four-level laser was proposed to create a steady beam with an extra transition state located between metastable and ground states.

Atoms with two relatively stable levels between their ground state and a

higher-energy excited state can be used to create a continuous laser beam. The atoms would first be induced to release excess energy in a long-lived metastable state before falling to another state above the ground state. Since they drop to a higher-energy excited state rather than the ground state, they can be excited back up to the higher metastable state more easily, preserving the population inversion for continuous laser activity.

An optical resonator is needed to increase the light energy in the beam. This resonator was formed with a pair of mirrors facing each other in which the light emitted along the line would be reflected back and forth between the mirrors. When a population inversion occurs in the medium, the intensity of light that reflected back and forth when traveling through the laser medium increases. The stimulated emission method, the resonant cavity, and the laser medium produce a narrow beam with a narrow wavelength range, that is in phase and coherent with each other, namely monochromatic. A second photon was generated by stimulated emission that is similar to the one that stimulated the emission, cause the new photon has the same phase, wavelength, and direction as the one that stimulated the emission.

The output wavelength is depended on the laser material, the stimulated emission mechanism, and the laser resonator optics. A material can support stimulated emission over a limited range of wavelengths when transitioning between energy levels. Laser oscillation at wavelengths that meet the resonant criteria is facilitated by resonant cavities. This condition necessitates an integral number  $N$  of wavelengths  $\lambda$  equal to the distance light travels between the mirrors on a round trip. If the cavity length is  $L$  and the refractive index of the material in the laser cavity is  $n$ , the requirement to satisfy the condition is:

$$2L = \frac{N \cdot \lambda}{n} \quad (2)$$

The coherent of the beam will increase with the narrower of wavelengths. This property of laser can be measured with coherence length ( $L_c$ ). If the center

of the wavelengths emitted is  $\lambda$  and the range of wavelengths emitted denotes with  $\Delta\lambda$ , the coherence length can be evaluated with:

$$L_c = \frac{\lambda^2}{2.\Delta\lambda} \quad (3)$$

Lasers can be divided into two types, pulsed laser and continuous wave laser. If a laser produces a steady output over a period of time, it is known as a continuous wave laser. Continuous wave operation means that the light is continuously pumped and emitted. Pulsed lasers emit single pulses or a sequence of pulses at regular intervals by concentrating their output energy into high-power bursts. At the peak of a very short pulse, instantaneous power may be extremely high. Continuous wave (CW) or pulse laser sources can be used as optical sources for OCDMA system. Figure 2.2 illustrates the output of continuous wave and pulsed laser.

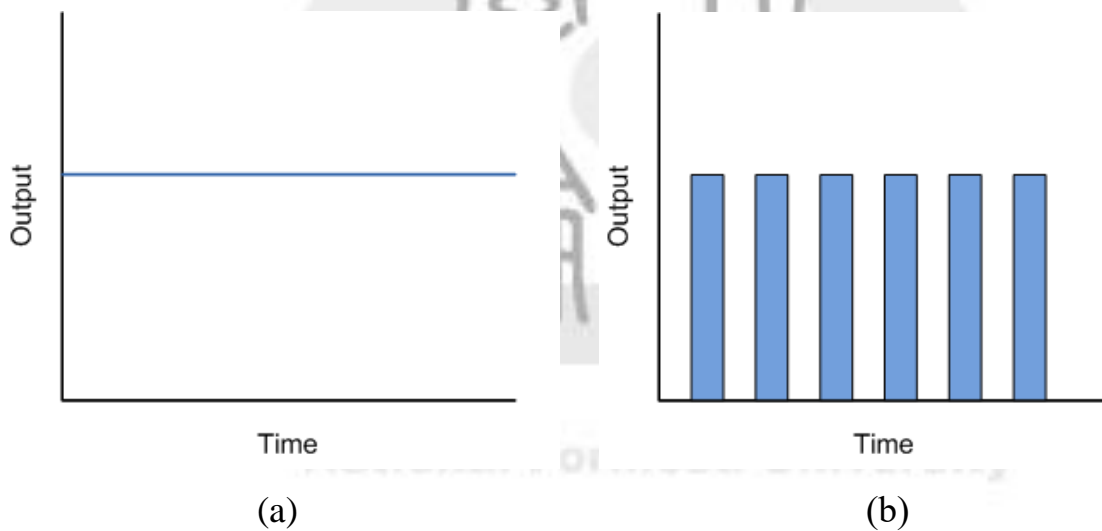


Figure 2.2 Laser types (a) Continuous wave laser, (b) Pulsed laser

The characteristics of a light source for an optical link include:

- Can be worked continuously at a variety of temperatures for several years
- Capable of modulating the light output over a broad spectrum of modulation frequencies. For fiber connections, the output wavelength should correspond to one of the transmission windows for the fiber form.
- For coupling a large amount of power through an optical fiber, the emitting

region should be small.

- In order to minimize material dispersion in an optical fiber connection, the output range should be narrow.
- Low power requirement for its operation.
- The compatibility of the light source with the modern semiconductor devices.
- Capable of directly modulating the optical output power by changing the device's input current.
- Improved linearity to eliminates harmonics and intermodulation distortion.
- Excellent coupling efficiency.
- High optical output power.
- High level of reliability.
- Low-cost and light weight.

In fiber optics, light-emitting diodes (LEDs) and laser diodes (LDs) are typical light sources. Because of the characteristics of LEDs, they are unsuitable for high-speed, long-range outdoor FSO while the advantages of laser diode include the simple economical design, precise control of light generation, narrow spectral width, high optical power, high coupling efficiency, operable at high temperatures, better modulation capability, capable to transmit optical output powers between 5 and 10 mW, and the ability to maintain intrinsic layer properties over long periods of time. The limitation of the laser diode is a speckle pattern appeared at the end of the fiber and the sensitivity to overload currents.

### 2.1.2 Optical Coupler

Optical coupling is a technique for linking two devices so that light waves can be used to transmit an optical signal. In fiber optic systems with one or more input fibers and several output fibers, an optical coupler is one of the optical coupling elements. An optical coupler usually connects two or more fibers cores for combining or splitting optical signals. Optical coupler has the advantages of

low excess loss, high reliability, high stability, dual operating window, low polarization dependent loss, high directivity, and low insertion loss.

Optical fiber principle based on total internal reflection of light. The refractive index and the angle of refraction are important parameters in this process. When two or more optical fiber are fused together, the light from the core leaks onto the cladding of the other core. The leaky light can penetrate into the second core, complete the transferred light process over a certain length. Optical couplers can be formed by fusing fibers together. When an optical coupler is implemented by using two or more parallel optical fibers that have twisted, stretched, and fused together, then this optical coupler is called optical fused coupler. To produce optical fiber fusion, the cores are positioned very close to each other. Optical fused couplers usually have the configuration in multiples of 2, such as  $2 \times 2$  or  $4 \times 4$ . Figure 2.3 shows the scheme of optical coupler.

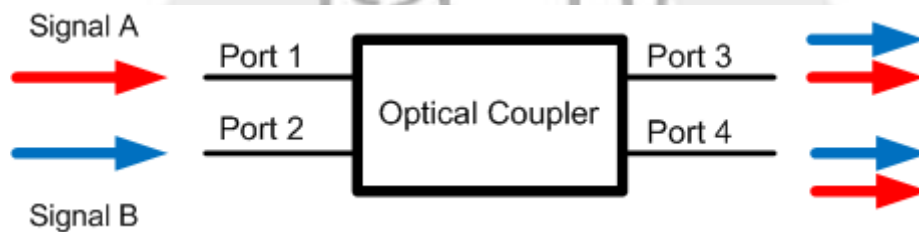


Figure 2.3 Optical coupler scheme

The optical coupler's number of input and output ports is denoted by the  $N \times M$  configuration, where  $N$  denotes the number of inputs and  $M$  denotes the number of outputs. Based on the number of inputs and outputs, optical couplers can be classified into X couplers, combiners, splitters, and trees. Combiners combine two signals to produce one output. Splitters use one optical signal to generate two outputs. Tree couplers that serve as both combiners and splitters in one device. The splitters are classified as either Y couplers with an equal power distribution or T couplers with a variable power distribution.

Optical couplers are classified as active or passive depending on the signal. In the passive optical coupler, there is no optical-to-electrical conversion process, and only redistributes the optical signal. Active couplers working on the principle



of optical-to-electrical conversion that electrically separate and blend the optical signal. Active optical couplers need an external power source, while passive optical couplers need no power to operate.

Essential parameters in the optical coupler are splitting ratio, insertion loss, additional loss, and degree of isolation. The splitting ratio gives the output power of a single split port divided by the total output power of all split ports. Insertion loss is the ratio of optical output power loss relative to the input. Additional loss is defined as the sum of all optical output power compared to the input optical power loss. Additional losses characterize the device quality in the manufacturing process. When the two other ports are terminated by matched loads, the degree of isolation shows the difference in optical signal levels in dB between the input port and the isolated port.

The basic optical coupler that often implemented in the optical system is X coupler. The transmission matrix for the X coupler can be formulated as:

$$\begin{pmatrix} E_{1out} \\ E_{2out} \end{pmatrix} = \alpha \cdot \begin{pmatrix} \sqrt{1-c} & pj\sqrt{c} \\ pj\sqrt{c} & \sqrt{1-c} \end{pmatrix} \begin{pmatrix} E_{1in} \\ E_{2in} \end{pmatrix} \quad (4)$$

where  $p$  is signal power,  $c$  denotes coupling coefficient, and  $\alpha$  is the additional loss.

### 2.1.3 Modulator

The modulation method for the optical signal can be classified into direct modulation and external modulation. Direct modulation works by changing the injection current of a semiconductor light source to alter the strength of the light source. The wavelength of the laser light source can be adjusted with a small amount of current change. At the receiver part, the received signal level (“0” or “1”) is determined by the light intensity. The advantages of direct modulation are no need any external modulation, which is cheap, easy, and highly reliable. On the other hand, the disadvantages of this method are the amount of data that can be modulated is not large and the modulation effect is limited by the laser used.

The chirp effect that produced by direct modulation are also a major problem that will reduce the system performance. Figure 2.4 displays the working principle of direct and external modulation.

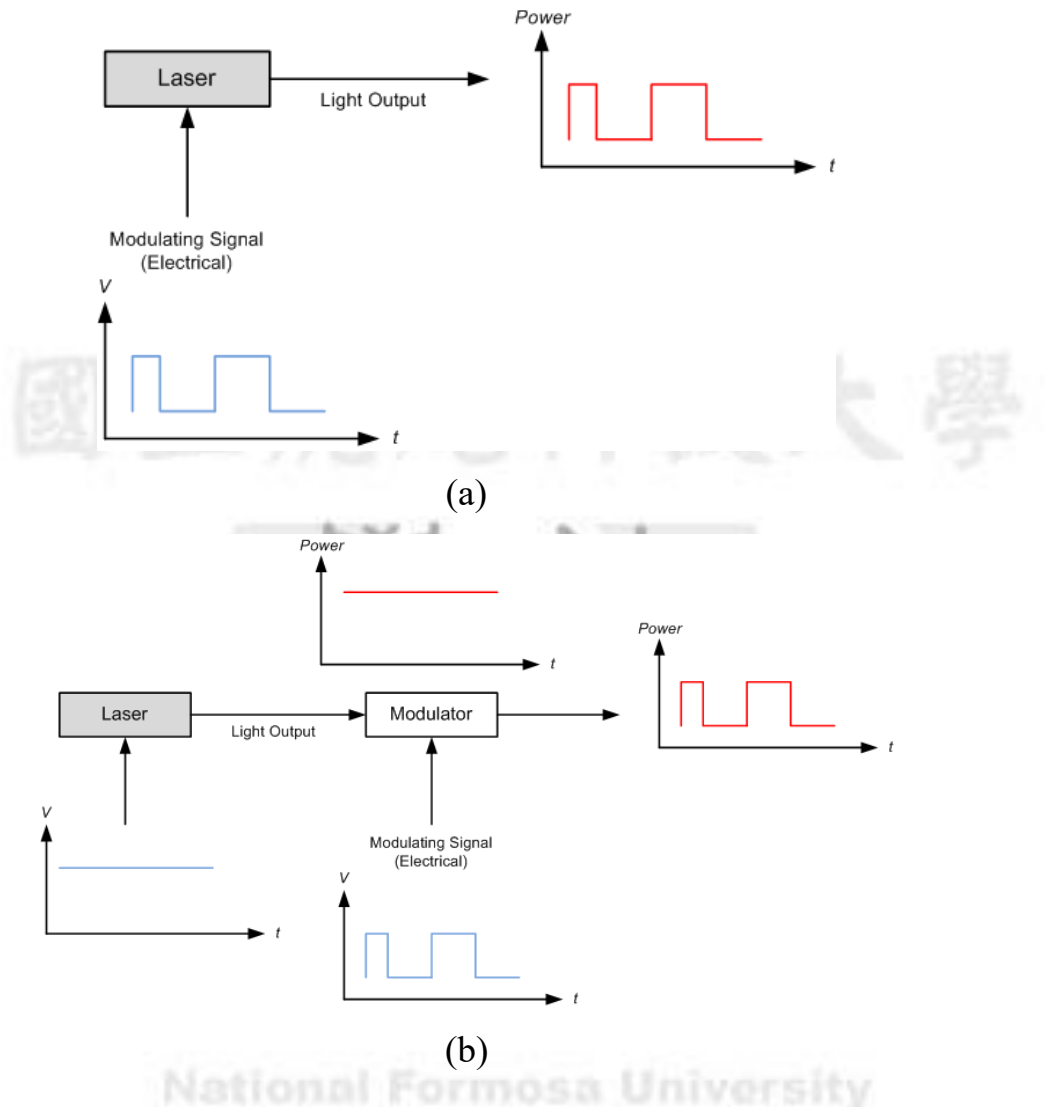


Figure 2.4 Modulation type (a) Direct modulation, (b) External modulation

External modulation is the addition of a modulator after the light source output to modulate the light wave. The advantages of this modulation are the bandwidth is not limited to the laser light source, the small chirp effect, and the speed is much higher than the direct modulation method that enables a higher amount of modulation data. With the small chirp, external modulators are widely used in high-speed long-distance transmission systems. The disadvantage is that external modulator is needed that will more costly than the direct modulation method.

In terms of operation mechanism, there are two typical external modulators, which are EOM and Electro-Absorption Modulator (EAM). EOM are usually constructed around a Pockels cell, which is a crystal with the characteristic of refractive index changed by an electric field. The degree of change is dependent on the field strength. Lithium niobate ( $\text{LiNbO}_3$ ) and other crystalline materials, as well as organic polymers, show the effect. The frequency, amplitude, and polarization of light can all be shifted by this effect. The refractive index of lithium niobate crystals changes in proportion to the electric field applied externally. Although the effect is small (less than 1%), it is sufficient to change the phase and amplitude of the optical beam in most applications. The Pockels cell uses amplitude modulation to adjust the polarization state of the light, which is then converted into a change in transmitted optical amplitude and power using a polarizer.

A resonant EOM is used to achieve a purely sinusoidal modulation with constant frequency. The resonance produced from a resonant inductor-capacitor (LC) circuit. Another EOM is broadband modulators for the operation in a wide frequency range. Integrated traveling-wave modulators are often chosen for high bandwidths in gigahertz applications. In this modulator model, an electronic drive signal produces an electromagnetic wave that propagates along the electrodes in the direction of the optical beam.

Another type, known as phase modulation, uses variations in phase to carry the modulation. Phase modulation formed by modulating the phase of the signal. To obtain this, the frequency of the signal needed to be changed for a relatively short time interval. This criterion states that when phase modulation is applied to a signal, frequency shifts will occur, and vice versa. Since phase is the integral of frequency, phase and frequency are inseparably. The optical phase of a laser beam can be controlled using a phase modulator, which is an electro-optical modulator. Figure 2.5 presents the principle of phase modulation.

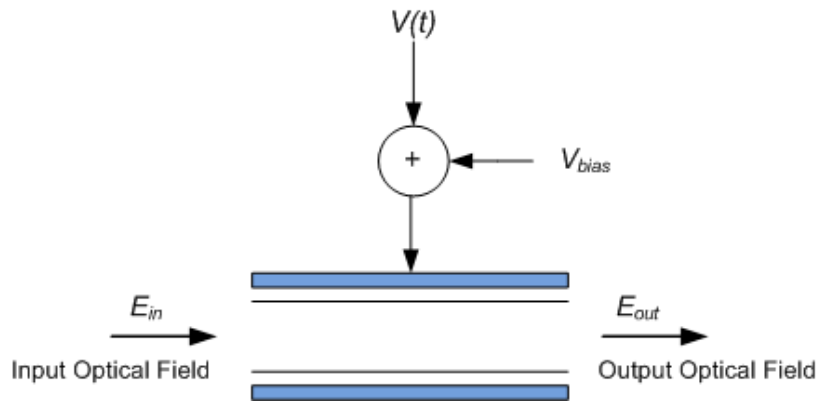


Figure 2.5 Phase modulation

Important parameters of phase modulators are the amount of phase modulation that can be obtained, the modulation bandwidth, the appropriate drive voltage, the optical bandwidth at which the device can be used, the device aperture, and the device outer dimensions.

Some applications of phase modulators are:

- a phase modulator for wavelength tuning or active mode locking within a single-frequency laser.
- in laser frequency stabilization schemes, a phase modulation with moderate modulation strength is utilized.
- spectroscopic measurements include phase modulators in a variety of interferometers and setups.
- phase modulators can be applied for encoding the transmitted information in data transmitters of optical communication systems.

The use of phase modulation in the form of phase shift keying has several advantages in data communications. In comparison to frequency shift keying and other types of modulation, phase shift keying allows data to be carried more efficiently. Another advantage is the immunity toward the noise. Binary phase shift keying (BPSK) is the basic form, in which a digital signal alternating between +1 and -1 or 1 and 0 causes 180-degree phase shifts as the data shifts state. Output optical signals from the phase modulator can be formulated as follow:

$$E_{out,PM}(t) = E_{in,PM}(t) \cdot \exp(j \cdot \Delta Q \cdot X(t)) \quad (5)$$

where  $\Delta Q$  is phase deviation and  $X(t)$  is the electrical input.

#### 2.1.4 Erbium Doped Fiber Amplifier

In the optical communication networks, optical amplifiers are the important technology for enabling the transmission of huge data over long distances in the presence of the fiber loss. The erbium-doped fiber amplifier (EDFA) is an optical amplifier with high gain, wide bandwidth, high output power, low noise figure, and polarization independence, that is widely used in optical communications systems. EDFA is used as an optical repeater unit in a fiber optic communications system to amplify the strength of optical signals. Since an optical fiber is doped with erbium, a rare earth element, it can absorb light at one frequency while emitting light at a different frequency.

The erbium-doped fiber (EDF), which is a conventional silica fiber doped with Erbium, is at the core of EDFA technology. When light of an appropriate wavelength (either 980 nm or 1480 nm) is illuminated into Erbium, it is motivated to a long-lifetime intermediate state, then decays back to the ground state, emitting light in the 1525-1565 nm band. The light at 980 nm can be used as a pump source for Erbium, in which case it passes through an unstable short lifetime state before rapidly decaying to a quasi-stable state, or the light at 1480 nm can be used as a direct pump source for Erbium, in which case it is immediately excited to the quasi-stable state. It decays to the ground state by emitting light in the 1525-1565 nm band once it has reached the quasi-stable state. Pre-existing light will induce this decay process, resulting in amplification. In comparison to the other wavelengths, the 980 nm wavelength has a high pumping efficiency and low noise.

The key components of an EDFA configuration are an EDF, a pump laser, a pump wavelength, and a signal combining component, all of which can propagate simultaneously through the EDF. Pump energy can propagate in the same direction as the signal (forward pumping), the opposite direction (backward

pumping), or both directions in EDFAs (bidirectional pumping). Figure 2.6 depicts the principle of EDFA.

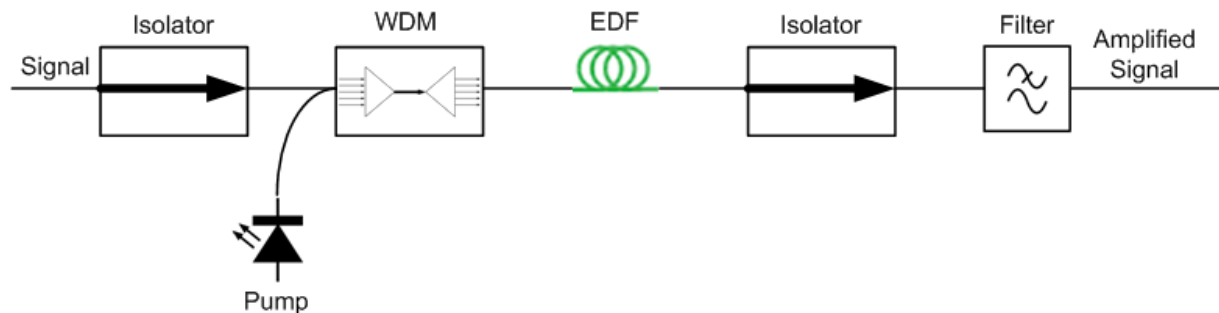


Figure 2.6 EDFA principle

Generally, EDFA can be applied as booster amplifier, preamplifier, and line amplifier. When used as the booster amplifier, EDFA is deployed in the output of an optical transmitter in order to enhance the output power of the multi-wavelength signal having been multiplexed. With booster amplifier, longer distances of optical communication transmission can be achieved. If used as the preamplifier, EDFA must have low noise and high gain characteristics. When used in the input of an optical receiver, EDFA may increase the sensitivity of the receiver. The transmission loss of lines can be compensated periodically when EDFA is used as the line amplifier.

### 2.1.5 Optical Switch

In optical fibers or integrated optical circuits, an optical switch is a mechanism that enables light signals to be transferred from one circuit to another. Optical switches in communication networks can pass light signals between channels. The optical switch may be used to control the connections within an optical circuit by creating, breaking, or changing them. Passive fiber optic switches do not need any electro-optical or opto-electrical conversion to route an optical signal. An electromechanical device can be used to physically position a passive optical switch. An optical switch may have several input and output ports. Three types of optical switches based on their operating principle and function, i.e., opto-mechanical switch, thermo-optic switch, and electro-optic switch.

An opto-mechanical optical switch redirects an optical signal by using mechanical equipment to move fiber or bulk optic components. Stepper motors are commonly used to power these optical switches. The stepper will move the mirror, which will direct light from the input to the desired output. The input and output light beams are collimated within the fiber and balanced within the switching device in an opto-mechanical optical switch. This switch will generate a variety of optical path selections from a number of optical path sections oriented in various spatial directions. Hence, opto-mechanical optical switches can be used in multi-channel optical power monitoring, switching multiple laser sources, optical local area networks, or optical receivers in Ethernet networks with excellent reliability, insertion loss, and cross talk. Opto-mechanical optical switches come in a variety of configurations based on the number of redirecting signals, such as  $1 \times 1$ ,  $1 \times 2$ ,  $1 \times 4$ ,  $1 \times 8$ ,  $1 \times 16$ , etc. For example, the  $1 \times 8$  opto-mechanical optical switch module connects optical channels by redirecting a one incoming optical signal to one of eight output fibers. In micro-electro-mechanical systems (MEMS) optical switches, a micro-mirror is used to reflect a light beam in which the direction of reflection can be adjusted by changing the angle of the mirror, allowing the input light to be connected to either port. It is a small optical switch that connects optical channels by routing incoming light to the desired output fibers. For various temperatures and vibrations, the switching state is very stable. In several aspects, MEMS optical switches differ from opto-mechanical switches, including their characteristics, performance, and reliability. MEMS optical switches also come in a variety of configurations, such as  $1 \times 8$ ,  $1 \times 12$ ,  $1 \times 16$ , etc.

The thermo-optic switch uses polymer or silica waveguides and is based on waveguide theory. In this optical switch, the material's thermal or refractive index properties are used. The theory of this switch is based on a temperature change that cause the changing of the waveguide refractive index. The temperature shift can be proceeded in a variety of ways, mostly resistive heaters are used to heat

the device, which slows light in one of the paths. The device then combines the light from the two paths in a positive or negative effect, allowing for signal attenuation or switching. Due to the time required to heat the waveguide, this type of switch is inherently slow. The optical loss of this system is normally lower than that of an opto-mechanical switch. Thermo-optic switches can be combined with a variety of silicon wafer-based devices and well performing in low optical power applications and compact in size.

When an electromagnetic wave from the optical spectrum passes through a substance under the stress of an electric field, a series of phenomena, namely electro-optic, occur. An electro-optic switch works by using an electric field to change the refractive index of a waveguide. In comparison to thermo-optic systems, this device has a fast response time and low optical power loss since it is semiconductor-based.

#### 2.1.6 Optical Polarizer

The polarization of light is one of the prominent parameters besides the wavelength and intensity of light. The polarization of light has an impact on the focus of laser beams, the cut-off wavelengths of filters, and can be managed to avoid unwanted back reflections. Different degrees of materials can absorb different polarizations of light.

Light is an electromagnetic wave whose electric field oscillates perpendicular to the wave's propagation direction. When this electric field move with the direction that fluctuates randomly in time, this light is called unpolarized. Light sources, such as sunlight, LED spotlights, halogen light, and incandescent bulbs are categorized as unpolarized light. Meanwhile, if the direction of the electric field of light is well defined, the light is referred to as polarized light. P- and S-polarizations are the two orthogonal linear polarization states that are most important for reflection and transmission. P- and S-Polarizations are distinguished by their orientation in relation to the incidence plane. The electric field of P-polarized light is parallel to the axis of incidence, while the electric field of S-



polarized light is perpendicular to the plane. Unpolarized light can be defined as a rapidly varying random combination of P- and S-polarized light. Figure 2.7 reveals the P- and S-polarizations.

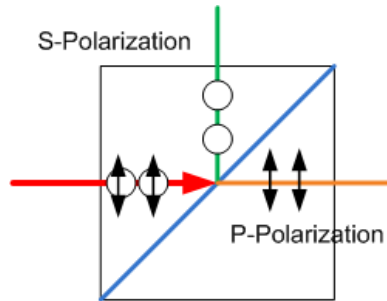


Figure 2.7 P- and S-polarizations

Based on the orientation of electric field, there are three types of polarizations of polarized light:

1. Linear polarization: in the propagation direction, the electric field of light is confined to a single plane. The electric field of linearly polarized light consists of two perpendicular waves with same phase and equal amplitude. The resulting electric field wave propagates along the plane  $y = x$ . For any linearly polarized light traveling in the  $z$  direction, the polarization direction of its electric field  $E(z, t)$  must be parallel to the  $x$ - $y$  plane and can be resolved into:

$$E_x(z, t) = \hat{i} E_{0x} \cos(kz - \omega t) \quad (6)$$

$$E_y(z, t) = \hat{j} E_{0y} \cos(kz - \omega t + \varepsilon) \quad (7)$$

where  $\varepsilon$  is phase difference,  $k = \frac{2\pi}{\lambda}$ ,  $\omega = \frac{2\pi}{T}$ ,  $\lambda$  is wavelength, and  $T$  is the time period. If  $\varepsilon$  equal to zero or multiple of  $\pm 2\pi$ , the resultant wave has a fixed amplitude equal to  $iE_{0x} + jE_{0y}$ , called linearly polarized. Figure 2.8 illustrates the linear polarization where in the propagation path, the electric field of linearly polarized light is confined to the  $y$ - $z$  plane (left) and the  $x$ - $z$  plane (right).

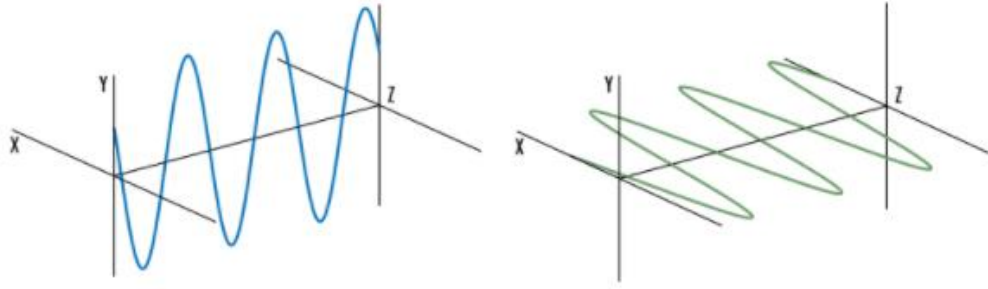


Figure 2.8 Linear polarization

2. Circular polarization: the electric field of light consists of two linear components that are perpendicular to each other and have the same amplitude with a phase difference of  $\pi/2$ . Around the propagation direction, the electric field rotates in a circle. Circular polarization may be classified as left- or right-handed circularly polarized light depending on the rotation direction. If the phase difference is positive, the light wave rotates clockwise formed the right-handed circular polarization state. When the phase difference is negative, the light wave rotates counterclockwise, produce a left-handed circular polarization state. If  $\varepsilon$  equal to  $-\frac{\pi}{2} + 2m\pi$ , where  $m = 0, \pm 1, \pm 2, \dots$

$$E_x(z, t) = \hat{i} E_{0x} \cos(kz - \omega t) \quad (8)$$

$$E_y(z, t) = \hat{j} E_{0y} \sin(kz - \omega t) \quad (9)$$

The resultant wave equal to  $E(z, t) = E_0 [i \cos(kz - \omega t) + j \sin(kz - \omega t)]$ , called circularly polarized.

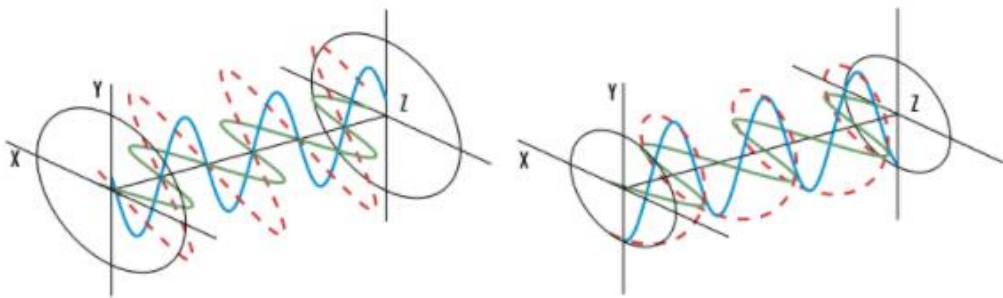


Figure 2.9 Circular polarization

Figure 2.9 depicts the circular polarization. The electric field of linearly

polarized light (left) consists of two perpendicular waves with same phase and equal amplitude. The resulting electric field wave propagates along the  $y = x$  plane. The electric field of circularly polarized light (right) includes two perpendicular linear components that have equal amplitude with a phase difference of  $\pi/2$  or  $90^\circ$ . The resultant electric field wave propagates circularly.

3. Elliptical polarization: the electric field of light consists of two linear components with different amplitude level with a phase difference that is not  $\pi/2$ . The resulting electric field rotates in ellipse. The wave equation traveling in the  $z$  direction can be expressed as a linear combination of two independent field components vibrating in the  $x$  and  $y$  directions is  $E = iE_x + jE_y$ , with:

$$E_x = E_{0x} \cos(\omega t - kz + \delta_x) \quad (10)$$

$$E_y = E_{0y} \cos(\omega t - kz + \delta_y) \quad (11)$$

where  $\delta_x$  and  $\delta_y$  are the phase difference for  $x$  and  $y$  direction, respectively.

Depending on the trajectory of the vector end of the optical electric field  $E$  at any point in space at different times and the polarization state is different,  $\omega t - kz$  is eliminated and can be evaluated as:

$$\left(\frac{E_x}{a}\right)^2 + \left(\frac{E_y}{a_y}\right)^2 - 2\frac{E_x}{a} = \frac{E_y}{a_y} \cos \delta = \sin^2 \delta \quad (12)$$

where  $\delta = \delta_y - \delta_x$ .  $(E_x, E_y)$  are the coordinates that turn an ellipse at an angle  $\theta$ :

$$\tan 2\theta = \frac{2a_x a_y}{a_x^2 - a_y^2} \cos \delta \quad (13)$$

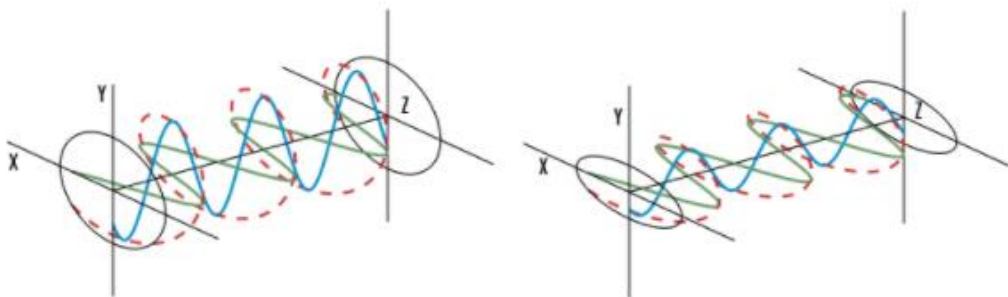


Figure 2.10 Elliptical polarization

Figure 2.10 demonstrates the elliptical polarization. The circular electric field

(left) consist of two components with equal amplitude and have a  $\pi/2$  or  $90^\circ$  phase difference. It will produce elliptically polarized light (right) if the two components have different amplitudes or if the phase difference is not  $\pi/2$ .

Polarizers are widely used in optical systems to choose a particular polarization of light. It can be utilized to filter the undefined or mixed polarized light beams into a well-defined polarized light beam, that is, polarized light. There are two types of polarizers that commonly used, i.e., linear polarizers and circular polarizers. A polarizer is one of the tools commonly used to obtain linearly polarized light. This element allows the electric field of the incident beam to be selected, and only allows a beam of a specific polarization direction to pass. Polarizers can be categorized into birefringent, reflective, and dichroic polarizers. The principle of birefringent polarizers is founded on the fact that the refractive index of light is proportional to its polarization. This feature can be used to select specific polarizations of light since different polarizations refract at different angles. Reflective polarizers transmit the desired polarization and reflecting the rest. Dichroic polarizers absorb a specific polarization of light while transmitting the others.

The initial unpolarized amplitude  $I_0$  would be reduced by half since an ideal linear polarizer only transmits one of the two linear polarizations. Malus' law describes the intensity  $I$  transmitted by an ideal polarizer for linearly polarized light with intensity  $I_0$ :

$$I = I_0 \cos^2 \theta \quad (14)$$

where  $\theta$  denotes the angle between the polarization axis and the incident linear polarization. When the two polarization angles are parallel, the intensity of the light passing through is the maximum,  $I = I_0$ ; when the angles of the two polarizers are perpendicular to each other, the light intensity is 0,  $I = I_0 \times \cos^2 90^\circ = 0$ , means that light cannot pass through.

With polarizers, certain polarizations of light are selected, while the other

polarizations will be discarded, result in the attenuation. Ideal waveplates change the polarization of a beam without attenuating, deviating, or discarding it. This principle is obtained by delaying or retarding one polarization component in relation to its orthogonal component. Any polarization state can be converted into a new polarization state using the appropriate waveplates. Waveplates are used to rotate linear polarization, such as to transform linearly polarized light to circularly polarized light or vice versa. Based on the orientation manipulation of the light, waveplate can be divided into:

- Half waveplate ( $\lambda/2$ -plate), rotate a linear polarization state into any other direction.
- Quarter-wave plate ( $\lambda/4$ -plate), the axis of which is oriented at  $45^\circ$  to the direction of polarization, caused a linear polarization state is converted into a circular one (and vice versa).
- Combination plate, for example one half waveplate and two quarter waveplates, can realize a polarization controller, where arbitrary polarization can be converted by properly rotating the three plates.

Monochromatic light's polarization state is typically represented by a Jones vector, which may be constant over a certain region of the beam or may differ. Jones matrices can be used to express the effect of optical elements like waveplates, polarizers, and Faraday rotators. Jones vectors are only applicable to completely defined polarization states but not applicable to unpolarized or partially polarized beams with stochastic nature.

### 2.1.7 Fiber Gratings

Fiber gratings are one of the most significant elements in fiber optic networks for a variety of applications. Fiber gratings are fabricated with ultra-violet (UV) laser exposure with the characteristic of low insertion loss. Fiber grating have several parameters that can be varied according to the application, including grating period, length, apodization, chirp, induced index change, and fringe tilt.

For a given wavelength, the grating design may allow either counter-propagating or co-propagating coupling.

From the diffraction principle in geometric linear optics, a slit from the light source that incident on a plane will produce bright and dark phases with different intervals due to the wavelength of the incident light and the width of the slit. The whole bright and dark phases will be represented by the distribution of the Bayesian function. If the single slit in the diffraction principle is expanded into a periodic slit, a superimposed effect can be obtained. The structure of this periodic slit is a so-called grating structure. If a grating structure is applied in an optical fiber, a so-called fiber grating can be obtained. According to the size of the grating period, fiber gratings can be categorized into two types, i.e., short-cycle and long-cycle. Although these two types of fiber gratings differ only in the length of the grating period, their characteristics are quite different.

The most commonly used of fiber gratings in recent fiber optic communication systems is fiber Bragg gratings (FBG). With the short cycle length, which is less than 1  $\mu\text{m}$ , FBG are also called short-cycle fibers grating. This type of fiber grating can do reflection at a specific wavelength, it is also known as a reflective fiber grating. The grating is constructed by changing the refractive index of the core. The grating then reflects back the light of a particular wavelength transmitted along the optical fiber, with the reflection direction matching the optical fiber's incident direction. The un-corresponding wavelength will pass through with little or no attenuation. FBG has the advantages of a small size, low insertion loss, high reliability, and compatibility with other fiber components or systems. FBG are a wavelength-selective filter, that is both simple and inexpensive. It has a wide range of applications that can increase the efficiency of optical networks while also lowering their costs. FBG first demonstrated in 1978 where the grating is formed by the exposed core with strong optical interference fringes. After a few minutes of reaction, excited argon ions are irradiated onto the Germanic fiber, and the light intensity increases until

almost all of the light is reflected from the fiber. FBG are made by exposing the core of a single-mode fiber laterally to a periodic pattern of intense laser light. The exposure causes the refractive index of the fiber core to increase permanently, resulting in a fixed index modulation corresponding to the exposure pattern. This fixed index modulation is known as a grating. A small amount of light is reflected with each periodic change in refraction. Furthermore, when the grating period is approximately half the wavelength of the input light, the reflected light signals combine coherently to create a large reflection at that wavelength. This is referred to as the Bragg condition, and the Bragg wavelength refers to the wavelength at which this reflection occurs. All light signals of unmatched phase, other than the Bragg wavelength, are practically transparent. As a result, light passes through the grating with no signal loss or attenuation. Only wavelengths that meet the Bragg condition are affected, and they are strongly reflected back. Figure 2.11 displays the structure and principle of FBG.

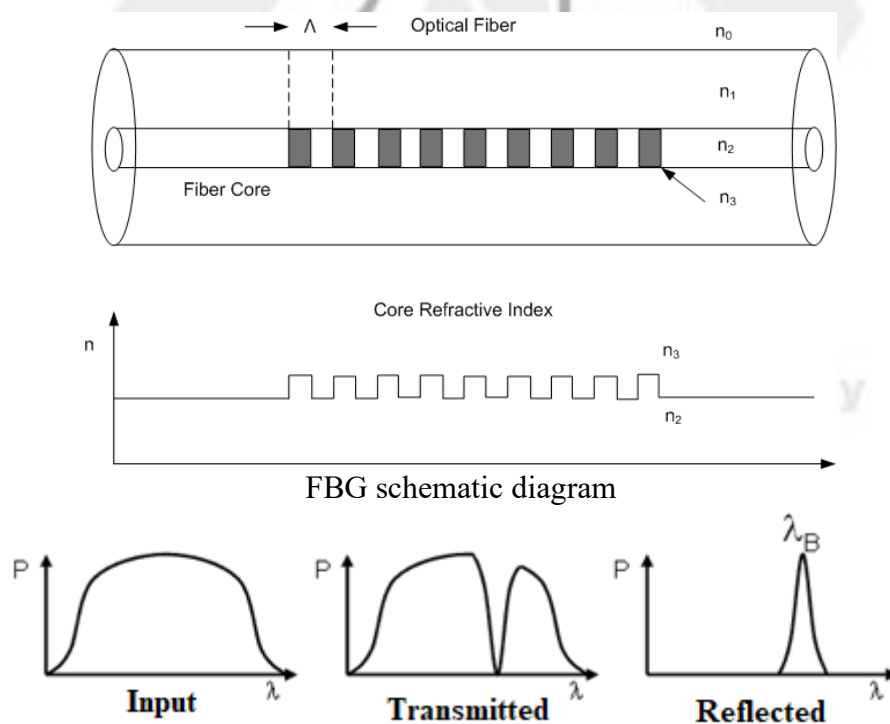


Figure 2.11 FBG principle

The central wavelength of the reflected component fulfills the Bragg equation:

$$\lambda_B = 2n_e \Lambda \quad (15)$$

where  $n_e$  denotes the effective refractive index of the grating in the fiber core and  $\Lambda$  is the grating period. The wavelength of the reflected component will change as a function of temperature and/or strain due to the temperature and strain dependence of the parameters  $n_e$  and  $\Lambda$ .

### 2.1.6 Optical Circulator

Optical circulators are used to redirect optical signals from one port to another in optical communication systems and optical instrumentation. The structure of optical circulator is depicted in Figure 2.12 while the principle of optical circulator is illustrated in Figure 2.13.

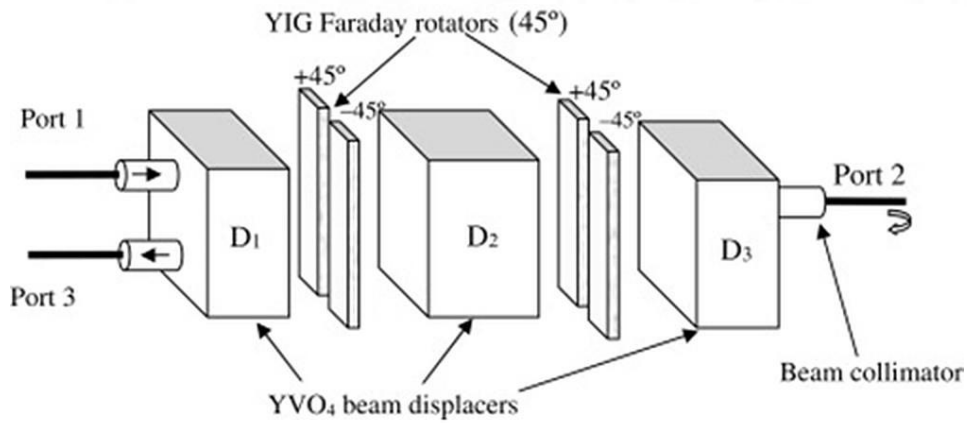


Figure 2.12 Optical circulator structure [7]

In the forward-propagation direction, i.e., from port#1 to #2, the first YVO<sub>4</sub> beam displacer splits the incoming light beam into ordinary (o) and extraordinary (e) beams, which are seen as solid and dashed lines, respectively. Near each light beam, the polarization state is also showed. These two beams travel through two Bi-YIG Faraday rotators, with the left rotator ( $a_1$ ) rotating the o beam +45 degrees and the right rotator ( $b_1$ ) rotating the e beam -45 degrees. The two beams become co-polarized after going through the first pair of Faraday rotators, and two beams are both o beams in the second YVO<sub>4</sub> displacer ( $D_2$ ). Since the polarization states of these two different beams are now the same, they will pass through the second displacer  $D_2$  with no more divergence. The left beam will rotate +45° at the left



rotator ( $a_2$ ) and the right beam will rotate  $-45^\circ$  at the right rotator ( $b_2$ ) at the second set of Faraday rotators, where the polarization states will become orthogonal with each other. The third beam displacer ( $D_3$ ) further combines these two different beams, which reconstructs the input optical signal with a  $90^\circ$  polarization rotation.

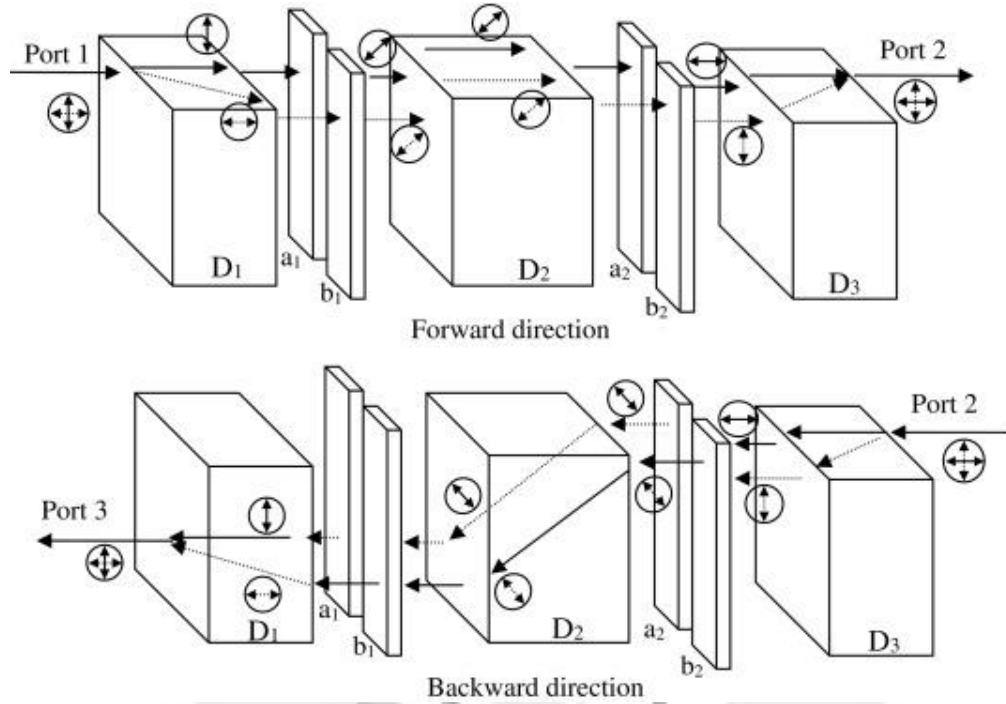


Figure 2.13 Optical circulator principle [7]

Furthermore, from port#2 to #3, where the light beam propagates backward, the light beams first pass through  $D_3$ , which creates a beam separation. The Faraday rotator  $a_2$  then rotates the reflected beam by  $+45^\circ$ , while  $b_2$  rotates it by  $-45^\circ$ . These two beams are co-polarized and both are e beams after going through the  $D_2$ . These two beams are recombined at port 3 after going through the first set of Faraday rotators and the first beam displacer ( $D_1$ ).

In optical circulator, important specifications include insertion loss, polarization dependent loss (PDL), return loss, and isolation. Furthermore, since a circulator has more than two terminals, directionality is a critical factor to consider. Insertion loss in a three-port circulator involves losses from port#1 to #2 and from port#2 to #3. Isolation from port#2 to #1 and from port#3 to #2 is also included in the isolation. When port#2 is terminated without reflection, losses

from port#1 to #3 characterize directivity.

Optical circulators can be divided into polarization-dependent optical circulators and polarization-independent optical circulators. Polarization-dependent optical circulator only works for light with a specific polarization state, for example in free-space communications between satellites and optical sensing. Since the polarization of a light can change during propagation, a polarization-independent optical circulator can be used for light without a specific polarization state.

### 2.1.7 Photodetector

The photodetector is an optical component in the optical receiver that functions as an optical/electrical (O/E) converter, converting the optical signal into an electrical signal. The working of the photodetector is based on the photoelectric effect as showed in Figure 2.14.

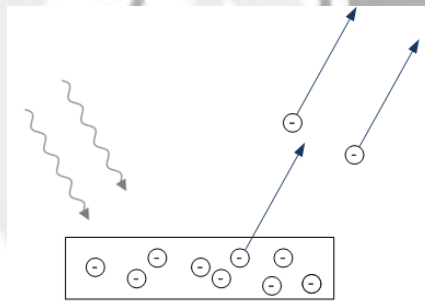


Figure 2.14 Photoelectric effect

When the PN junction of the semiconductor is irradiated by the light, if the photon energy is sufficiently large, the electrons in the valence band will move from the valence band in the semiconductor material by absorbing the energy of the photons. When the forbidden band achieves the conductive band, electrons emerge in the conductive band, and a hole is appeared in the valence band, resulted in a photo-generated electron-hole pair, complete the photoelectric effect of the semiconductor. If the energy gap of the photodetector material is  $E_g$  and the incident photon energy is  $E_p$ , the incident photon energy should be greater

than the energy gap to generate a current. The conditions fulfil by  $E_p \geq E_g$  and  $h.f \geq E_g$  where the cutoff frequency can be evaluated with:

$$f_c = \frac{E_g}{h} \quad (16)$$

The photodetector must be sensitive to the received light signal's emission wavelength spectrum, have a low impact of noise on the signal, be able to operate at the desired data rate with fast response, be temperature tolerant, compatible with the dimensions of the fiber, be relatively low-cost, and have a long operating lifetime.

Some important parameters of photodetectors:

- **Quantum Efficiency**  
The ratio of incident photon-generated primary electron-hole pairs to photon incident on the diode material.
- **Detector Responsivity**  
The efficiency of a system is determined by the ratio of output current to input optical power.
- **Spectral Response Range**  
The wavelength range in which the system would work.
- **Noise Characteristics**  
The amount of noise produced by the device.
- **Response Time**  
The time it takes for the detector to respond to changes in the intensity of the input light.
- **Dark Current**  
The amount of current that flows through the photodiode if the diode is reverse-biased, when there is no light (dark).

Photodiodes, or semiconductor photodetectors, are the common types of photodetectors used in optical communication systems. Photodiode has the

benefits of their small size, high detection efficiency, and fast detection speed. Photodiodes are also based on the PN junctions. However, unlike a laser diode in which the PN junction is forward biased, the PN junction of a photodetector is reversely biased so that without an input optical signal, a very small reverse saturation current will flow through the diode.

Photodetectors with a fast response time for a limited amount of light are worth for high-speed optical communications applications. Positive-intrinsic-negative photodiodes (PINs) and avalanche photodiodes (APDs) are included in this category.

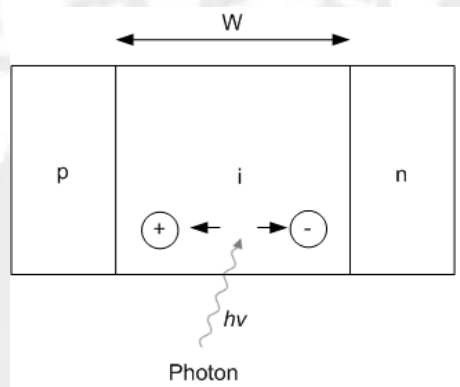


Figure 2.15 PIN photodiode structure

The PIN diode is a modification of the PN junction for certain applications. The PN junction diode was first used as a rectifier for high power and low frequency applications in 1952, after being developed in the 1940s. The breakdown voltage can be increase significantly with the presence of an intrinsic layer for high voltage applications. As the system operates at high frequencies, such as radio waves and microwaves, this intrinsic layer provides exciting properties. PIN diodes have three regions: P, I, and N. Both the P and N regions are highly doped for ohmic contacts. Between the P and N semiconductor regions, a PIN diode has a wide intrinsic semiconductor region. The broader intrinsic region is indifferent to an ordinary PN diode. This region allows the diode to be used in power electronics for fast switches, photodetectors, attenuators, and high voltage applications. Figure 2.15 presents the structure of PIN photodiode.

When reverse-biased, this system has a nearly infinite internal impedance, operates like an open circuit, and produces an output current proportional to the input optical power. In terms of incident optical power, the optical power absorbed in the depletion region can be calculated by using:

$$P(x) = P_0 \left(1 - e^{-\alpha_s(\lambda)x}\right) \quad (17)$$

where  $P_0$  is the input optical power,  $\alpha_s(\lambda)$  denotes the photon absorption coefficient. The wavelength cutoff for any semiconductor can be determined by its energy gap:

$$\lambda_c (\mu m) = \frac{1.24}{E_g (eV)} \quad (18)$$

The primary absorption-induced photocurrent is:

$$I_p = \frac{q}{h\nu} P_0 \left(1 - e^{-\alpha_s(\lambda)x}\right) (1 - R_f) \quad (19)$$

where  $q$  is the electric charge,  $\nu$  denotes the velocity, and  $R_f$  is the resistance. The quantum efficiency can be examined with:

$$\eta = \frac{I_p / q}{P_0 / h\nu} \quad (20)$$

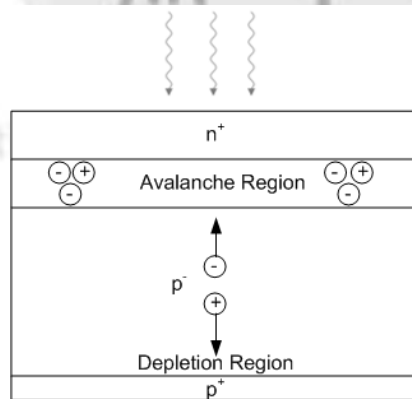


Figure 2.16 APD photodiode structure

The APD is a semiconductor device that produces strong fields in the junction region for the reverse direction. The electron-hole pair produced by a photon flows through the junction. The electron gains enough energy to create

secondary electron-hole pairs, which in turn create more pairs, thanks to the strong fields in the junction. A multiplication (or avalanche) process occurs as a result, and a large current is produced from a small number of photons. Figure 2.16 shows the structure of APD photodiode.

A certain minimum current is required for the detector to operate reliably. The minimum power requirement can be calculated by:

$$P_{in} = I_p \mathfrak{R} \quad (21)$$

For small optical power, detectors with a large responsivity  $\mathfrak{R}$  are preferred. The APDs have much larger values of  $\mathfrak{R}$  compare to the PIN photodiodes. Compare to PIN photodiode, APD possess high intensity electric field region. In this area, primary electron-hole pairs are generated when the incident photons absorb enough kinetic energy from the strong electric field to collide with the atoms present, forming more electron-hole pairs.

Impact ionization is the physical process that causes internal current amplification and avalanche breakdown at ordinary reverse bias. A very high reverse bias voltage is required for the new charge carriers generated by the impact ionization to generate more charge carriers themselves by the same mechanism. The process of generating more than one electron-hole pair from the incident photon by the ionization process is called the avalanche effect.

The avalanche multiplication resulted in amplification of the photodiode current. The APD's internal gain, or the ratio of the total multiplied output current to the primary non-multiplied current, is measured by the multiplication factor  $M$ , which can be determined by using:

$$M = \frac{I_M}{I_p} \quad (22)$$

where  $I_M$  denotes the average value of the total multiplied output current and  $I_p$  is the primary photocurrent.

Multiplication relies on physical and operational characteristics of

photodetector device. Operational characteristics include the width of the avalanche area and the strength of the electric field. The response sensitivity of the APD can be evaluated as follows:

$$\mathfrak{R}_{APD} = \frac{\eta q}{h\nu} M = \mathfrak{R}_0 M \quad (23)$$

When the field in the depletion region exceeds a saturation value, the charge carriers move with maximum drift velocity. The longest travel time for the charge carriers to travel through the full depletion layer width:

$$\tau_{tr} = \frac{W}{v_d} \quad (24)$$

where  $W$  is the width of the depletion layer, which varies with acceptor and donor concentrations and  $v_d$  denotes a velocity that varies with applied voltage but reaches a maximum (saturation velocity) of  $\sim 105$  m/s. The saturation velocity is dependent on the photodiode material where  $W \sim 10$   $\mu\text{m}$ ,  $v_d \sim 105$  m/s, and  $\tau_{tr} \sim 100$  ps are typical values. To minimize  $\tau_{tr}$ , both  $W$  and  $v_d$  can be optimized. The bandwidth after the photodetector acts like a time-constant RC low-pass filter with a passband:

$$B = \frac{1}{2\pi R_T C_T} \quad (25)$$

$$R_T = R_S // R_L \quad (26)$$

where  $R_L$  is the external load resistance,  $R_S$  is the internal series resistance, and  $C_T$  is the parasitic capacitance.

The existence of a diffusive component in the photocurrent, which is related to the absorption of incident light beyond the depletion region, limits the bandwidth of PN photodiodes. Electrons produced in the P-region must diffuse to the depletion region's boundary before drifting to the N-side; similarly, holes generated in the N-region must diffuse to the depletion region's boundary before drifting to the P-side. The diffusion process is relatively slow, taking a nanosecond

or longer for charge carriers to diffuse over a 1  $\mu\text{m}$ . The diffusion limitation can be minimized by increasing the width of the depletion region and decreasing the width of the P and N regions, so that the region absorbs most of the incident optical power.

APD photodiodes are favored for long-distance high-bit rate fiber optic communications because of their internal gain, which offers a better sensitivity margin than PIN photodiodes. APDs have a 5 to 10 dB higher sensitivity than PIN if the multiplication noise is low and the gain-bandwidth is high enough.

## 2.2 Literature Review

The next development stage of the mobile communication network allows a significantly higher data capacity and extremely fast response times. This completely support new potential applications for a fully connected network, such as cloud computing, mobile computing, internet of things, and many other next generation services. Liu et al. in [1] reported the forecast for next 10 years mobile communication technology demands and challenges which is low-cost high-capacity performance. The study was performed using specified performance metrics for the mobile broadband (MBB) service and IoT perspective, which included requirements from the particular service and user demands, network implementation and operation requirements, and 5G system capabilities and efficiency requirements. The calculations showed that 5G capable to fulfil the requirement of the increasing traffic with high data rates and low latency. The predictions have confirmed that 5G is capable of linking a large number of devices and providing a seamless experience across a wide range of scenarios, as well as intelligent optimization that can dramatically reduce energy and cost consumption.

With the advantages of high bandwidth, low latency, resistance to electromagnetic interference, high reliability, and high security, optical fiber network becomes prospective choice to meet the demands of the 5G or higher



network technology. With the drawbacks of wired optical networks, i.e., complexity of installation and high-cost, FSO communication become one of the favorite technologies. One of the essential technical parts of the FSO to support multi-user is the multiple access technology. The most common used multiplexing technology in the optical system is WDM, which utilize different light wavelengths to send data through the common channel. The disadvantage of the WDM techniques is the spectral dispersion. With the limitation of spectral bandwidth resource, many re-searches focus on the improvement of WDM performance. Chakkour *et al.* in [8] introduced optical transmission model to increase the performance of WDM. In terms of reflectivity peak, full width at half maximum bandwidth (FWHM), and side lobe level, an FBG and an EDFA were used in this model to compensate for chromatic dispersions and nonlinear effects. The output was measured with 16-channel wavelengths and the nonlinear Schrödinger equations were solved using the split-step fourier process. Further, coupled mode theory (CMT) and transfer matrix method (TMM) were also implemented for reflection spectrum optimization with high reflectivity, small FWHM, and an efficient side lobe suppression. Simulation results showed that the proposed approach generated better responses in contrast to other methods.

Another method was introduced by Singh *et al.* in [9] with the differential quadrature phase shift keying (DQPSK)-polarization shift keying (PolSK) modulation scheme. In a 16-channel WDM-based inter-satellite optical wireless communication (IsOWC) system, the modulation scheme was used to transmit  $16 \times 100$  Gbps data over a 25,000 km transmission channel. The demonstration verified that the proposed model can achieved the acceptable bit error rate (BER). Further simulation with space turbulences indicated that acceptable performance could be achieved from the transmission of information up to  $2.7 \mu\text{rad}$  receiver pointing error angle through the proposed link.

Another multiplexing technique is TDM. This method is implemented effective spectrum sharing for multi-user scheme in optical networks by utilizing

same wavelength. However, for the adjacent wavelength, time delay is needed. TDM suffered from nonlinear fiber effects. In this technique, the optical clock distribution and synchronization plays an important role. Mishra *et al.* in [10] proposed DEC time division multiple access (TDMA) as cooperative mechanism in the integrated passive optical network and wireless access network referred to as fiber-wireless (FiWi) access network. Since delay and efficient energy utilization becomes challenges in FiWi network, the proposed mechanism improved these two factors by using front-end and back-end cooperation with time stamping for synchronization. For energy efficiency using TDMA, the analysis was made simultaneously in the optical line terminal (OLT), optical network units (ONUs), access points (APs), and stations while delay performance was improved with clusters of ONUs and equal partition approach. The proposed approach further compared with the existing ONU sleeping, clustered ONU sleeping, and energy conservation (ECO) FiWi method. The reported results indicated that DEC TDMA increased the energy efficiency compare to ONU sleeping, and clustered ONU sleeping. Further findings revealed that, while the proposed approach's energy efficiency was comparable to that of ECO FiWi, DEC TDMA's delay output was superior to that of ECO FiWi, as well as ONU sleeping and clustered ONU sleeping approach. Overall, the results showed that the proposed mechanism, which improved delay and energy efficiency, could be implemented for large-scale FiWi access networks with high bandwidth requirements under heavy load conditions.

Further method was proposed by Zhang *et al.* in [11] with optical signal processing to realize the high-speed optical fiber networks based on TDMA technique. In this scheme, two wavelengths were implemented to carry both the optical TDMA signal and clock signals, respectively. In the receiver-end, optical delay lines were designed to achieved the optical TDMA signal and clock signals separately. By implementing the proposed model, large-scale digital TV or high-definition (HD) TV broadcasting networks can be implemented using multi-star

topology. The proposed architecture also can be applied in ultra-high-capacity optical fiber networks for real-time computer communications and multiprocessor interconnection.

Another prospective multiplexing technique is OCDMA which is implement a unique code to achieve high-speed and large bandwidth network. With the feature of MAI mitigation and noise effect suppression, SAC become one of the promising techniques for OCDMA. There are many important aspects of OCDMA that affect the performance of the system, including the light source in the transmitter-end and detection method in the receiver-end.

Moghaddasi *et al.* in [12] utilized a multi-wavelength laser source and a vertical cavity surface emitting laser array for SAC-OCDMA in a free-space optical network. In addition to the turbulence, the effect of optical beat interference (OBI), relative intensity noise, and receiver noises were included in the analysis. The numerical evaluation showed that the proposed system suffered most from OBI, especially at higher received power. Further observations compared the modified quadratic congruence (MQC) and modified double weight (MDW) code with the result of higher performance achieved with MDW codes. In the condition of moderate turbulence, a successful transmission could be achieved for 10 users' scheme at 2.6 km distance with 8 cm aperture diameter. The performance could be further improved by increasing the aperture diameter or decreasing the beam divergence below 1 mrad.

For the receiving-end, Mottaleb *et al.* in [13] investigated the use of single photodiode (SPD) for detection technique of SAC-OCDMA system. The simulations employed three simultaneous users and implemented enhanced double weight (EDW) codes for the signature codes. PIIN and MAI were also included in the simulations. The simulation compared the use of APD and PIN PD as photodetector, explored the effect of dispersion compensating fiber (DCF) to the system performance, and finally compared the EDW and MDW codes performance on the proposed system. The simulations results presented that the

proposed SAC-OCDMA system could achieved longer transmission distance with APD than PIN PD. Further results showed that the use of DCF improved the system performance.

Further detection method comparation conducted by Thakur *et al.* in [14] with several detection techniques in OCDMA, i.e., AND subtraction method, modified AND (M-AND) detection method, direct detection method, and SPD. According to the findings, direct detection outperformed AND detection, while M-AND outperformed AND subtraction detection in terms of Q-factor and BER. SPD obtained better performance at a high data rates and could be used in the longer distance as compare to other subtraction detection techniques. Since SPD only used one photodetector, the receiver-end has the low-cost design.

Another comparation of detection technique in the presence of atmospheric turbulence was simulated by Aissaoui *et al.* in [15]. The performance comparision between various detection techniques in the SAC-OCDMA system for FSO with atmospheric losses channel was reported in [15]. The simulation results revealed that SPD technique with the EDW code outperformed the complementary subtraction detection (CSD) and M-AND detection techniques. SPD technique maintains the PIIN and MAI elimination in the optical system with low-cost design since it only used one photodetector.

Boukricha *et al.* proposed the use of narrowband Bragg gratings as filter in the encoder and decoder of SAC-OCDMA system. In [16], the SAC-OCDMA system performance was evaluated by utilizing fiber Bragg gratings as narrowband filter. Variations in optical power, fiber length, data rate, and bandwidth were observed. The simulations result for three simultaneous user's system presented that an acceptable BER  $< 10^{-9}$  can be achieved with data rate of 200 Mbits/s and a FBGs bandwidth of 0.6 nm for 25 km length. Further system with nine users verified that the performance maintained up to eight users for distance of 5 km.

In order to improve the performance of SAC-OCDMA, hybrid method was designed by Aldhaibani *et al.* in [17] by combining orthogonal frequency division multiplexing (OFDM) and SAC-OCDMA to achieve high data rate and high fidelity in the fiber links. The simulation results with MD code proved that the proposed hybrid system can reach  $10^{-4}$  BER improvement with 10 Gbps data rate at 100 Km distance.

Another effort to improve the OCDMA performance by combining with WDM was introduced in [18] that proposed passive optical network (PON) system with OCDMA over WDM. The proposed hybrid model implemented the superstructure fiber Bragg gratings (SSFBG) and multi-port OCDMA encoders/decoders. The demonstration revealed that the proposed asynchronous model could achieved transmission rates of more than 380 Gbit/s while maintaining a spectral efficiency of about 0.32. The flexible and cost-effective design drive the proposed hybrid system become the prospective choice for gigabit-symmetric fiber-to-the home (FTTH) services.

Further hybrid method was proposed by Bhanja *et al.* in [19] that evaluated the hybrid system between SAC-OCDMA technique and OFDM technique for FSO communication network. Two kind of SAC-OCDMA codes, i.e., triangular matrix-zero cross correlation (TM-ZCC) and pulse shifting substitution-zero cross correlation (PSS-ZCC) codes were proposed in [19]. The proposed hybrid system was simulated with 20 and 30 active users simultaneously at various data rates through the Gamma-Gamma fading channel. Two different detection techniques, i.e., M-AND and SPD were applied in the decoding part. The simulation results revealed that the proposed hybrid method with SPD detection has superior performance than the M-AND detection. Further results demonstrated that the proposed hybrid scheme with TM-ZCC code achieved higher performance compare with PSS-ZCC code. Other simulations showed that the proposed method with TM-ZCC and PSS-ZCC code outperformed the KS and RD codes

and overall exhibited higher performance compare to conventional SAC-OCDMA method.

Park *et al.* exploited the OCDMA scheme for optical subscriber access networks in [20] by using modified pseudorandom noise (PN)-coded fiber Bragg gratings architecture in bipolar OCDMA decoders. The numerical analysis indicated that MAI among ONUs can be relieved when there is no spectral power distortion if bipolar OCDMA decoder and modified PN codes were implemented in the OCDMA system. When the data was encoded both with a unipolar signature sequence of the modified PN code and its complement, the proposed scheme's BER performance can be improved under the same SINR compared with the on-off shift keying (OOK)-based OCDMA system. In the case of spectral power distortion was exists with the total transmitted optical power of 6 dBm, the acceptable BER of  $10^{-9}$  can be achieved if spectral power distortion could be maintained to within 33 %.

Many researches have been conducted to enable the high capacity, high data rates, and low-cost communication network services, among them by combining FSO with other technology. Dat *et al.* in [21] suggested hybrid method that combine optical fiber, millimeter-wave (mmWave), and optical wireless communications for indoor communications application. The proposed method was used to transmit 40-Gb/s mmWave signal in the 100-GHz band. The demonstrations proved the feasibility of the proposed scheme for ultra-high-speed communications with low-latency, spectral and energy-efficient, and cost-effective features to be implemented in the 5G or higher communication network.

Another hybrid technology was proposed by Nguyen *et al.* in [22] by conducting two experimental demonstrations with hybrid optical fiber, FSO, and RF wireless channels. First experiment with 5, 20 and 50 MHz bandwidths through 3 m RF wireless channels, 5 km standard single-mode fiber (SSMF), and 2 m turbulent FSO to transmit 64-quadrature amplitude modulation (QAM) signal indicated that atmospheric turbulence impact more on QAM with a high

bandwidth. Other experiment with 4/16/64-QAM signals through 50 km SSMF and 40 m FSO/RF wireless links at 20 MHz resulted in measured error vector magnitude (EVM) values of 12, 9, and 7.9%, respectively, which was below the minimum value as defined by 3rd generation partnership project (3GPP) specifications. Further observations also found that antenna misalignment angle to be less than  $3^\circ$  for indoor corridor transmission. Another testing of extended FSO link span for 25 GHz hybrid microwave photonic link (MPL) with 16-QAM at 10 Gb/s were done with simulation under the weak and strong turbulence conditions and showed that the proposed hybrid method can be implemented in 5G network practical applications.

For the encoding, OCDMA can be divided into non-coherent and coherent OCDMA. The encoding method for non-coherent OCDMA is unipolar encoding, while the coherent systems utilizing the bipolar encoding. The results of some researches proved that the performance of bipolar encoding is superior than the unipolar encoding therefore it is suitable for high-speed data transmission and real time applications. Patel *et al.* in [23] proposed a bipolar code with smaller code length based on double weight code pattern to increase the security against an eavesdropper with low-cost and low-complexity. The proposed bipolar code has the feature of reconfiguration at the transmitting end resulted in higher code confidentiality against unauthorized user. For the decoding part, complementary subtraction technique and SPD detection technique were implemented to reconstruct the original data. The evaluation results demonstrated that the proposed code has better performance in comparison with the existing extended quadratic codes (EQC) bipolar and M-sequence code switching techniques. Further observation also found that SPD detection technique has a better performance than complementary subtraction technique.

Another prove was presented by Ai-Khafaji *et al.* in [24] that compared two encoding methods, namely unipolar and bipolar encoding for SAC-OCDMA systems with the effect of intensity noise as the primary noise source. The

comparison was conducted for four SAC codes, i.e., Hadamard, MQC, balanced incomplete block design (BIBD), and zero cross-correlation (ZCC). The analysis results showed that ZCC code with zero cross-correlation property can support higher number of users and achieved high spectral efficiency than the other SAC codes. Furthermore, the results showed that bipolar encoding increases spectral efficiency over a unipolar system. In [25], Zefreh *et al.* proposed a power-cubic nonlinear preprocessor for spectral-phase-encoded ultrashort light pulse optical code division multiple access (SPE-OCDMA) system. The numerical results proved the superiority of the proposed system to improve the coherent SAC OCDMA system performance; especially in the high-power scenarios where MAI become the dominant noise.

Other observation was conducted by Hamza *et al.* in [26] by utilizing MD code for two-code keying scheme to generate bipolar encoding for SAC-OCDMA system. Several noises, such as PIIN, shot noise, and thermal noise were included in the analysis. Direct detection technique was implemented in the receiver-end. The results from numerical calculations and further verified with simulations proved that the proposed bipolar scheme achieved superior performance compare to the unipolar scheme with the improvement of 125% increment in the data rate at a BER of  $10^{-9}$  and  $K = 20$ .

Bipolar code also improves the spectral efficiency in the OCDMA System. Yen *et al.* in [27] performed the analysis and simulation of unipolar and bipolar code in the SAC-OCDMA system by utilizing Walsh-Hadamard codes as signature codes and included the PIIN effect to the system. The FGB were implemented in the encoder and decoder structure. The results showed that the BER performance of bipolar scheme was superior compare to the unipolar method. The spectral efficiency of the bipolar system was also higher than that of the unipolar scheme.

Similar research was presented by Al-Khafaji *et al.* in [28] by analyzing the spectral efficiency (SE) and BER of SAC-OCDMA system with bipolar scheme



of MQC, BIBD, ZCC, and Hadamard code. The system included intensity noise from simultaneous users as the primary source of noise. For the decoding, balanced photodetection was implemented to relieve the MAI. From the evaluation, cross-correlation value strongly effected the performance of the code, for example ZCC with cross-correlation can had relatively high SE and BER so that can be used to support more users at a transmission rate up to 2.5 Gbps. Another comparation was conducted between unipolar and bipolar scheme with the results that bipolar encoding improved the SE compared with unipolar scheme.

Several methods were demonstrated to improve the security aspect by employing the bipolar code. Gupta *et al.* in [29] analyzed bipolar double weight coding scheme for OCDMA system in comparison with existing bipolar M-sequence code, flexible cross-correlation (FCC), and without mapping MDW code. Different numbers of simultaneous users, obtained power, and data rate, were used in the performance analysis. Noises in OCDMA system, such as PIIN, shot, and thermal noise, were also counted in the analysis. The evaluation results indicated that the proposed system could increase the number of active users up to 186%, 140%, and 120% compare with the existing scheme. Further analysis showed that in order to achieved acceptable BER performance, the received power required by the proposed system is lower than another method. The proposed system also attained lower BER at high data rate compare with another existing scheme. In the security point of view, a greater number of users were secured against the eavesdropping in the proposed approach.

Further implementation of bipolar codes in non-coherent OCDMA was proved by Cha *et al.* in [30] to improve system performance. The used of bipolar codes stabilized the decision threshold in the receiving-end and further increased overall system performance. The requirement of complex threshold injection process was also alleviated with the use of bipolar codes. Simulation results

presented that OCDMA bipolar system could achieved  $10^{-8}$  BER at 15 km distance, which is increased by 7 km compared to unipolar OCDMA system.

Moreover, polarization domain exhibits the potential to improve the multiplexing gain in the OCDMA system. Tseng *et al.* in [31] proposed a compact codec for OCDMA system in free-space optics communication by using polarization spectral amplitude coding (P-SAC) and cyclic ternary perfect (CTP) codes. The proposed model utilized three values:  $\{-1, 0, +1\}$  of CTP codes to realize the polarization coding and the cyclic property of CTP codes to realized simple structure with moderate security in which each user only equipped with one arrayed-waveguide grating (AWG) router for encoding and two AWG routers for decoding the SAC signals. From theoretical analysis, the proposed method exhibited satisfactory SE performance compare with other techniques.

Further hybrid system was presented by Chang *et al.* in [32] that presented the hybrid spectral amplitude coding and polarization division multiplexing based optical code division multiple access (SAC/PDM-based OCDMA) for optical wireless communication. The M-sequence was utilized as a codeword and rewritten with FBGs based encoder. The MAI cancellation property of the proposed structure was investigated in terms of auto-correlation and cross-correlation at a wireless distance of 2 m and normal atmospheric temperatures. The experimental results showed that the proposed model could achieved twice spectral efficiency and number of simultaneous active users compare to the traditional SAC-OCDMA system.

Similar work was demonstrated by Chang *et al.* in [33] that proposed the two-dimensional SAC/PDM-based OCDMA in the wireless optical transmission channel. Under normal atmospheric temperatures, the experiments utilized M-sequence as signature code and transmitted the optical coded and polarized signal. The experiment investigated that the desired signal could be easily extracted, both for horizontal and vertical polarization state. The MAI cancellation property of the proposed scheme was further checked using the auto-correlation (matched)

and cross-correlation (unmatched) scenarios. The experiments have showed that the proposed 2D SAC/PDM-based OCDMA scheme had twice spectral efficiency and simultaneous active users compare to the traditional SAC-OCDMA scheme.

Jen *et al.* in [34] introduced an alternative structure for SPC-OCDMA configuration structured over AWG router with differential photodetectors technique. The numerical results indicated that the proposed scheme could improve the signal to noise ratio (SNR) up to 9 dB compare to the conventional unipolar and bipolar SAC structures with Walsh-Hadamard codes when PIIN was included in the calculation and degree of polarization (DOP) equals to 1.

Another implementation of SPC-OCDMA system for radio-over-fiber (RoF) transmissions was investigated by Yen *et al.* in [35]. AWG routers and polarization beam splitter (PBS) devices were utilized to generate the SPC codes of Walsh-Hadamard codes while in the receiving-end, a differential photodetector was used. The PIIN effect was effectively cancelled out by transmitting two orthogonal states of polarization radio base station (SOP RBS) from one spectrum encoder. When the number of simultaneous active RBSs increased, the limitations in PIIN reduction become apparent. As compared to the complementary SPC scheme with a single-balanced detection system, the proposed approach potentially eliminated the MAI with a 3 dB increase in carrier-to-noise ratio (CNR).

Further model combines the PDM and OFDM modulation for radio-over-fiber. Morant *et al.* in [36] introduced the hybrid PDM and OFDM modulation system in order to increase the system capacity. The experiments were conducted for three users by transmitting OFDM signals with ultrawide band (UWB) subcarrier multiplexed (SCM) configuration. The results showed that PDM transmission would achieve an aggregated bit rate of 1.2 Gbit/s with a spectral efficiency of 0.76 bit/s/Hz. The feasibility of the proposed structure to transmit SCM multi-user OFDM-UWB with PDM transmission over a passive optical network with 25 km SSMF was verified with power levels of 5 dBm.

The effect of atmospheric turbulence on the polarized system was observed by Bai *et al.* in [3] by testing the polarization-based transceiver for OCDMA systems over a FSO channel. The study was conducted in the presence of atmospheric turbulence, which was modeled using the Gamma-Gamma distribution. The MAI and optical noise effect was also included in the mathematical model. The findings showed that optical scintillation caused by atmospheric turbulence and the obtained optical power had the greatest impact on the proposed method. Further findings showed that, in the presence of atmospheric turbulence, the proposed scheme outperformed the OOK modulation scheme in terms of BER. Another analysis also found that prime number, which is one of the metric parameters, could increase the overall system performance when it is large.

For the modulation, PM exhibits the simple structure with acceptable performance of the system. Gao *et al.* in [37] utilized single PM for simultaneous generation of differential phase-shift keying (DPSK) data modulation and time-domain spectral phase encoding/decoding (SPE/SPD) in OCDMA system. The proposed scheme was observed both with simulation and experiments which exhibited that the performance of proposed structured was affected by dispersion mismatch between the encoding and decoding, code transition, and the transmission fiber dispersion. The experiment demonstrated the transmission of 16 chip, 40 Gchip/s optical carrier pattern, and 2.5 Gb/s DPSK data modulation generated by single PM over 34 km fiber with successful DPSK data decoding at the receiver-end.

Meanwhile, Wang *et al.* in [38] introduced the simultaneous time domain SPE signal generation and DPSK data modulation for OCDMA application. In the decoding end, AWG and variable-bandwidth-spectrum-shaper based devices were implemented to decode the signal in spectral domain. In the simulations and experiments, the effects of fiber dispersion, light pulse width, and timing error on coding efficiency were taken into account. The experiments results verified that

the proposed structure successfully transmitted SPE signal with 8 chip, 20 GHz/chip optical code patterns modulated with 2.5 Gbps DPSK data over 34 km fiber with acceptable BER performance. The proposed scheme has the advantages of simple structure and higher data confidentiality for OCDMA application.

Different signature codes for SAC-OCDMA have been introduced and proposed to improve the system performance, among them that commonly used is MQC code, Walsh-Hadamard code, M-sequence code, and MD code.

Huang *et al.* in [39] proposed two-dimensional MQC codes with M-sequence codes for SAC-OCDMA system. The effects of quantum shot noise, thermal noise, and PIIN had been included in the system evaluation. The analysis of system performance indicated that the combine MQC/M-Matrices had higher performance compare to the M-matrices coding scheme.

Another implementation of MQC codes for SAC-OCDMA system with a fixed in-phase cross-correlation value of 1 was proposed by Wei *et al.* in [40]. The tunable chirped FBGs based encoder and decoder were also proposed in [40]. The impact of PIIN, shot noise, and thermal noise were counted in the analysis. The results indicated that the proposed codes could depress the intensity noise and increase the system performance.

The hybrid system of WDM and SAC-OCDMA to improve the capacity and security of the networks was proposed by Ashour *et al.* in [41]. MQC code was used as signature code in the proposed hybrid system. With the overlaid scheme of SAC-OCDMA into a multichannel WDM system, the security was increased due to complexity increasing in the decoding process compare to the conventional SAC-OCDMA. The notch filters and APD photodetectors were implemented in the structure to improve the proposed system performance in accordance with the interference effects.

Walsh-Hadamard codes was applied as a signature code by Huang *et al.* in [42] for optical coder/decoder structure AWG routers. The proposed model has the benefit of simple and low-cost since each user only need two AWG routers to

complete the encoding and decoding for complementary keying with complementary Walsh–Hadamard code in OCDMA system. The PIIN effect was also included in the analysis and the results indicated that the proposed system can effectively decrease the MAI effect and increase the BER performance compared to conventional OOK method. The increasing of simultaneous number of users. Furthermore, when the total number of users is increased, the proposed codecs do not accumulate the insertion loss.

Yang *et al.* in [43] utilized the cyclic properties of AWG routers and M-sequence codes to realize a compact and low-cost SAC-OCDMA codecs. The users can use the same hardware in the coding process while maintain the properties of MAI cancellation in SAC-OCDMA system.

MD codes with zero cross-correlation property was introduced by Abd *et al.* in [44] for SAC-OCDMA system. In comparison to other SAC-OCDMA codes, MD code has zero cross-correlation and a simple code construction. MD code also has flexibility in defining code parameters, such as the number of users, code weight, and cross-correlation. With MD code, the increasing of user will not impact on code weight increment. With the feature of zero cross-correlation, MD code effectively eliminate MAI, resulted in excellent performance for OCDMA system. Theoretical analysis revealed that MD code has superior performance compared with MQC code and Random Diagonal (RD) code. Further simulations results illustrated that BER of  $3.5 \times 10^{-14}$  could be achieved with MD code for 10 users with 10 Gb/s data rate.

In order to verify the ability of MD code to relieve MAI, Motealleh *et al.* in [45] applied MD code with 10 users' scheme in SAC-OCDMA to remove the MAI effect. With transmission rate of 15 Gb/s for each user, the demonstrated system could achieve maximum BER of  $10^{-9}$  for 30 km long single-mode fiber optic. Since the MD code has zero cross-correlation, the architecture of encoder and decoder is simple. In the observation, the effect of beat noise and thermal

noise were included and direct detection technique was applied in the receiver-end.

Further, MD code was applied for hybrid system. Fayadh *et al.* in [46] proposed the hybrid model for OCDMA system by utilizing SCM SAC. The simulation of the proposed model employed the MD code and counted in the effect of atmospheric attenuations. According to the simulation results, an acceptable BER could be reached for a distance or range of 500 m in heavy rain and a distance or range of 2,500 m in drizzle rain. Further RoF simulations for UWB signals revealed that the current scheme is more suited for indoor application.

Performance comparison between different codes was observed in another work. Under the nonlinear effect of four-wave mixing (FWM) and cross-phase modulation (XPM), Rana *et al.* evaluated the performance of MD code, multi-weight code, and Walsh-Hadamard code in [47]. According to the simulation results, the MD code with zero cross-correlation property outperformed the other two codes.

Another comparison was conducted by Kaur *et al.* in [48] for different SAC, namely Walsh-Hadamard, DDW, MDW, EDW, and MD codes, for OCDMA systems with homogeny input parameters. The comparison was done for the parameters of data speeds, extinction ratio, bit error rate, photonic efficiencies of photodetectors, frequency bands, advanced modulation formats, signal-to-noise ratio, decision algorithms, forward error correction, and photodetector noises. Based on simulations, the advantages and drawbacks of each SAC-OCDMA codes were concluded along with the recent progress in the technology, literature comparison, future scope, encryption-decryption techniques, all-optical methods, practical works on SAC throughout the world, and applications of the SAC-OCDMA codes. EDW codes outperformed Walsh-Hadamard codes in terms of BER, SNR, and eye height, whereas Walsh-Hadamard codes had fewer spectral interference from desired chip combinations.

## **Chapter 3 Design and Simulation Setup of The Proposed Bipolar OCDMA Scheme**

The third chapter present the design of the proposed bipolar OCDMA architecture and the simulation setup. The proposed system implements the bipolar codes for OCDMA in the FSO network by utilizing phase modulator to achieved the polarization coding. The design includes the proposed structure of the encoder and decoder along with the correlation analysis to achieve the MAI elimination feature of the proposed system. Simulation setup section depicts the components used in the simulation equipped with parameter of each component. Noises and channel model applied in the simulation also revealed in this section.

### **3.1 Design of Bipolar OCDMA System with Phase Modulator Scheme**

The proposed bipolar OCDMA scheme is developed to transmit bipolar data signals over a common FSO channel. Each user data is created by pseudo-random bit sequence (PRBS). Phase-shift keying (PSK) pulse generator along with electrical bias, and electrical gain were applied as the modulation signal generator. A phase modulator is used to encode each user's data bit into an optical signal, which is then transmitted to the decoder-end through an FSO channel. Polarization splitters are utilized as polarization shift keying devices. Optical circulator and series of uniform FBG are used as decoder devices with balanced photodetection method.

In the single-user scheme of Bi-OCDMA, a family of M-sequences is used to create all sequences of the same length. In order to maintain the cross-correlation property for MAI elimination, zero-padding method was implemented by adding zero after the last bit of the original M-sequence. The resulted code



family is named as modified M-sequence in the rest of this paper. Let  $X_1$  be a codeword derived from modified M-sequences as follows:

$$X_1 = [x_1(1), x_1(2), \dots, x_1(N), z_p] \quad (42)$$

where  $x_k(i)$  is the  $i$ -th element of the  $k$ -th codeword of the modified M-sequence,  $N$  is the modified M-sequence code length, and  $Z_p$  is the zero-padding element. Afterwards, the cyclic property of M-sequences is used to produce codewords of the same length  $N$  through an equation of  $X_{(k+1)} = T^k X_1$ , where  $T$  is the shifting operator vectors cyclically to the right by one position and  $k$  is the number of cyclic shifts to the right side.

The implementation of polarization coding and modulation techniques for Bi-OCDMA schemes using modified M-sequence codes can be described as follows: when the data bit of the  $k$ -th user is "1", the transmitted optical signal is modulated with vertical (or horizontal) polarization state if the chip of codeword is "0" (or "1"), respectively. However, when the  $k$ -th user's data bit is "0", if the chip of codeword is "0" (or "1"), the transmitted optical signal is modulated with horizontal (or vertical) polarization state, respectively.

For example, with the matrix of the proposed modified M-sequence code of length 8 in the bipolar scheme can be expressed as follows.

$$X = \begin{bmatrix} 1 & -1 & 1 & 1 & 1 & -1 & -1 & -1 \\ -1 & 1 & 1 & 1 & -1 & -1 & 1 & -1 \\ 1 & 1 & 1 & -1 & -1 & 1 & -1 & -1 \\ 1 & 1 & -1 & -1 & 1 & -1 & 1 & -1 \\ 1 & -1 & -1 & 1 & -1 & 1 & 1 & -1 \\ -1 & -1 & 1 & -1 & 1 & 1 & 1 & -1 \\ -1 & 1 & -1 & 1 & 1 & 1 & -1 & -1 \end{bmatrix} = \begin{bmatrix} 1 & 0 & 1 & 1 & 1 & 0 & 0 & 0 \\ 0 & 1 & 1 & 1 & 0 & 0 & 1 & 0 \\ 1 & 1 & 1 & 0 & 0 & 1 & 0 & 0 \\ 1 & 1 & 0 & 0 & 1 & 0 & 1 & 0 \\ 1 & 0 & 0 & 1 & 0 & 1 & 1 & 0 \\ 0 & 0 & 1 & 0 & 1 & 1 & 1 & 0 \\ 0 & 1 & 0 & 1 & 1 & 1 & 0 & 0 \end{bmatrix} - \begin{bmatrix} 0 & 1 & 0 & 0 & 0 & 1 & 1 & 1 \\ 1 & 0 & 0 & 0 & 1 & 1 & 0 & 1 \\ 0 & 0 & 0 & 1 & 1 & 0 & 1 & 1 \\ 0 & 0 & 1 & 1 & 0 & 1 & 0 & 1 \\ 0 & 1 & 1 & 0 & 1 & 0 & 0 & 1 \\ 1 & 1 & 0 & 1 & 0 & 0 & 0 & 1 \\ 1 & 0 & 1 & 0 & 0 & 0 & 1 & 1 \end{bmatrix} = C_v - \bar{C}_H \quad (43)$$

In (43),  $x_k$  denotes the  $k$ -th row in the modified M-sequence matrix, which can be split into two unipolar codes,  $C_{kV}$  and  $\bar{C}_{kH}$ . The positive and negative elements of  $x_k$  are denoted by these two codes, which form a complementary pair in the set  $\in \{0,1\}$ . In this process,  $x_k$  is sent for the  $k$ -th user's data bit "1", while the complement row of  $x_k$  (denoting  $\bar{x}_k$ ) is sent for the  $k$ -th user's data bit "0". The

matrix formed when all users sent a data bit of “1” is denoted by  $(C_V - \bar{C}_H)$ . The modified M-sequence matrix can then be mapped to the wavelength domain, where two orthogonal polarization states are present (vertical and horizontal). The vertical ( $C_V$ ) and horizontal ( $\bar{C}_H$ ) polarization states are represented by the first and second matrices, respectively. In the same way, the complement matrix of  $X$  can be decomposed as follows:

$$\bar{X} = \begin{bmatrix} -1 & 1 & -1 & -1 & -1 & 1 & 1 & 1 \\ 1 & -1 & -1 & -1 & 1 & 1 & -1 & 1 \\ -1 & -1 & -1 & 1 & 1 & -1 & 1 & 1 \\ -1 & -1 & 1 & 1 & -1 & 1 & -1 & 1 \\ -1 & 1 & 1 & -1 & 1 & -1 & -1 & 1 \\ 1 & 1 & -1 & 1 & -1 & -1 & -1 & 1 \\ 1 & -1 & 1 & -1 & -1 & -1 & 1 & 1 \end{bmatrix} = \begin{bmatrix} 0 & 1 & 0 & 0 & 0 & 1 & 1 & 1 \\ 1 & 0 & 0 & 0 & 1 & 1 & 0 & 1 \\ 0 & 0 & 0 & 1 & 1 & 0 & 1 & 1 \\ 0 & 0 & 1 & 1 & 0 & 1 & 0 & 1 \\ 0 & 1 & 1 & 0 & 1 & 0 & 0 & 1 \\ 1 & 1 & 0 & 1 & 0 & 0 & 0 & 1 \\ 1 & 0 & 1 & 0 & 0 & 0 & 1 & 1 \end{bmatrix} - \begin{bmatrix} 1 & 0 & 1 & 1 & 1 & 0 & 0 & 0 \\ 0 & 1 & 1 & 1 & 0 & 0 & 1 & 0 \\ 1 & 1 & 1 & 0 & 0 & 1 & 0 & 0 \\ 1 & 1 & 0 & 0 & 1 & 0 & 1 & 0 \\ 1 & 0 & 0 & 1 & 0 & 1 & 1 & 0 \\ 0 & 0 & 1 & 0 & 1 & 1 & 1 & 0 \\ 0 & 1 & 0 & 1 & 1 & 1 & 0 & 0 \end{bmatrix} = \bar{C}_V - C_H \quad (44)$$

As a result, the optical signal  $R_k$  sent from the  $k$ -th user's encoder can be calculated with (30).

Table 3.1 Modified M-sequence codes of length 8 with spectral polarization coding

User No.	Signature Sequence	Data Bit	Transmitted Optical Polarized Signal							
			$H$				$V$			
#1	1 0 1 1 1 0 0 0	0	$\lambda_1$	$\lambda_3$	$\lambda_4$	$\lambda_5$	$\lambda_2$	$\lambda_6$	$\lambda_7$	$\lambda_8$
		1	$\lambda_2$	$\lambda_6$	$\lambda_7$	$\lambda_8$	$\lambda_1$	$\lambda_3$	$\lambda_4$	$\lambda_5$
#2	0 1 1 1 0 0 1 0	0	$\lambda_2$	$\lambda_3$	$\lambda_4$	$\lambda_7$	$\lambda_1$	$\lambda_5$	$\lambda_6$	$\lambda_8$
		1	$\lambda_1$	$\lambda_5$	$\lambda_6$	$\lambda_8$	$\lambda_2$	$\lambda_3$	$\lambda_4$	$\lambda_7$
#3	1 1 1 0 0 1 0 0	0	$\lambda_1$	$\lambda_2$	$\lambda_3$	$\lambda_6$	$\lambda_4$	$\lambda_5$	$\lambda_7$	$\lambda_8$
		1	$\lambda_4$	$\lambda_5$	$\lambda_7$	$\lambda_8$	$\lambda_1$	$\lambda_2$	$\lambda_3$	$\lambda_6$
#4	1 1 0 0 1 0 1 0	0	$\lambda_1$	$\lambda_2$	$\lambda_5$	$\lambda_7$	$\lambda_3$	$\lambda_4$	$\lambda_6$	$\lambda_8$
		1	$\lambda_3$	$\lambda_4$	$\lambda_6$	$\lambda_8$	$\lambda_1$	$\lambda_2$	$\lambda_5$	$\lambda_7$
#5	1 0 0 1 0 1 1 0	0	$\lambda_1$	$\lambda_4$	$\lambda_6$	$\lambda_7$	$\lambda_2$	$\lambda_3$	$\lambda_5$	$\lambda_8$
		1	$\lambda_2$	$\lambda_3$	$\lambda_5$	$\lambda_8$	$\lambda_1$	$\lambda_4$	$\lambda_6$	$\lambda_7$
#6	0 0 1 0 1 1 1 0	0	$\lambda_3$	$\lambda_5$	$\lambda_6$	$\lambda_7$	$\lambda_1$	$\lambda_2$	$\lambda_4$	$\lambda_8$
		1	$\lambda_1$	$\lambda_2$	$\lambda_4$	$\lambda_8$	$\lambda_3$	$\lambda_5$	$\lambda_6$	$\lambda_7$
#7	0 1 0 1 1 1 0 0	0	$\lambda_2$	$\lambda_4$	$\lambda_5$	$\lambda_6$	$\lambda_1$	$\lambda_3$	$\lambda_7$	$\lambda_8$
		1	$\lambda_1$	$\lambda_3$	$\lambda_7$	$\lambda_8$	$\lambda_2$	$\lambda_4$	$\lambda_5$	$\lambda_6$

Table 3.1 shows the modified M-sequences code of length 8 with bipolar

schemes. The letters  $H$  and  $V$  stand for horizontal and vertical polarized optical signals, respectively.

The following correlation must be obtained in order to implement modified M-sequence codes of length  $N$  in the proposed schemes:

$$\theta_{xx}(k,l) = \sum_{i=1}^N (c_{kV}(i) - \bar{c}_{kH}(i))(c_{lV}(i) - \bar{c}_{lH}(i)) = \begin{cases} N, & k=l \\ N/2, & k \neq l \end{cases} \quad (45)$$

$$\theta_{\bar{x}\bar{x}}(k,l) = \sum_{i=1}^N (c_{kV}(i) - \bar{c}_{kH}(i))(\bar{c}_{lV}(i) - c_{lH}(i)) = \begin{cases} 0, & k=l \\ N/2, & k \neq l \end{cases} \quad (46)$$

The modified M-sequence code with code length 8 was used as the signature code. Based on Table 3.1, user#1 is assigned with the codeword  $X = [\lambda_{1H}, \lambda_{2V}, \lambda_{3H}, \lambda_{4H}, \lambda_{5H}, \lambda_{6V}, \lambda_{7V}, \lambda_{8V}]$  for user data bit of “0” and  $\bar{X} = [\lambda_{1V}, \lambda_{2H}, \lambda_{3V}, \lambda_{4V}, \lambda_{5V}, \lambda_{6H}, \lambda_{7H}, \lambda_{8H}]$  for user data bit of “1”.

From (45) and (46), the modified M-sequence codes can be implemented in the proposed system to alleviate MAI by using balanced subtraction detection method. The corresponding FSO system based on Bi-OCDMA schemes can be constructed using these derivations.

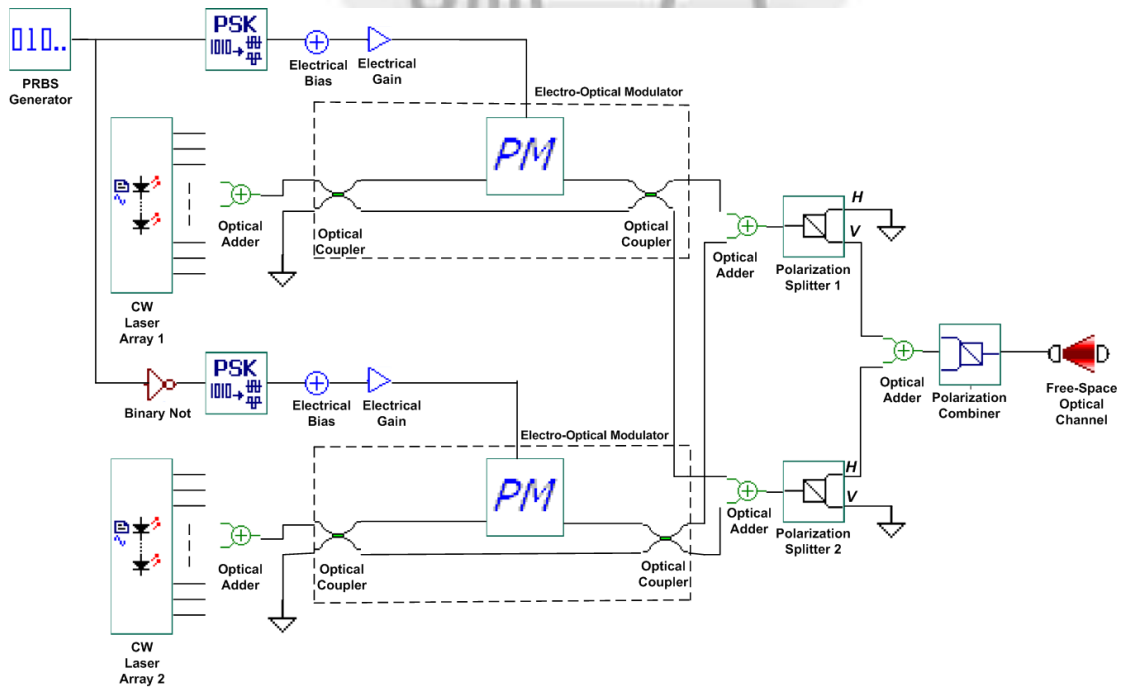


Figure 3.1 Proposed Bi-OCDMA encoder with phase modulator scheme

Figure 3.1 illustrates the design of the proposed encoder, which is composed of two CW laser array as light source, one PRBS generator as the bit sequence generator, two set of electrical bias, electrical gain, and PSK pulse generator as modulation signal generator, two phase modulators for optical signals modulation, four optical couplers, several optical adders, an inverter, two polarization splitters ( $0^\circ$  and  $90^\circ$ ), and a polarization combiner.

First, two CW laser arrays are used to emit specific wavelengths based on the modified M-sequence codeword assigned to them, where CW laser array#1 (or #2) sends out the wavelength correlated with chip “1” (or “0”) of the codeword depends on the users’ data bit of “0” (or “1”). As showed in Table 3.1, since the modified M-sequence codeword  $X_1 = [10111000]$  is assigned to user#1, the wavelengths of CW laser array#1 and #2 are  $(\lambda_1, \lambda_3, \lambda_4, \lambda_5)$  and  $(\lambda_2, \lambda_6, \lambda_7, \lambda_8)$ , respectively. According to the user data bit, the electrical signals are generated by the PSK pulse generator. Since the in-phase output of PSK pulse generator is -1 and 1, electrical bias and electrical gain are utilized to modify it into 0 and 1 for the modulating signal of the phase modulator. Next, the electrical signal is sent to the EOM for optical signals modulation. As can be seen in Figure 3.1, two optical couplers and one phase modulator are implemented to form the EOM function. Output optical signals from the phase modulator can be formulated with (5).

Further, the modulated signals are distributed to one of the outputs from optical coupler depends on the user data bit. Output of the optical coupler can be observed by (4). In this simulation, 0 dB additional loss was added in the optical coupler (i.e.  $\alpha$  equals to 1). Conjugate parameter was used in the simulation (i.e.  $p = -1$ ) with coupling coefficient equals to 0.5. The output from the first optical coupler can be evaluated as:

$$\begin{pmatrix} E_{1out,C1} \\ E_{2out,C1} \end{pmatrix} = \begin{pmatrix} \sqrt{0.5} & -j\sqrt{0.5} \\ -j\sqrt{0.5} & \sqrt{0.5} \end{pmatrix} \begin{pmatrix} E_{1in} \\ 0 \end{pmatrix} = \begin{pmatrix} \sqrt{0.5}E_{1in} \\ -j\sqrt{0.5}E_{1in} \end{pmatrix} \quad (47)$$

The phase deviation of  $180^\circ$  was applied in the simulation. When the user's data bit is "0," the following formula can be used to measure PM output optical signals:

$$E_{out,PM}(t) = \sqrt{0.5}E_{in} \cdot \exp(j.180^\circ.1) = -\sqrt{0.5}E_{in} \quad (48)$$

The modulated signals are distributed to one of the optical coupler outputs depends on the data bit of user. Optical signals that passed through the second optical coupler can be observed as:

$$\begin{pmatrix} E_{1out,C2} \\ E_{2out,C2} \end{pmatrix} = \begin{pmatrix} \sqrt{0.5} & -j\sqrt{0.5} \\ -j\sqrt{0.5} & \sqrt{0.5} \end{pmatrix} \begin{pmatrix} -\sqrt{0.5}E_{in} \\ -j\sqrt{0.5}E_{in} \end{pmatrix} = \begin{pmatrix} -E_{in} \\ 0 \end{pmatrix} \quad (49)$$

When the user's data bit is "1", PM output optical signals can be calculated with:

$$E_{out,PM}(t) = \sqrt{0.5}E_{in} \cdot \exp(j.180^\circ.0) = \sqrt{0.5}E_{in} \quad (50)$$

Optical signals that passed through the second optical coupler can be observed as:

$$\begin{pmatrix} E_{1out,C2} \\ E_{2out,C2} \end{pmatrix} = \begin{pmatrix} \sqrt{0.5} & -j\sqrt{0.5} \\ -j\sqrt{0.5} & \sqrt{0.5} \end{pmatrix} \begin{pmatrix} \sqrt{0.5}E_{in} \\ -j\sqrt{0.5}E_{in} \end{pmatrix} = \begin{pmatrix} 0 \\ -jE_{in} \end{pmatrix} \quad (51)$$

From the mathematical derivation, when the user's data bit is "0" (or "1"), only the first (or second) output of optical couplers will have the signals and pass into the upper (or lower) polarization splitter to polarize the signals into vertical (or horizontal) polarization state. Then, these polarized signals are combined through the polarization combiner. For example, if the data bit of user#1 is "0", the polarization combiner output corresponds to  $[\lambda_1, \lambda_3, \lambda_4, \lambda_5]_H$  and  $[\lambda_2, \lambda_6, \lambda_7, \lambda_8]_V$ ; however, if the bit of user#1 is "1", the polarization combiner output corresponds to  $[\lambda_2, \lambda_6, \lambda_7, \lambda_8]_H$  and  $[\lambda_1, \lambda_3, \lambda_4, \lambda_5]_V$ . Finally, the output of the encoder is transmitted via a FSO channel.

Figure 3.2 illustrates the structure of the proposed Bi-OCDMA decoder, which contains a polarization splitter, two optical circulators, two series of uniform FBGs, two optical adders, two photodetectors, two low pass Bessel filters, and one electrical subtractor to complete the bipolar scheme with balanced photodetection by subtracting the upper and lower signals to minimize the MAI.

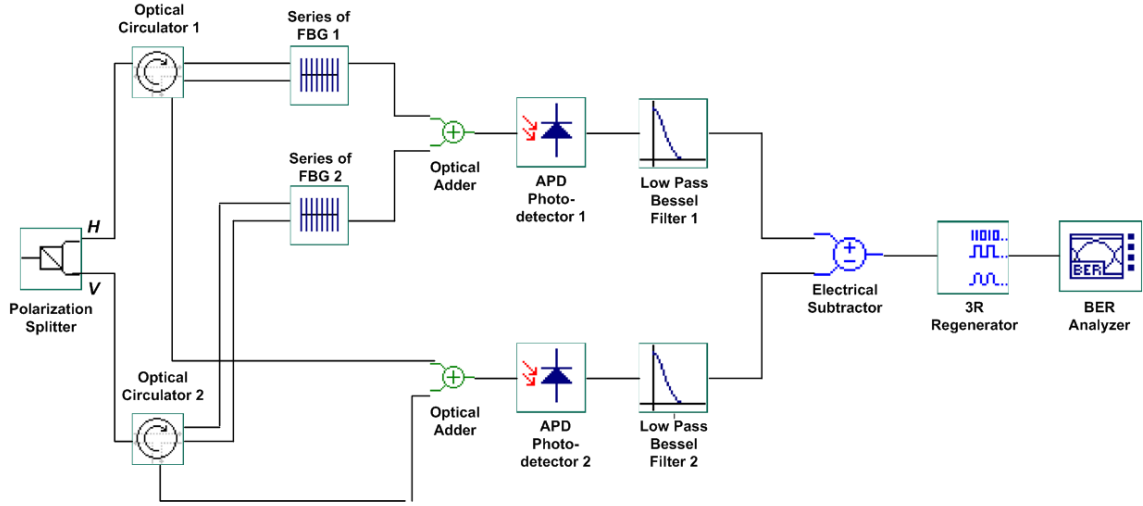


Figure 3.2 Proposed Bi-OCDMA decoder with phase modulator scheme

The obtained optical signals are depolarized by the polarization splitter before being sent to the two circulators, each of which has a port#2 connected to a series of uniform FBGs. The wavelengths of these two series of uniform FBGs are determined by the assigned codewords. For example, the series of upper (or lower) uniform FBGs reflect the central wavelengths of  $\lambda_1, \lambda_3, \lambda_4,$  and  $\lambda_5$  (or  $\lambda_2, \lambda_6, \lambda_7,$  and  $\lambda_8$ ) that correspond to chip “1” (or “0”) of the codeword  $X_1 = [10111000]$  in uniform FBG decoder for user#1. The reflected signals are collected in the upper optical adder, while the transmitted signals of the two series of uniform FBGs are collected in port#3 of the circulator. The lower optical adder collects optical signals from each of the two optical circulators' port#3.

According to (33), the optical signal ( $R_v$ ) with specific wavelengths corresponding to the position of the “1s” of  $\bar{c}_{kV}$  is reflected by the  $k$ -th user's uniform FBGs-based decoder, and then arrives at the lower optical adder. Simultaneously, the optical signal ( $R_v$ ) with remainder wavelengths corresponding to the position of the “1s” of  $C_{kV}$  is sent to the upper optical adder. Conversely, the optical signal ( $R_h$ ) with specific wavelengths corresponding to the position of the “1s” of  $C_{kH}$  arrives at the upper optical adder after a series of lower uniform FBGs. Concurrently, the optical signal ( $R_h$ ) with reflected

wavelengths is sent to the lower optical adder concurrently.

The output signals of the upper and lower optical adder then pass to the photodetectors for electrical subtraction to complete the balanced detection. The approach is detailed in the following equation.

$$\theta_{xj}(k,l) - \theta_{x\bar{j}}(k,l) = \begin{cases} N, & \text{if } x = j, k = l \\ -N, & \text{if } x = \bar{j}, k = l \\ 0, & \text{otherwise} \end{cases} \quad (52)$$

where  $j$  and  $\bar{j}$  are the desired users assigned and complementary optical codewords. Finally, a 3R regenerator is used to determine the desired user's data bit. The BER and Q-factor are then measured with the BER analyzer. Mathematically, the BER of the proposed Bi-OCDMA can be evaluated with [49]:

$$BER = \frac{1}{2} \operatorname{erfc} \left( \sqrt{\frac{SNR}{2}} \right) \quad (53)$$

where  $SNR$  indicates the signal-to-noise ratio of the proposed system and  $\operatorname{erfc}$  denotes the complementary error function in time that can be calculated by [50]:

$$\operatorname{erfc} = \frac{2}{\sqrt{\pi}} \int_x^{\infty} \exp(-t^2) dt \quad (54)$$

In the simulation, minimum log of BER was adopted instead of minimum BER to simplify the analysis of the system performance [51]:

$$\operatorname{Min}\{\log(BER)\} = \log_{10} BER \quad (55)$$

The correlation between the BER and Q-factor can be derived as [52]:

$$BER = \frac{1}{2} \operatorname{erfc} \left( \frac{Q}{\sqrt{2}} \right) \quad (56)$$

Figure 3.3 shows the proposed encoder/decoder architecture for the multi-user scheme with two users. The higher multi-user scheme can be expanded with the same architecture from the single-user scenario.

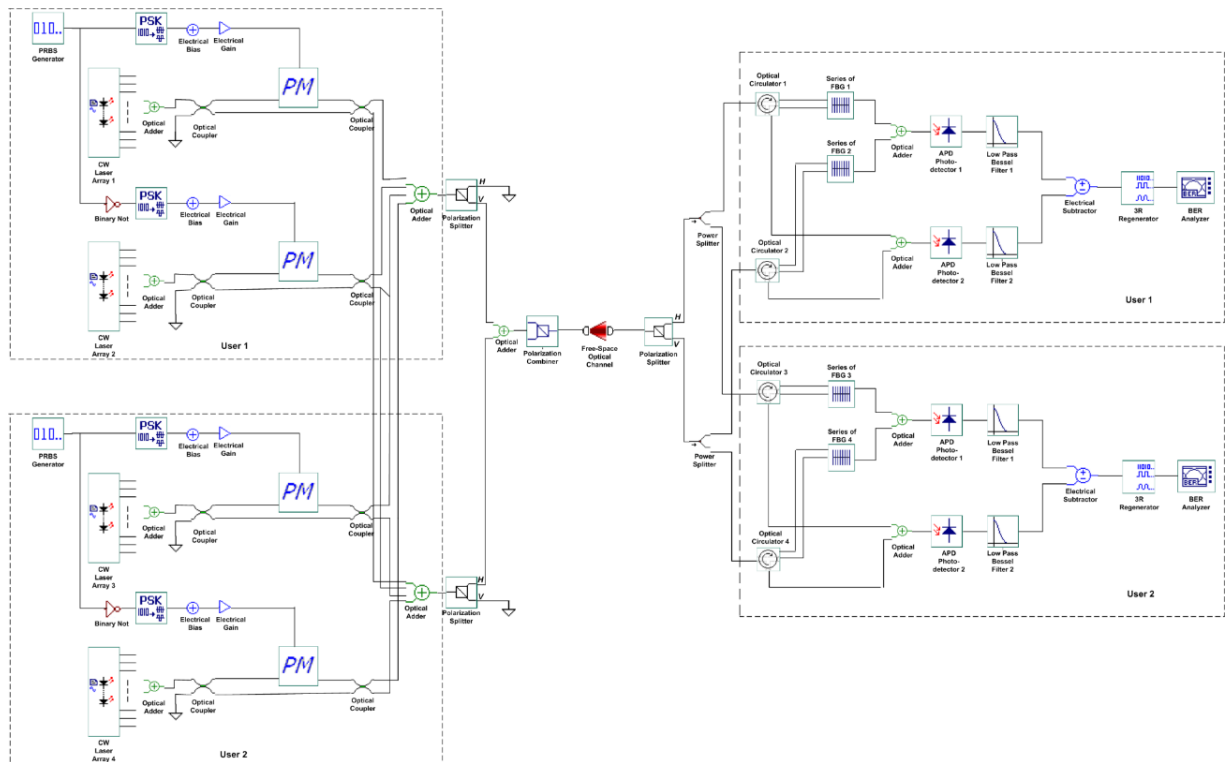


Figure 3.3 Proposed Bi-OCDMA system with phase modulator scheme for two users

### 3.2 Simulation Setup of Bipolar OCDMA System with Phase Modulator Scheme

This section presents the components used for simulation along with the applied parameter. Noises in the optical system and channel model that implemented in the simulation are described in this section.

#### 3.2.1 Components of Bipolar OCDMA System with Phase Modulator Scheme

The simulation was conducted with well-known optical system software, OptiSystem version 10. Based on architecture depicted in Figure 3.1 and 3.2, the first simulation was conducted with single-user scheme to prove the feasibility of the proposed Bi-OCDMA scheme. The second simulation was conducted with the scheme showed in Figure 3.3 to testify the proposed Bi-OCDMA in different channel condition by utilizing several SAC codes.



The components in the OptiSystem that being implemented in the simulation for single-user scheme are listed in Table 3.2.

Table 3.2 Components for single-user bipolar OCDMA simulation


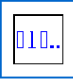




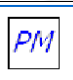

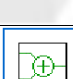

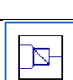













No.	Component	Symbol	Amount
1.	CW Laser Array		2
2.	PRBS Generator		1
3.	Binary Not		1
4.	PSK Pulse Generator		2
5.	Electrical Bias		2
6.	Electrical Gain		2
7.	Phase Modulator		2
8.	Optical Coupler		4
9.	Optical Adder		7
10.	Polarization Splitter		3
11.	Polarization Combiner		1
12.	Ground		4
13.	Free-Space Optical Channel		1
14.	Optical Circulator		2

Table 3.2 Components for single-user bipolar OCDMA simulation (continue)

No.	Component	Symbol	Amount
15.	Uniform FBG		2 Set
16.	PIN Photodiode		2
17.	APD		2
18.	Low-Pass Bessel Filter		2
19.	Electrical Subtractor		1
20.	3R Generator		1
21.	BER Analyzer		1
22.	Optical Spectrum Analyzer		1
23.	Oscilloscope		1
24.	White Light Source		1

CW laser array emits an array of CW lasers as light source. The linewidth of the CW laser array applied in this simulation is 10 MHz with initial phase of 0 degree. For the purpose of polarization coding, azimuth of CW laser array was set to 45 degree. The sample rate was arranged to follow the sample rate of the system. The power of the CW laser array was set to 0 dBm in order to minimize the non-linear effect. From the nature of narrow optical beam, CW laser was applied to reduce the atmospheric attenuation effect. A narrow beam concentrates the transmitting signal and reduces power loss, resulting in increased received power. The narrower the laser beam, the better the signal quality and the higher the system security. As a result, the BER rises as the beam divergence rises.

The user data bit to be transmitted over the proposed system was generated using a PRBS generator. According to the operation modes specified in the parameter, the PRBS generator generates a pseudo random binary sequence. To approximate the characteristics of random data, the bit sequence is generated. There are five different operation modes to generate the bit sequence, i.e.:

1. Probability: in this mode, random number generator is implemented, in which mark probability that define the probability of ones in the sequence is specified in the parameter. In default, the probability is set to 0.5.
2. Order: in this mode, a sequence is generated based on the Order  $k$  with period of  $2k - 1$  where the order is defined in the parameter.
3. Alternate: this mode will generate alternate sequence between ones and zeros.
4. Ones: this mode will generate all one sequence.
5. Zeros: this mode will generate all zero sequence.

In the simulation, order mode was applied with order of:

$$order = \frac{\log(sequence\_length)}{\log(2)} \quad (57)$$

Bit rate of PRBS generator is the same with the bit rate of the system. Generate random seed was implemented in the simulation to checking the system behaviour and the flexibility of the system where the system should give an approximately equal output when there is no specific pattern of bit stream. The binary sequence of  $N$  bits generated by PRBS generator can be evaluated with:

$$N = T_w B_r \quad (58)$$

$$N_G = N - n_l - n_t \quad (59)$$

where  $T_w$  is time window,  $B_r$  is bit rate parameter,  $N_G$  is the number of bits generated,  $n_l$  and  $n_t$  is the number of leading zeros and trailing zeros. In this simulation, leading zeros and trailing zeros were set to 0. Inverter (binary not) component will inverse the binary inputs and was used in order to inverse the sequence generated by PRBS generator.

PSK pulse generator is used to produce the modulation signal for phase modulator. PSK pulse generator is implemented to generate two parallel M-ary electrical signals from binary signals by utilizing PSK modulation. The phase of a signal may be varied depending on the source symbols when transmitting data. The phase values are taken from the set of angles:

$$\varphi_i = \left( \frac{2\pi}{M}(i-1) + \phi \right) \quad (60)$$

where  $\phi$  is the phase offset,  $i = 1, 2, \dots, M$ ,  $M$  is the number of possible sequences of binary digits, and can be evaluated with:

$$M = 2^h \quad (61)$$

where  $h$  denotes the number of bits per symbol. The in-phase and the quadrature-electrical signals will have amplitudes according to:

$$I_i = \cos(\varphi_i) \quad (62)$$

$$Q_i = \sin(\varphi_i) \quad (63)$$

The phase offset was set to  $45^\circ$  with sample rate was set to follow the sample rate of the system.

Electrical bias and electrical gain component are applied for modulation signal normalization. Electrical bias component adds a constant bias value to the input signal. Output of electrical bias can be calculated as:

$$output = input + bias \quad (64)$$

Electrical gain component gives ideal gain to the input signal. Output of electrical gain can be observed as:

$$output = input \times gain \quad (65)$$

Bias used in the simulation is 1 while gain applied in the simulation is 0.5.

Phase modulators component is implemented to modulate the user data bit with the optical signal. In the phase modulator, the electrical modulation signal imposes a phase modulation on an optical carrier. Output optical signals from phase modulator can be defined as (5) where phase deviation implemented in the

simulation was 180 degrees.

Optical couplers component is applied to coupling the optical signals. In the simulation, for combining or splitting optical signals, a cross coupler was used. The transmission matrix can be evaluated with (4). If the parameter conjugate is “False”, the relative phase shift between input port#1 and output port#2 is +90 degrees, indicating that  $p$  is positive (+1). The relative phase change between input port#1 and output port#2 equals -90 degrees when parameter conjugate is “True”, where  $p$  is negative (-1). Coupling coefficient, that is, coupling factor from port#1 to port#2 was set to 0.5. In the simulation, the additional loss, i.e., loss applied to the signal after coupling was set to 0 dB and conjugate value was set to “True”.

Optical adder component is utilized for summing the optical signals. Optical adder component adds the input optical signals from two inputs and can be formulated as:

$$output = (input\ #1) + (input\ #2) \quad (66)$$

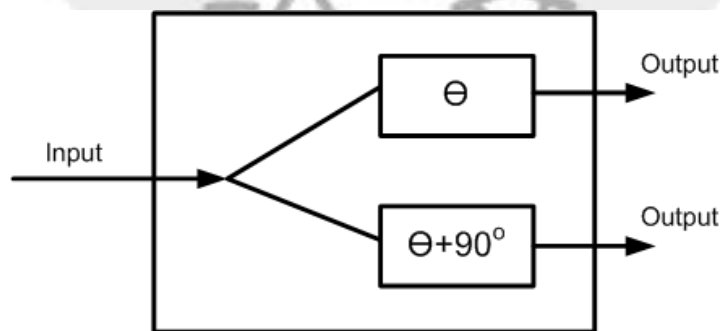


Figure 3.4 Polarization splitter structure

Polarization splitter component is used to polarize the optical signals into two polarization states. This component divides the input signal to two output ports. The first port of the polarization splitter output the optical signals with the polarization of  $\theta$ , i.e., device angle set in the parameter while the second port pass the optical signal with polarization of  $\theta + 90^\circ$ . In this simulation, device angle was set to 0 degree. Figure 3.4 depicts the polarization splitter principle.

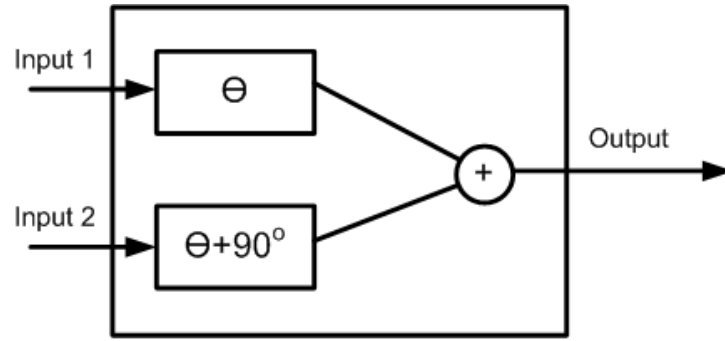


Figure 3.5 Polarization combiner structure

Polarization combiner component is implemented to combine the optical signals from different polarization states. This component combines the two input optical signals to one output port. The angle of each polarizer is defined by device angle. For the second port, an angle of  $90^\circ$  is added to the device angle. In this simulation, device angle was set to 0 degree. Figure 3.5 illustrates the polarization combiner principle.

Free-space optical channel component is utilized as the transmission medium. This component is made up of two telescopes and the free-space channel that connects them. For the modelling of line-of-sight free-space terrestrial connections, the FSO channel is used. The FSO channel's range, or the distance between the transmitter and receiver telescopes, was set between 0 and 500 m. The transmitter telescope's aperture diameter was set to 5 cm, while the receiver telescope's aperture diameter was set to 20 cm. Beam divergence was set to 2 mrad. The laser power attenuation in FSO is primarily determined by two parameters: Attenuation and Geometrical Loss. The Attenuation parameter indicates how much the laser power is attenuated in the atmosphere. The second parameter, Geometrical Loss, suffered from the distribution of the transmitted beam between the transmitter and the receiver. The link equation can be evaluated as:

$$P_R = P_T \frac{d_R^2}{(d_T + \theta R)^2} 10^{-\alpha \frac{R}{10}} \quad (67)$$

where  $d_r$  is receiver aperture diameter (m),  $d_t$  denotes transmitter aperture diameter (m),  $\theta$  is beam divergence (mrad),  $R$  denotes range (km), and  $\alpha$  is atmospheric attenuation (dB/km).

To simulate as closely as possible the real world, all attenuations, geometrical losses, and beam divergence were defined using typical industrial values in accordance with the ITU-T G.652 standard. The beam divergence and receiver aperture diameter affect the quality of the superimposed signal in the FSO channel. The advantage of a larger receiver area was its ability to minimize errors due to scintillation. The averaging effect of the localized surges and fades is achieved by using a receiver aperture that is much larger than the spatial scale of the scintillation. This improves the error rate. The total attenuation can also be decreased by reducing this effect.

Ideal optical circulator component is used to transfer the optical signal from one port to another port. This component prevents the optical signal from propagating in an unintended direction by directing it from one port to another. There is no return loss or isolation in this component, only the insertion loss exists. The insertion loss was set to 0 dB in the simulation and is the attenuation between Input#1 – Output#2, Input#2 – Output#3, and Input#3 – Output#1.

Uniform FBG component is employed to reflect and transmit the wavelength according to the signature code. The optical signals of the various users vary, which means that each user has its unique code signature detected by the series of FBGs used in the decoding process. The frequency of the uniform FBG was set according to the signature code used in the bipolar OCDMA system. The bandwidth of the uniform FBG was set to 125 GHz with maximum reflectivity of the grating was 0.99. For noise settings, noise threshold was set to -100 dB with noise dynamic of 3 dB.

Electrical subtractor is implemented to subtracts the input electrical signals. This component is applied to subtract the electrical signals from upper and lower

side of the bipolar OCDMA system. The output of electrical subtractor can be observed as:

$$output = (input \#1) - (input \#2) \quad (68)$$

Low pass Bessel filter component is used for filtering the electrical signals with the cut-off frequency of its linear phase response up to 0.75\*bit rate. This component is functioning as filter with a Bessel frequency transfer function. The original electrical signal is recovered using a Low Pass Bessel Filter. A fourth-order Bessel low pass filter is used to reject noise and interference components from the signal. Bessel filters have the following transfer function:

$$H(s) = \alpha \frac{d_0}{B_N(s)} \quad (69)$$

where  $\alpha$  is the parameter insertion loss,  $N$  is the parameter order, and

$$d_0 = \frac{(2N)!}{2^N \cdot N!} \quad (70)$$

being a normalizing constant and  $B_N(s)$  is an  $n$ th-order Bessel polynomial of the form:

$$B_N(s) = \sum_{k=0}^N d_k s^k \quad (71)$$

with

$$d_k = \frac{(2N-k)!}{2^{N-k} \cdot k! \cdot (N-k)!} \quad (72)$$

$$\text{and } s = j \left( \frac{f \cdot w_b}{f_c} \right) \quad (73)$$

where  $f_c$  is the filter cut-off frequency, defined by the parameter frequency and  $w_b$  denotes the normalized 3 dB bandwidth where  $N > 10$  can be approximated by:

$$w_b \approx \sqrt{(2N-1) \cdot \ln 2} \quad (74)$$



An electrical signal is regenerated by using the 3R Generator component. This component produces the original bit sequence as well as a modulated electrical signal for BER analysis. The bit sequence is the first output port of the 3R Generator, followed by a modulated NRZ signal and a copy of the input signal. These three signals can be connected directly to the BER Analyzer, no connections between the transmitter and the BER Analyzer are needed.

BER Analyzer component is applied to observe the performance of the system. This component displays the bit error rate of an electrical signal. BER analyser capable to estimate the BER using various algorithms, such as Gaussian and Chi-Squared, further extract various metrics from the eye diagram, such as Q-factor, eye opening, eye closure, extinction ratio, eye height, jitter, etc. Forward Error Correction (FEC) can be included in the BER. This component also can estimates the system penalties and margins. The decision instant was set to 0.5 bit period as the threshold, which is the value of the decision instant for the maximum Q-factor/minimum BER. Clock recovery was used in this component.

There are four parameters that can be observed from this component:

1. Max Q-factor: maximum value for the Q-factor in the eye time window.
2. Min BER: minimum value for the bit error rate in the eye time window.
3. Eye height: maximum value for the eye height in the eye time window.
4. Threshold: value of the threshold at the decision instant for the maximum Q-factor/minimum BER.

The error probability is calculated numerically by:

$$P_e = \frac{1}{2} \operatorname{erfc} \left( \frac{Q}{\sqrt{2}} \right) \quad (75)$$

The Q-factor is calculated with:

$$Q = \frac{|\mu_1 - \mu_0|}{\sigma_1 + \sigma_0} \quad (76)$$

where  $\mu$  is the average value and  $\sigma$  denotes the standard deviation. The eye height is calculated by:

$$E_H = (\mu_1 - 3\sigma_1) - (\mu_0 + 3\sigma_0) \quad (77)$$

The eye amplitude is calculated by:

$$E_A = \mu_1 - \mu_0 \quad (78)$$

The eye closure is calculated by:

$$E_c = \min(V_1) - \max(V_0) \quad (79)$$

where  $\min(V_1)$  is the minimum value of the amplitude for the marks and  $\max(V_0)$  is the maximum value for the amplitude of the spaces.

The eye-opening factor is calculated by:

$$E_o = \frac{(\mu_1 - \sigma_1) - (\mu_0 - \sigma_0)}{(\mu_1 - \mu_0)} \quad (80)$$

The extinction ratio is calculated by:

$$E_R = \frac{\mu_1}{\mu_0} \quad (81)$$

Optical spectrum analyser is used to examine the optical signals. This component displays optical signals in the frequency domain, including the signal intensity, group delay, phase, power spectral density, and dispersion for horizontal and vertical polarizations. Rectangle type is used as filter in the OSA. Electrical signals are showed in the time domain by the oscilloscope component. Oscilloscope can display the signal amplitude and auto-correlation, including the signal, noise, also signal with noise.

Photodetector component is utilized to convert optical signals into electrical signals. Based on the device's responsivity, a PIN photodiode component is used to transform an optical signal into an electrical current. The responsivity of the PIN photodiode was set to 1 A/W. The sample rate was 5 times of the global system sample rate. The noise applied in PIN photodiode included signal-amplified spontaneous emission (ASE) noise, ASE-ASE noise, thermal noise, and shot noise with Gaussian distribution. For the noise, dark current was set to 10 nA and thermal power density was set to 100e-024 W/Hz. APD component has the

same function with PIN photodiode. The gain of APD was set to 3 with ionization ratio was 0.9.

White light source component was utilized in the proposed scheme in order to create AWGN channel. This component generates a gaussian distributed optical white noise. This model generates noise bins or sampled signals at the output according to:

$$\begin{pmatrix} E_X(t) \\ E_Y(t) \end{pmatrix} = \begin{pmatrix} \hat{x}_X(t) + j\hat{y}_X(t) \\ \hat{x}_Y(t) + j\hat{y}_Y(t) \end{pmatrix} \sqrt{\frac{P}{4}} \quad (82)$$

For the real and imaginary parts of  $E_X$  and  $E_Y$ , a Gaussian distribution has been assumed to define the probability density function. When the power spectral density (PSD) parameter is “False”, the notation  $P$  represents the average power. If PSD is “True”,  $P$  is determined by multiplying PSD by the sample rate. In this simulation, the frequency of white light source was set to 1552 nm with power of -130 dBm.

Table 3.3 summarizes the overall simulation parameters.

Table 3.3 Simulation parameters

Parameter		Value
Global	Bit rate	10e+009 bits/s
	Sample rate	640e+009 Hz
	Number of samples	4096
	Sensitivity	-100 dBm
CW laser	Linewidth	10 MHz
	Power	0 dBm
	Azimuth	45 deg
	Noise threshold	-100 dB
	Frequency	1546...1568 nm ( $\lambda_1 \dots \lambda_{12}$ )

Table 3.3 Simulation parameters (continue)

Parameter		Value
Electrical bias	Bias	1
Electrical gain	Gain	0.5
Phase modulator	Phase deviation	180 degree
Free-space optics channel	Range	50-500 m
	Transmitter aperture diameter	5 cm
	Receiver aperture diameter	20 cm
	Beam divergence	2 mrad
Uniform fiber-bragg grating	Bandwidth	125 GHz
	Reflectivity	0.99
	Noise threshold	-100 dB
	Noise dynamic	3 dB
Avalanche photodetector	Gain	3
	Responsivity	1 A/W
	Ionization ratio	0.9
	Dark current	10 nA
	Sample rate	5*(sample rate)
	Thermal power density	100e-024 W/Hz

### 3.2.2 Noises and Channel Model of Bipolar OCDMA System

Second simulation was conducted to testify the proposed Bi-OCDMA in different channel condition. By adjusting various factors, the simulations were performed in order to evaluate the transmission performance of the system. The simulation was demonstrated by using architecture showed in Figure 3.3 with two simultaneous users. A real scenario was evaluated by using OptiSystem, which

permits to consider all practical effects of attenuation, dark current, shot noise, receiver thermal noise, and weather condition which may include rain, haze, fog, etc. Some noises were implemented in the simulation in order to perform the closely-real environment of the free-space optical system. The noise includes ASE noise, thermal noise, and shot noise with gaussian distribution where total noises effect can be observed with:

$$\sigma_{total}^2 = \sigma_{th}^2 + \sigma_{shot-S}^2 + \sigma_{shot-ASE}^2 + \sigma_{S-ASE}^2 + \sigma_{ASE-ASE}^2 \quad (83)$$

Each noise induced in the simulation can be verify as follows:

- Thermal noise:

$$\sigma_{th}^2 = \frac{4.k_B.T}{R_L}.ENB \quad (84)$$

- Shot-Signal Noise:

$$\sigma_{shot-S}^2 = 2B_e.(rM^2P_s + i_d) \quad (85)$$

- Shot-ASE Noise:

$$\sigma_{shot-ASE}^2 = M^2F.2B_e.qrP_{ASE} \quad (86)$$

- Signal-ASE Noise:

$$\sigma_{S-ASE}^2 = 4B_e.r^2.M^2.PSD_{ASE}P_s \quad (87)$$

- ASE-ASE Beat Noise:

$$\sigma_{ASE-ASE}^2 = r^2.M^2.PSD_{ASE}^2 \quad (88)$$

where  $T$  is the absolute temperature of the device,  $R_L$  denotes the receiver load resistance,  $k_B$  is the Boltzmann constant,  $ENB$  is the receiver equivalent electrical noise bandwidth,  $B_e$  denotes the equivalent noise bandwidth of the photodetector,  $r$  is the PIN responsivity,  $M$  is the gain,  $F$  denotes the excess noise factor,  $P_s$  is the signal power,  $i_d$  denotes the device dark current,  $q$  is the electron charge value,  $P_{ASE}$  is the optical noise power, and  $PSD_{ASE}$  denotes the power spectral density of the optical noise field (spontaneous emission).

Two channel conditions were implemented in the second simulation, namely, AWGN channel and turbulence-induced fading channel. AWGN channel was created by added white light source with power of -130 dBm to the optical signals before transmit through the FSO. Turbulence conditions can be defined by using a variety of models, including Log-Normal, negative exponential, K-distribution, and Gamma–Gamma, with Gamma–Gamma being the most dominant in weak to strong turbulence. Further, Gamma-Gamma distribution was applied to model the turbulence-induced fading channel in this simulation. In all turbulence strength regimes, the Gamma-Gamma distribution model can be used to analyze the scintillation of atmospheric turbulence. The Gamma-Gamma includes both small-scale and large-scale atmospheric fluctuations. Performance of the system was observed for the optimum performance in the form of minimum Log of BER and maximum Q-Factor.

In the Gamma-Gamma fading model, the probability of intensity  $I$  can be calculated by:

$$P(I) = \frac{2(\alpha\beta)^{(\alpha+\beta)/2}}{\Gamma(\alpha)\Gamma(\beta)} I^{(\alpha+\beta)/2-1} K_{\alpha-\beta}(2\sqrt{\alpha\beta I}) \quad (89)$$

where  $\Gamma(\dots)$  is the Gamma function,  $K_{\alpha-\beta}(\dots)$  is the modified Bessel function of the second kind,  $\frac{1}{\alpha}$  and  $\frac{1}{\beta}$  are the variances of the small- and large-scale eddies and can be evaluated with:

$$\alpha = \exp\left[\frac{0.49\sigma_R^2}{(1 + 1.11\sigma_R^{12/5})^{5/6}}\right] - 1 \quad (90)$$

$$\beta = \exp\left[\frac{0.51\sigma_R^2}{(1 + 0.69\sigma_R^{12/5})^{5/6}}\right] - 1 \quad (91)$$

where  $\sigma_R^2$  denotes the Rytov variance and is calculated from:

$$\sigma_R^2 = 1.23C_n^2 k^{7/6} z^{11/6} \quad (92)$$

where  $C_n^2$  is the parameter index refraction structure with value ranges from  $10^{-13} \text{ m}^{-2/3}$  to  $10^{-17} \text{ m}^{-2/3}$ ,  $k$  denotes the optical wavenumber and  $z$  is the parameter range. In the simulation,  $C_n^2$  was set to  $10^{-17} \text{ m}^{-2/3}$  for strong turbulence,  $10^{-15} \text{ m}^{-2/3}$  for medium turbulence, and  $10^{-17} \text{ m}^{-2/3}$  for weak turbulence

Table 3.4 International visibility code [53]

Weather Conditions	Precipitation	Visibility (m)	Attenuation (dB/km)
Light fog	Storm	770	18.3
Very light fog	Strong rain	1,900	6.9
Light mist	Average rain	2,800	4.6
Very light mist	Light rain	5,900	2
Clean air	Drizzle	18,100	0.6

Further simulation was conducted in the AWGN channel for different weather condition based on standard of propagation data required for the design of terrestrial free-space optical links from International Telecommunication Union Radiocommunication Sector (ITU-R) P.1817 [53]. The attenuation in different weather conditions is showed in Table 3.4.

Table 3.5 Signature code for two users

Code	Signature Code
MD	$\begin{bmatrix} 1 & 0 & 0 & 0 & 0 & 0 & 0 & 1 \\ 0 & 1 & 0 & 0 & 0 & 0 & 1 & 0 \end{bmatrix}$
MQC	$\begin{bmatrix} 1 & 0 & 0 & 0 & 1 & 0 & 0 & 1 & 0 & 0 & 0 & 1 \\ 0 & 1 & 0 & 0 & 0 & 1 & 0 & 0 & 1 & 0 & 0 & 1 \end{bmatrix}$
Modified M-Sequence	$\begin{bmatrix} 1 & 0 & 1 & 1 & 1 & 0 & 0 & 0 \\ 1 & 1 & 1 & 0 & 0 & 1 & 0 & 0 \end{bmatrix}$
Walsh-Hadamard	$\begin{bmatrix} 1 & 0 & 1 & 0 & 1 & 0 & 1 & 0 \\ 1 & 1 & 0 & 0 & 1 & 1 & 0 & 0 \end{bmatrix}$

Four well-known SAC-OCDMA codes, i.e., MD code, MQC code, modified M-sequence code, and Walsh-Hadamard code, were applied in this simulation. These four codes satisfy the correlation properties of (45) and (46), revealed the

compatibility to be implemented in the proposed Bi-OCDMA structure. The signature code used in this simulation is showed in the Table 3.5.

國立虎尾科技大學



National Formosa University



# Chapter 4 Simulation Results and Analysis of The Proposed Bipolar OCDMA

The fourth chapter presents the simulation results along with the analysis. The simulation conducted in two parts. First simulation aims to verify the feasibility of the proposed system to generate bipolar codes for OCDMA in the FSO network by utilizing phase modulator to achieved the polarization coding. The simulation utilized modified M-sequence as the signature code for single-user scheme. First simulation also tested the mismatch decoder scenario to prove the MAI elimination property of the proposed bipolar OCDMA system. Second simulation purpose is to observe the performance of the proposed bipolar OCDMA system. The performance measurements were simulated in two FSO channel conditions, first in the AWGN channel and further in the AWGN and turbulence-induced fading channel for different weather conditions. The comparison between several different SAC codes were also revealed in this section. The performances were inspected in terms of minimum log of BER and maximum Q-factor.

## 4.1 Feasibility of Bipolar OCDMA System with Phase Modulator Scheme for Single-User

To prove the feasibility of the proposed bipolar OCDMA system, first simulation was conducted in single-user scheme. The analysis was observed both for user data bit of “0” and “1”. The simulation was demonstrated by using structure showed in Figure 3.1 and 3.2. The first simulation was conducted with normal atmospheric condition, i.e., weak turbulence and drizzle weather condition.

First, user data bit of “0” was transmitted over the bipolar OCDMA system. The signature code implemented in this simulation is modified M-sequence for user#1. Figure 4.1 presents the binary output from bit sequence generator when

bit “0” is sent. In OptiSystem, arbitrary units (a.u.) is used with 1:1 relation toward the volts or current.

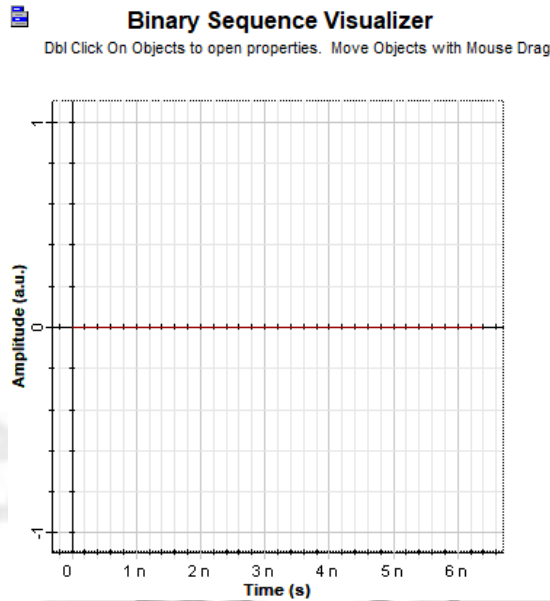


Figure 4.1 Output from bit sequence generator when bit “0” was transmitted

Figure 4.2 depicts the spectra produced by CW laser array, both the upper and lower side for user#1. Figure 4.2(a) illustrates the spectra from upper CW laser array,  $\lambda_1, \lambda_3, \lambda_4, \lambda_5$  were measured with light intensities of 0 dBm. Figure 4.2(b) shows the spectra from upper CW laser array,  $\lambda_2, \lambda_6, \lambda_7, \lambda_8$  were measured with light intensities of 0 dBm.

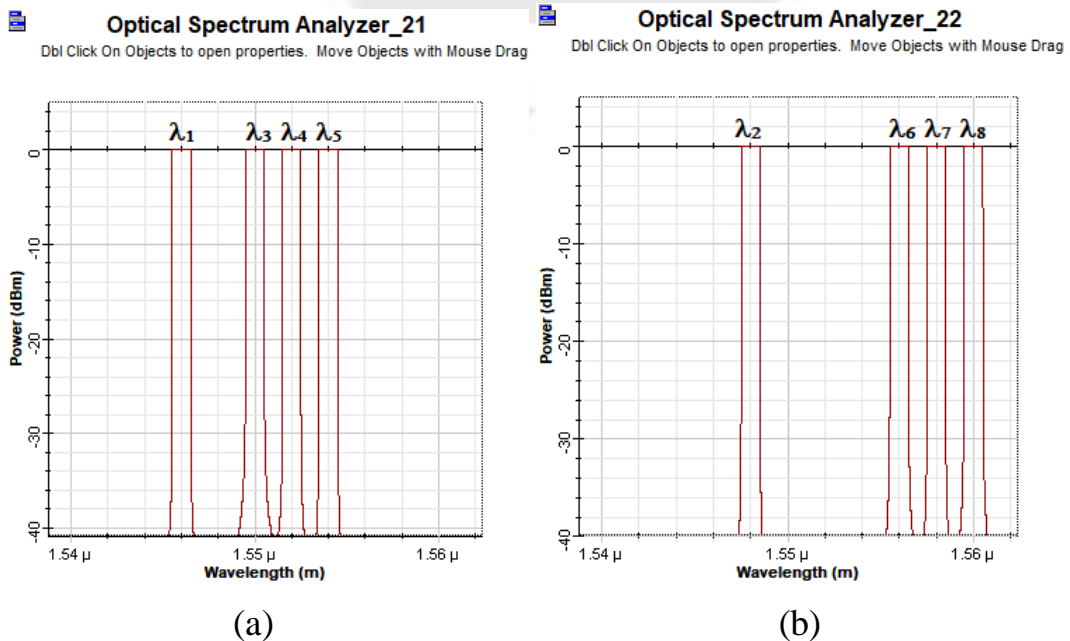


Figure 4.2 CW laser array spectra (a) Upper CW laser array, (b) Lower CW laser

array

Figure 4.3 demonstrates the electrical signals from in-phase (I) port of PSK pulse generator when bit “0” was transmitted. Figure 4.3(a) indicate the electrical signals produced after passing through the upper PSK pulse generator, the amplitude was 1 volt. Figure 4.3(b) presents the electrical signals from the lower PSK pulse generator, the amplitude measured was -1 volt.

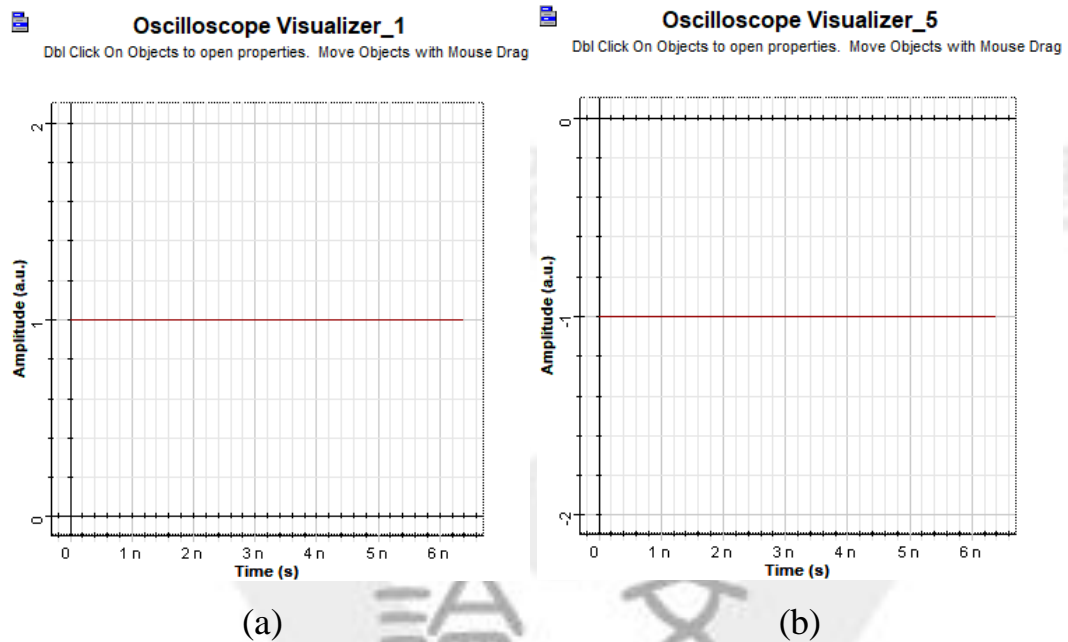


Figure 4.3 Output from PSK pulse generator when bit “0” was transmitted (a) Upper PSK pulse generator, (b) Lower PSK pulse generator

Next process aims to normalized the output from PSK pulse generator by using electrical bias and electrical gain component. Figure 4.4 illustrates the electrical signals from electrical bias when bit “0” was sent. Figure 4.4(a) shows the electrical signals after passing through the upper electrical bias, the amplitude observed was 2 volt. Figure 4.4(b) depicts the electrical signals from the lower electrical bias, the amplitude was 0.

Further, Figure 4.5 shows the electrical signals from electrical gain when bit “0” was sent. Figure 4.5(a) demonstrates the electrical signals after passing through the upper electrical gain, the amplitude was 1 volt. Figure 4.5(b) indicates the electrical signals from the lower electrical gain, the amplitude was 0. Thus,

the pulse has been normalized to 0 and 1.

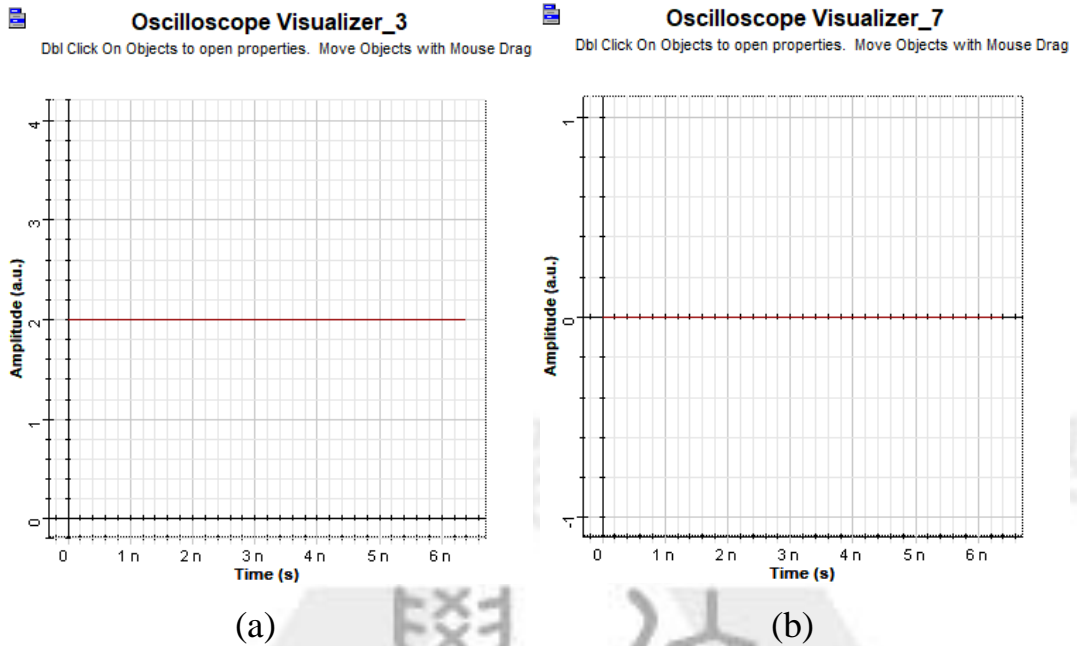


Figure 4.4 Output from electrical bias when bit “0” was transmitted (a) Upper electrical bias, (b) Lower electrical bias

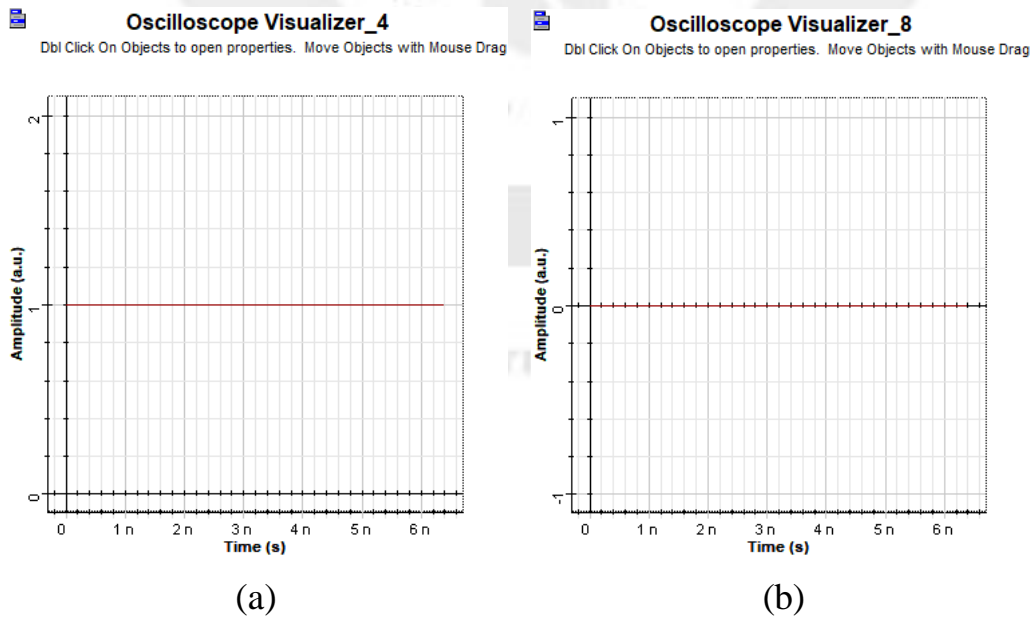


Figure 4.5 Output from electrical gain when bit “0” was transmitted (a) Upper electrical gain, (b) Lower electrical gain

Figure 4.6 shows the optical signals after modulated with phase modulator if user data bit of “0” was sent. Figure 4.6(a) indicates the modulated optical signals from upper phase modulator,  $\lambda_1$ ,  $\lambda_3$ ,  $\lambda_4$ ,  $\lambda_5$  were measured, the light intensities

were -3 dBm. Figure 4.6(b) demonstrates the modulated optical signals from lower phase modulator,  $\lambda_2, \lambda_6, \lambda_7, \lambda_8$  were measured with light intensities of -3 dBm. These results corresponded to (5).

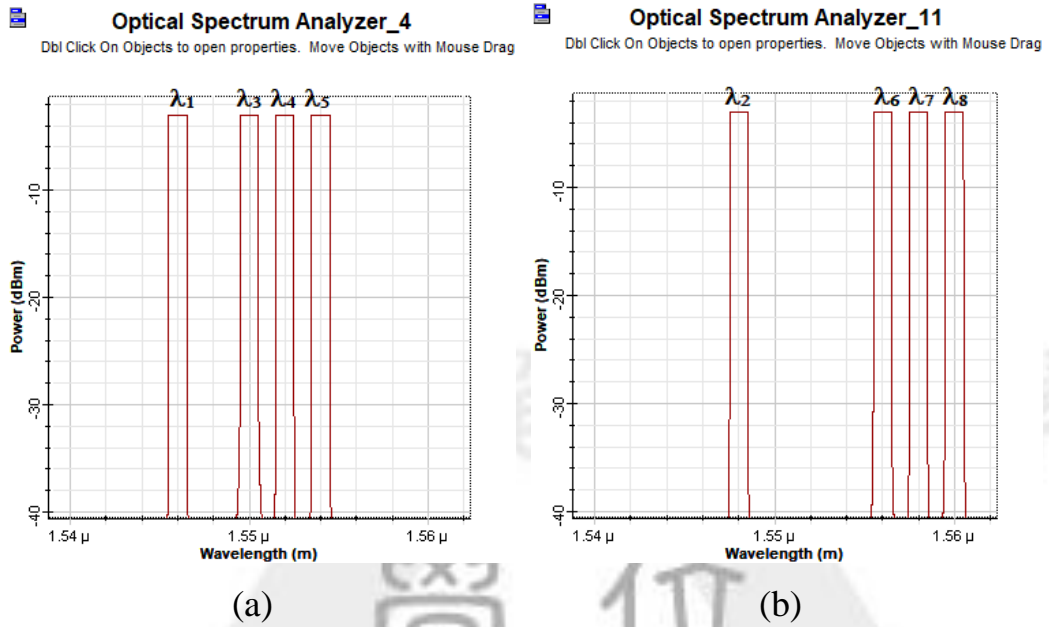


Figure 4.6 Spectra measured after modulated with phase modulator when bit “0” was transmitted (a). Upper phase modulator, (b) Lower phase modulator

Figure 4.7 reveals the optical signals after coupling with the upper optical coupler#2 when bit “0” was transmitted.

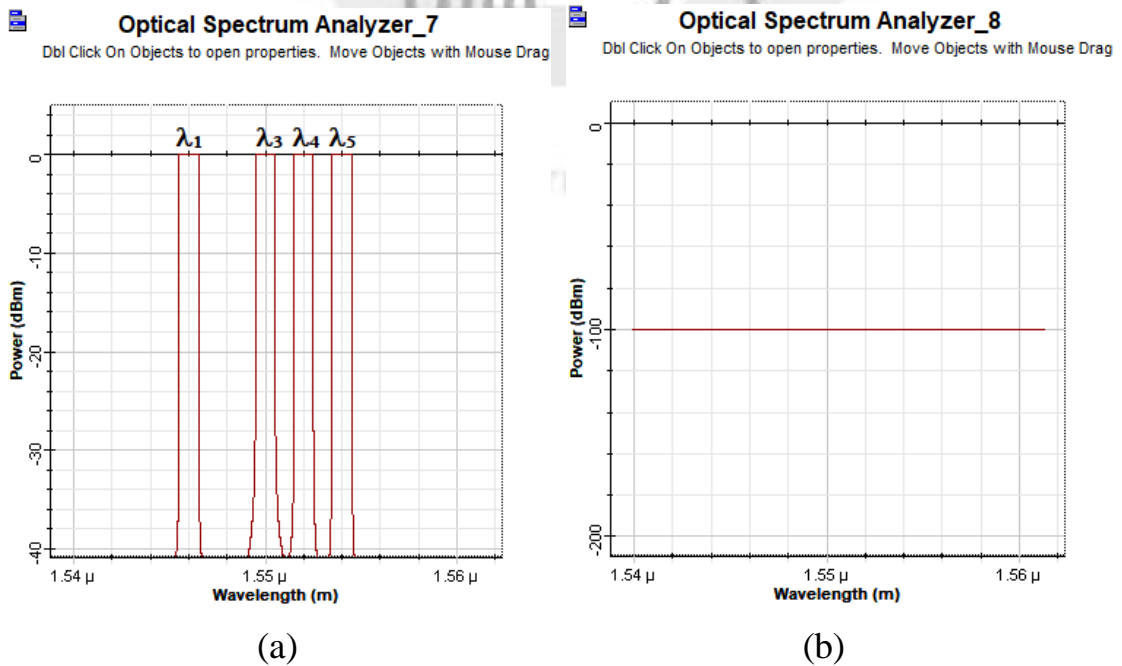


Figure 4.7 Spectra observed after coupling with upper optical coupler#2 when

bit “0” was transmitted (a) Port#1, (b) Port#2

Figure 4.7(a) presents the optical signals from port#1 of upper coupler#2,  $\lambda_1, \lambda_3, \lambda_4, \lambda_5$  were measured and the light intensities measured were 0 dBm. Figure 4.7(b) depicts the optical signals from port#2 of upper coupler#2, no spectra was measured. These results verified (4), spectra only measured on port#1.

Figure 4.8 depicts the optical signals after coupling with the lower optical coupler#2 when bit “0” was sent. Figure 4.8(a) demonstrates the optical signals from port#1 of lower coupler#2, no spectra was measured. Figure 4.8(b) illustrates the optical signals from port#2 of lower coupler#2,  $\lambda_2, \lambda_6, \lambda_7, \lambda_8$  were measured, the light intensities measured were 0 dBm. These results proved (4), spectra only measured on port#2.

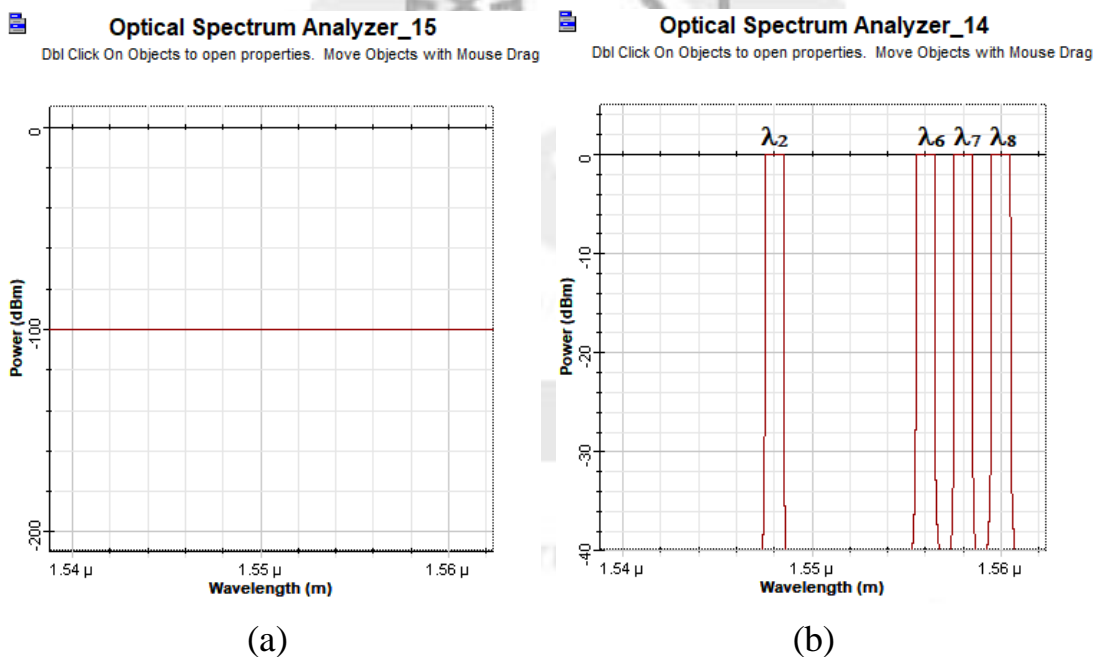


Figure 4.8 Spectra after coupling with lower optical coupler#2 when bit “0” was transmitted (a) Port#1, (b) Port#2

Figure 4.9 illustrates the measured spectra when bit “0” was transmitted after passing through the polarization splitter. Figure 4.9(a) demonstrates the measured spectra at the upper side,  $\lambda_1, \lambda_3, \lambda_4, \lambda_5$  were measured at horizontal polarization, the light intensities were -3 dBm. Figure 4.9(b) presents the measured spectra at the upper side; no spectra were measured at vertical polarization. Figure 4.9(c)

depicts the measured spectra at the lower side, no spectra were measured at horizontal polarization. Figure 4.9(d) indicates the measured spectra at the lower side,  $\lambda_2, \lambda_6, \lambda_7, \lambda_8$  were measured for vertical polarization with light intensities of -3 dBm.

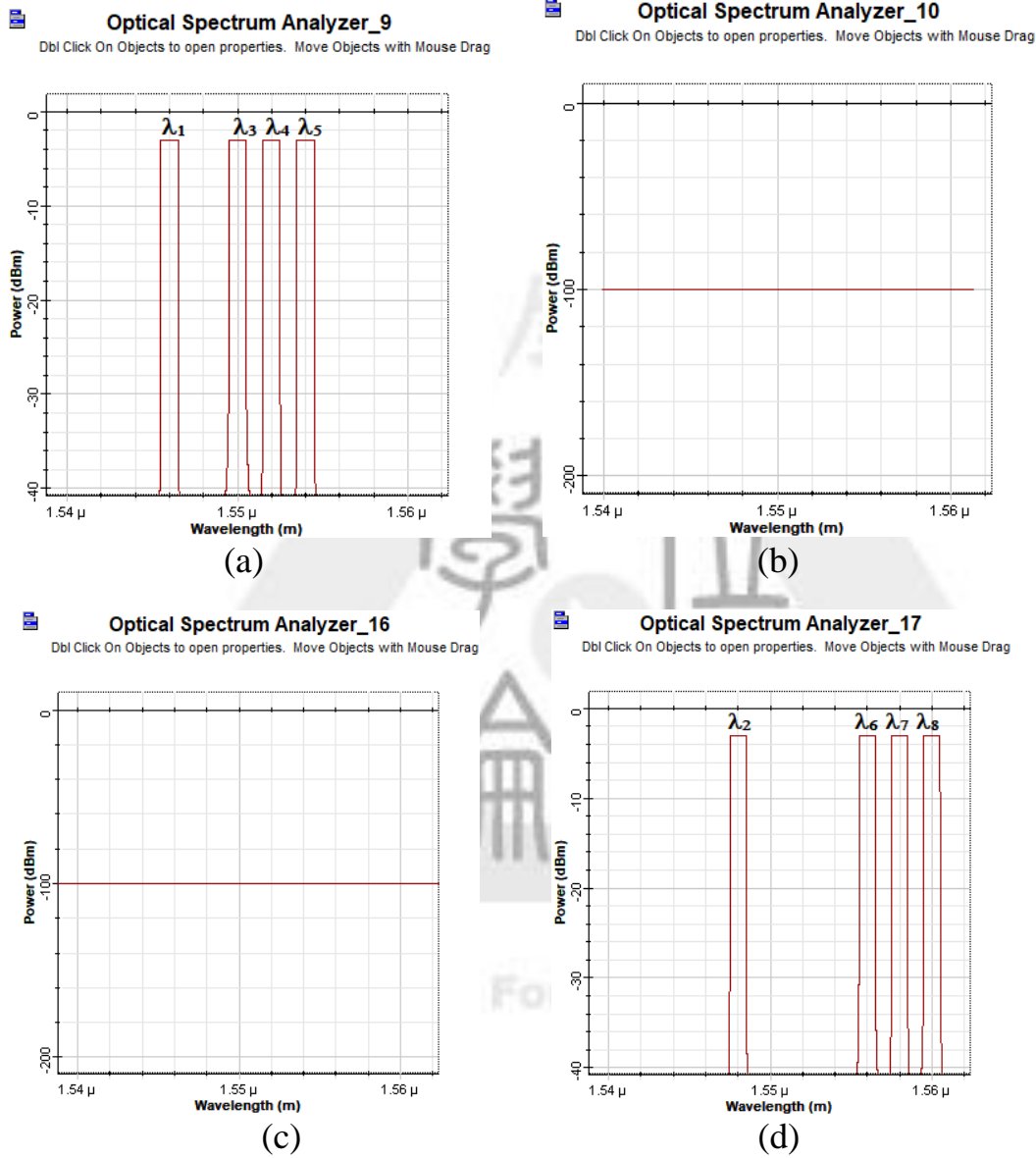


Figure 4.9 Encoded spectra after polarization splitting when bit “0” was transmitted (a) Horizontal polarization at upper side, (b) Vertical polarization at upper side, (c) Horizontal polarization at lower side, (d) Vertical polarization at lower side

Figure 4.10 presents the measured spectra after combined with polarization combiner when bit “0” was transmitted,  $\lambda_1, \lambda_2, \lambda_3, \lambda_4, \lambda_5, \lambda_6, \lambda_7, \lambda_8$  were measured

with the light intensities of -3 dBm.

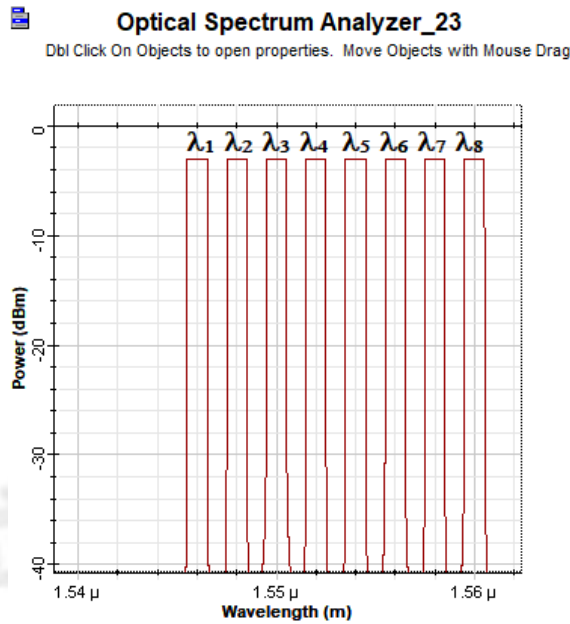


Figure 4.10 Spectra after combined with polarization combiner when bit “0” was transmitted

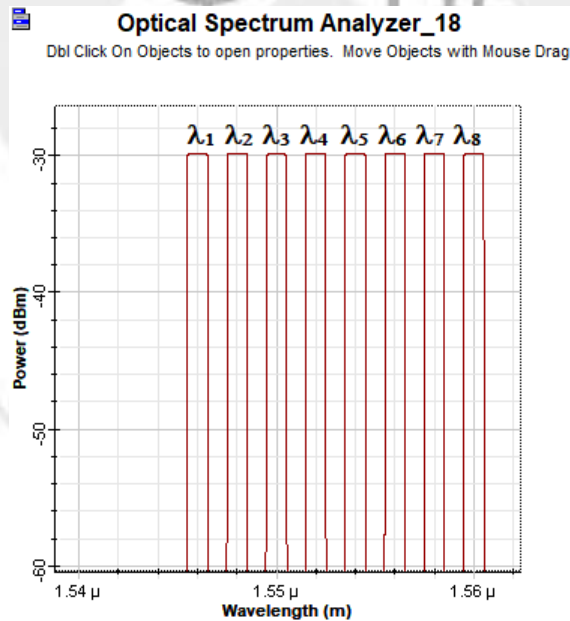


Figure 4.11 Spectra after passing through free-space optics channel when bit “0” was transmitted

Figure 4.11 presents the measured spectra when bit “0” was transmitted after passing through the FSO channel,  $\lambda_1, \lambda_2, \lambda_3, \lambda_4, \lambda_5, \lambda_6, \lambda_7, \lambda_8$  were measured with the light intensities were -30 dBm. With the parameter of FSO channel defined in



Table 3.3, the power observed was attenuated by about -27 dBm after transmission through free-space channel.

Figure 4.12 reveals the measured spectra after polarization splitting. Figure 4.12(a) shows the encoded spectra for the horizontal polarization,  $\lambda_1, \lambda_3, \lambda_4, \lambda_5$  were measured with light intensities of -30 dBm. Figure 4.12(b) illustrates the encoded spectra for the vertical polarization,  $\lambda_2, \lambda_6, \lambda_7, \lambda_8$  were measured, the light intensities were -30 dBm.

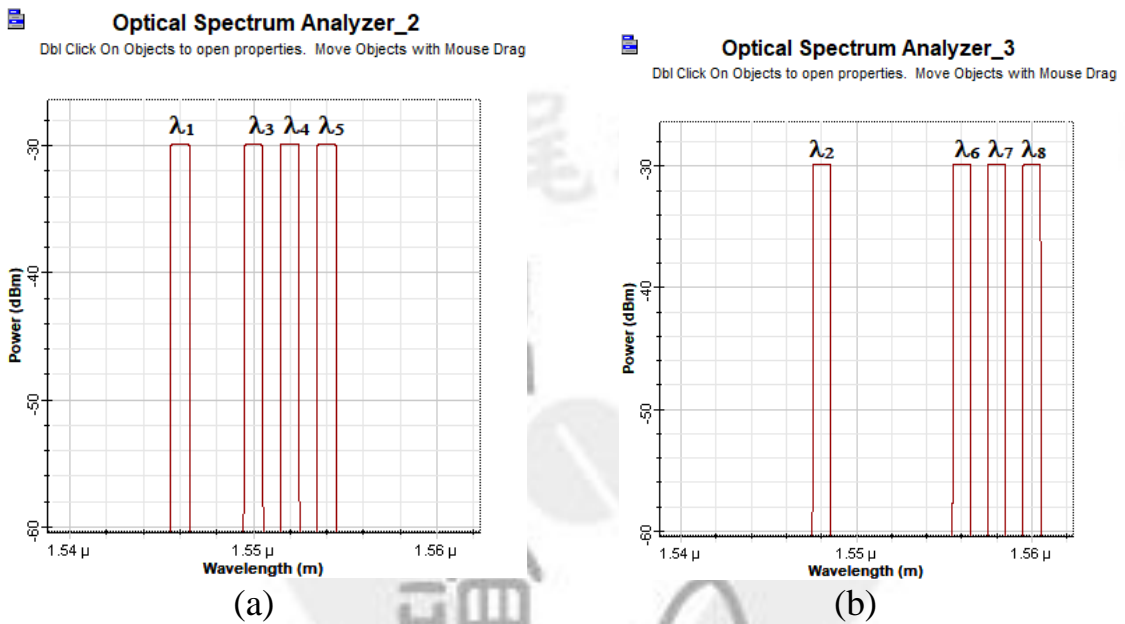


Figure 4.12 Output spectra after polarization splitting when bit “0” was transmitted (a) Horizontal polarization, (b) Vertical polarization

Figure 4.13 depicts the measured spectra before the optical signals passed to the upper and lower photodetector when data bit “0” was sent. Wavelength of  $\lambda_1, \lambda_3, \lambda_4, \lambda_5$  with horizontal polarization were reflected by first series of FBG to the lower branch while  $\lambda_2, \lambda_6, \lambda_7, \lambda_8$  were reflected by second series of FBG to the lower branch. Figure 4.13(a) presents the measured spectra for horizontal polarization at the upper branch, no spectra was measured. Figure 4.13(b) shows the measured spectra for vertical polarization at the upper branch, no spectra was measured. Figure 4.13(c) displays the total measured spectra at the upper branch, no spectra was measured. Figure 4.13(d) demonstrates the measured spectra for horizontal polarization at the lower branch,  $\lambda_2, \lambda_6, \lambda_7, \lambda_8$  were measured with light

intensities of -30 dBm. Figure 4.13(e) reveals the measured spectra for vertical polarization at the lower branch,  $\lambda_1, \lambda_3, \lambda_4, \lambda_5$  were measured with light intensities of -30 dBm. Figure 4.13(f) presents the total measured spectra at the lower branch,  $\lambda_1, \lambda_2, \lambda_3, \lambda_4, \lambda_5, \lambda_6, \lambda_7, \lambda_8$  were measured, the light intensities were -30 dBm.

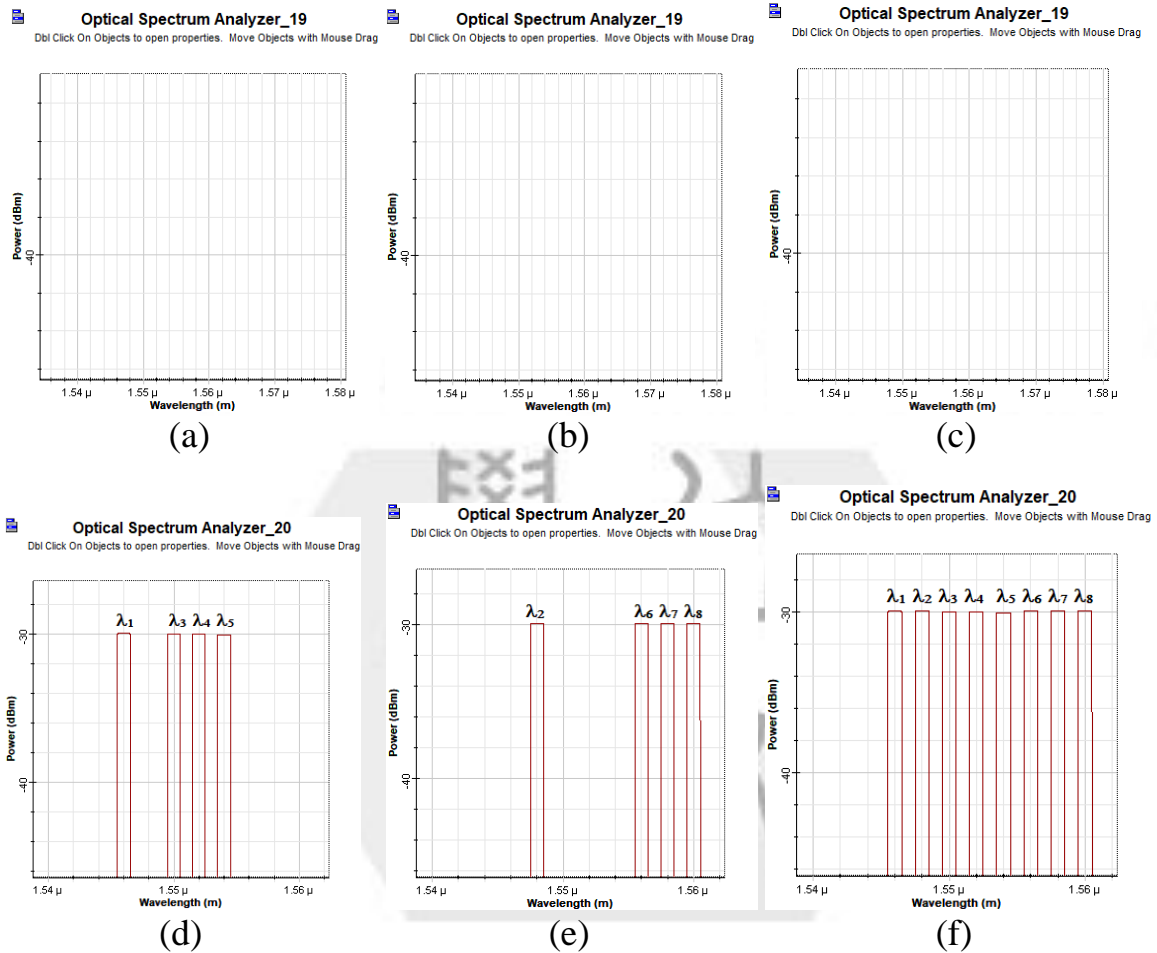


Figure 4.13 Output spectra before photodetection when bit “0” was transmitted  
 (a) Horizontal polarization at upper branch, (b) Vertical polarization at upper branch, (c) Total signals at upper branch, (d) Horizontal polarization at lower branch, (e) Vertical polarization at lower branch, (f) Total signals at lower branch

From Figure 4.13(c) and 4.13(f), no spectral chip at the upper branch and eight spectral chips were appeared at the lower branch, the electrical subtraction between upper and lower branch resulted in negative signal amplitude, represents the negative parts “-1” of the bipolar scheme.

Figure 4.14 illustrates the output electrical signals (blue color) and noise

signals (green color) after balanced photodetection process. Figure 4.14 (a) presents the separated electrical signals and noise signals while Figure 4.14(b) demonstrates the combined electrical signals and noise signals. From the figure can be seen that the electrical signals amplitude is negative, represents the negative parts “-1” of the bipolar scheme.

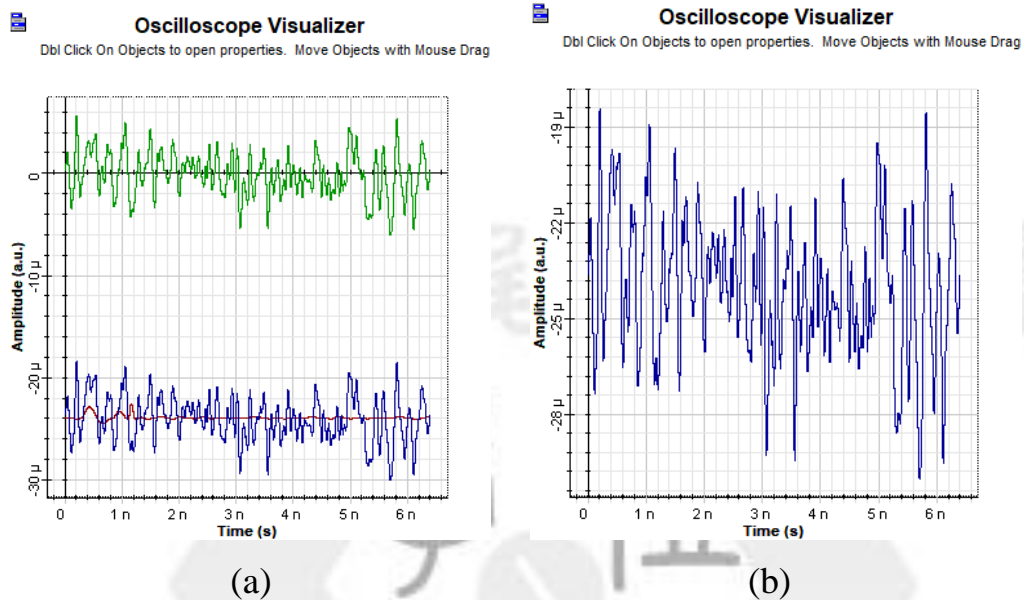


Figure 4.14 Output electrical signals of the proposed Bi-OCDMA system when bit “0” was transmitted (a) Separated electrical and noise signals, (b) Combined electrical and noise signals

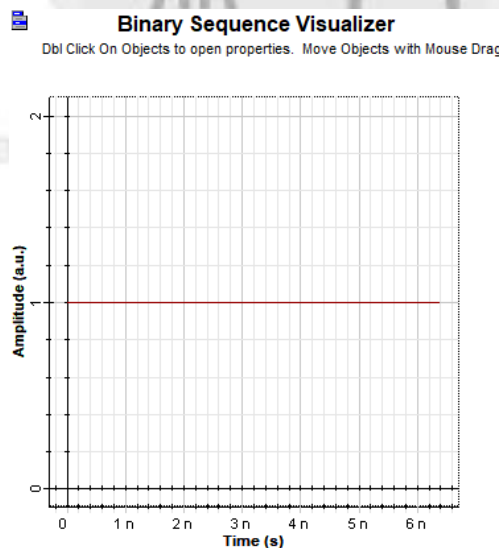


Figure 4.15 Output from bit sequence generator when bit “1” was transmitted

Another case was analyzed when bit “1” was transmitted through the

proposed bipolar OCDMA system. Figure 4.15 displays the binary output from bit sequence generator when bit “1” was transmitted.

Figure 4.16 displays the electrical signals from in-phase (I) port of PSK pulse generator when bit “1” was sent. Figure 4.16(a) demonstrates the electrical signals produced after passing through the upper PSK pulse generator, the amplitude was -1 volt. Figure 4.16(b) reveals the electrical signals from the lower PSK pulse generator, the amplitude measured was 1 volt.

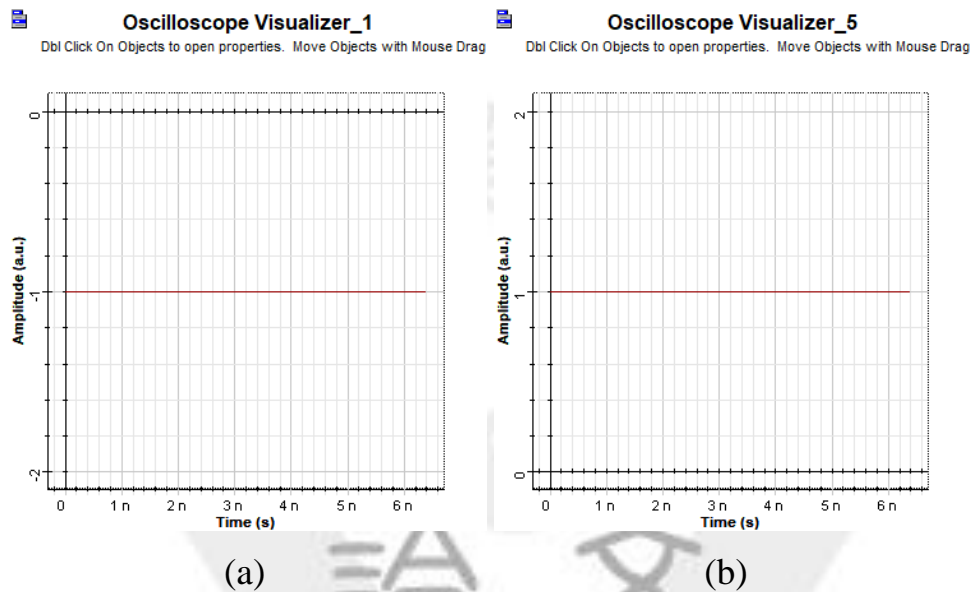


Figure 4.16 Output from PSK pulse generator when bit “1” was transmitted (a) Upper PSK pulse generator, (b) Lower PSK pulse generator

Since output from PSK pulse generator in terms of “-1” and “1”, electrical bias and electrical gain was further implemented to normalized the pulse. Figure 4.17 depicts the electrical signals from electrical bias when bit “1” was sent. Figure 4.17(a) presents the electrical signals after passing through the upper electrical bias, the amplitude was 0. Figure 4.17(b) displays the electrical signals from the lower electrical bias where the amplitude was 2 volt.

Figure 4.18 demonstrates the electrical signals from electrical gain when bit “1” was sent. Figure 4.18(a) shows the electrical signals after passing through the upper electrical gain, the amplitude was 0. Figure 4.18(b) displays the electrical signals from the lower electrical gain, the amplitude was 1 volt. Accordingly, the

pulse already normalized into 0 and 1 amplitude.

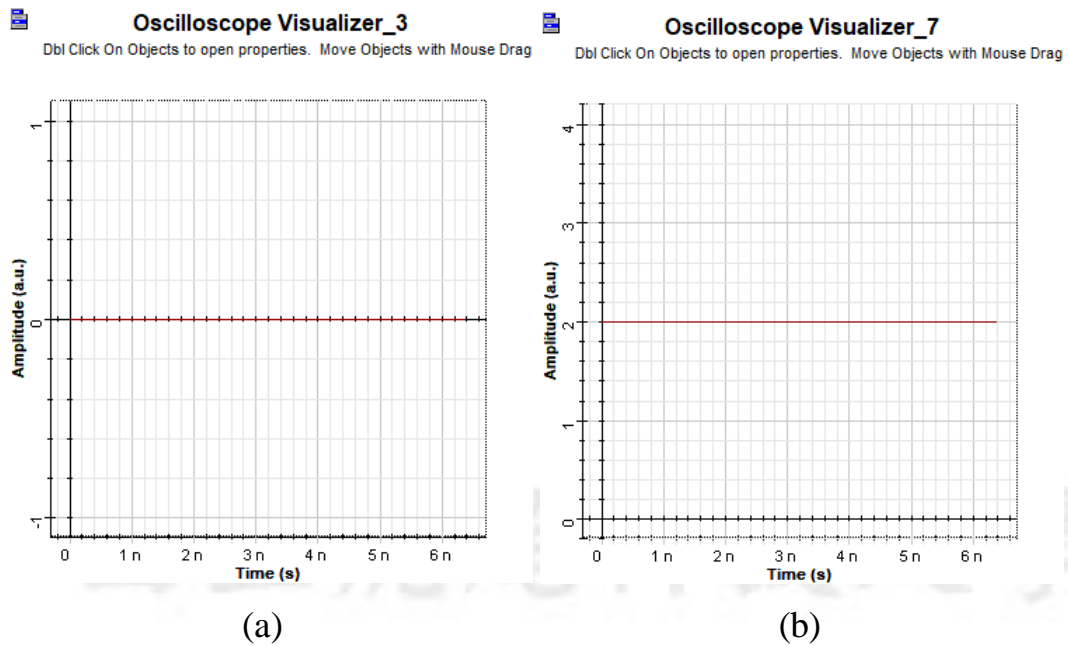


Figure 4.17 Output from electrical bias when bit “1” was transmitted (a) Upper electrical bias, (b) Lower electrical bias

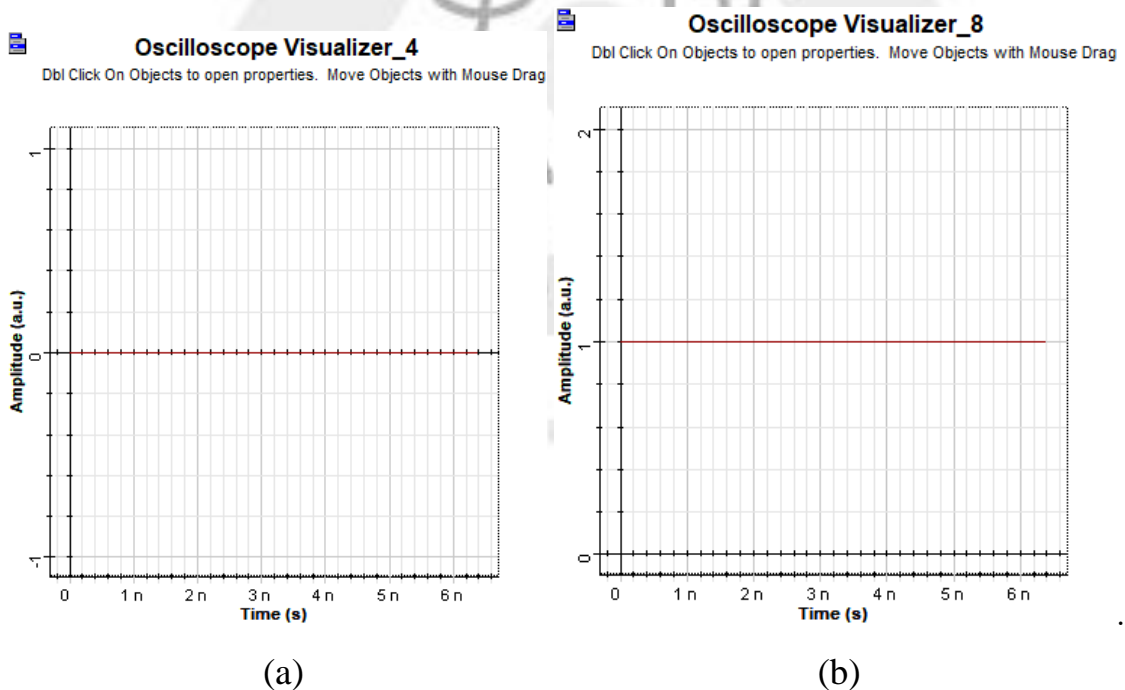


Figure 4.18 Output from electrical gain when bit “1” was transmitted (a) Upper electrical gain, (b) Lower electrical gain

Figure 4.19 displays the optical signals after modulated with phase modulator if user data bit of “1” was transmitted. Figure 4.19(a) shows the

modulated optical signals from upper phase modulator,  $\lambda_1, \lambda_3, \lambda_4, \lambda_5$  were measured, the light intensities were -3 dBm. Figure 4.19(b) illustrates the modulated optical signals from lower phase modulator,  $\lambda_2, \lambda_6, \lambda_7, \lambda_8$  were measured, the light intensities were -3 dBm. These results confirmed with (5).

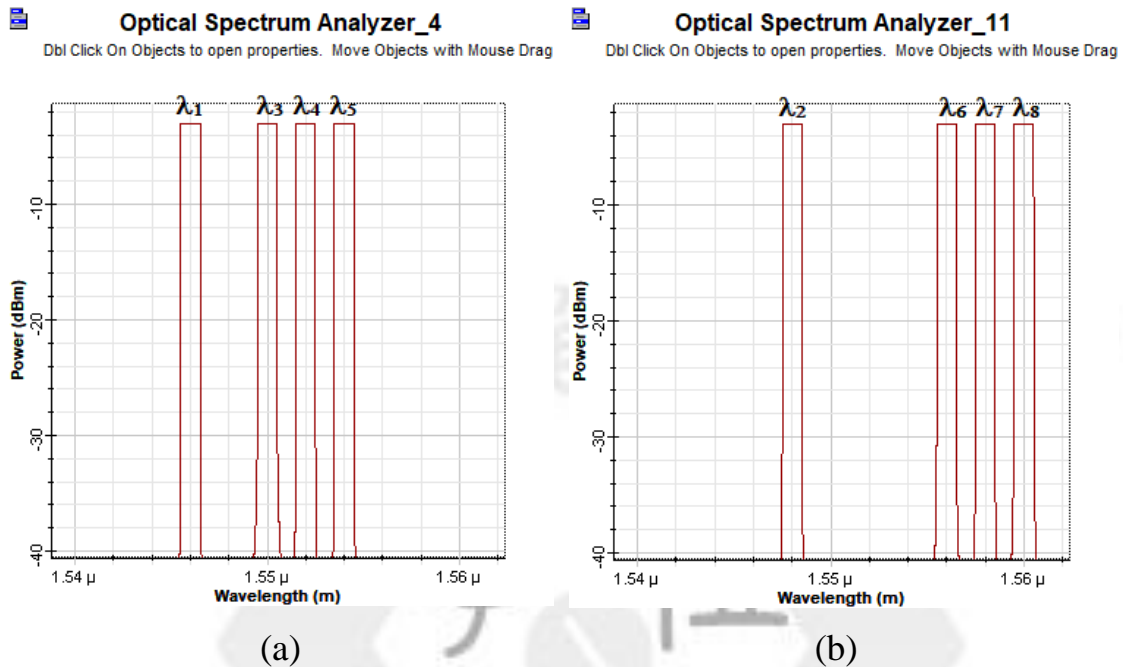
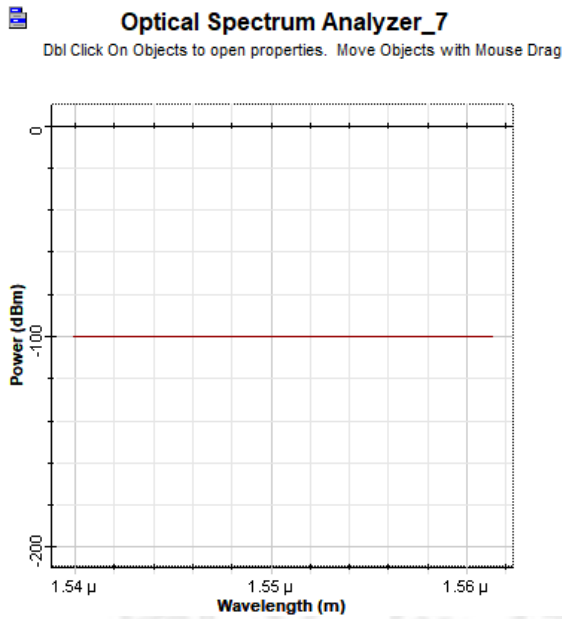


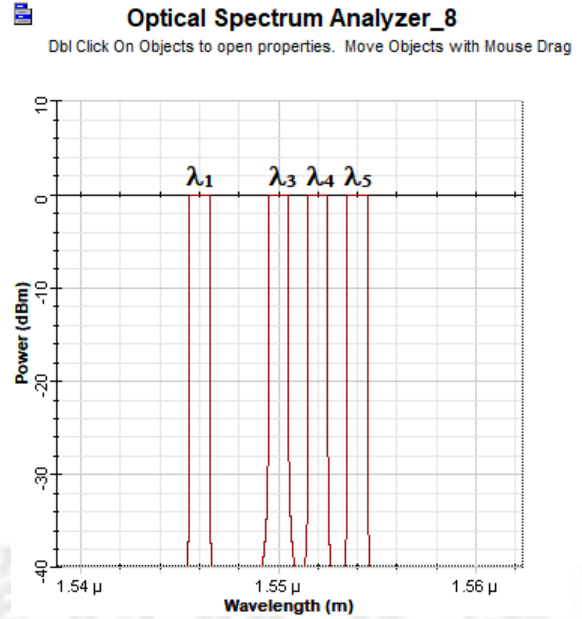
Figure 4.19 Spectra measured after modulated with phase modulator when bit “1” was transmitted (a) Upper phase modulator, (b) Lower phase modulator

Figure 4.20 shows the optical signals after coupling with the upper optical coupler#2 when bit “1” was transmitted. Figure 4.20(a) displays the optical signals from port#1 of upper coupler#2, no spectra was measured. Figure 4.20(b) reveals the optical signals from port#2 of upper coupler#2,  $\lambda_1, \lambda_3, \lambda_4, \lambda_5$  were measured with the light intensities of 0 dBm. These results proved (4), spectra only appeared at port#2 of optical coupler#2.

Figure 4.21 presents the optical signals after coupling with the lower optical coupler#2 when bit “1” was transmitted. Figure 4.21(a) depicts the optical signals from port#1 of lower coupler#2,  $\lambda_2, \lambda_6, \lambda_7, \lambda_8$  were measured, the light intensities were 0 dBm. Figure 4.21(b) shows the optical signals from port#2 of lower coupler#2, no spectra was measured. This result is matched with (4), spectra only measured at port#1 of optical coupler#2.

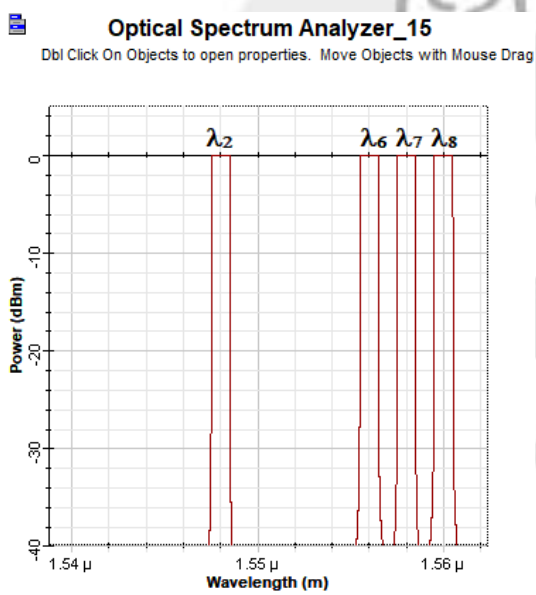


(a)

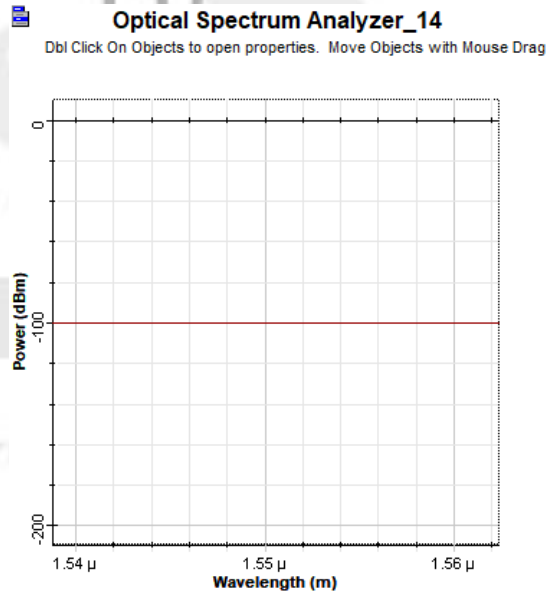


(b)

Figure 4.20 Spectra after coupling with upper optical coupler#2 when bit “1” was transmitted (a) Port#1, (b) Port#2



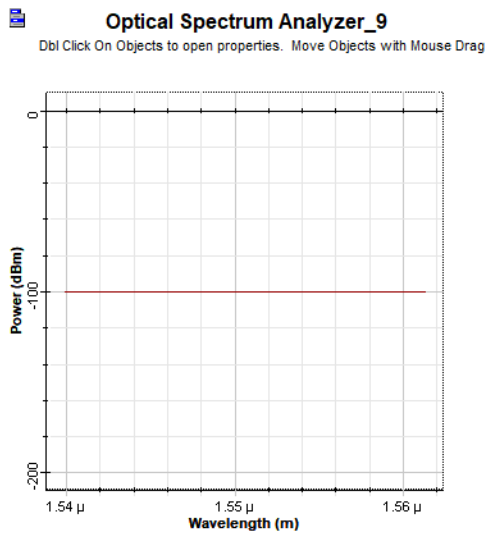
(a)



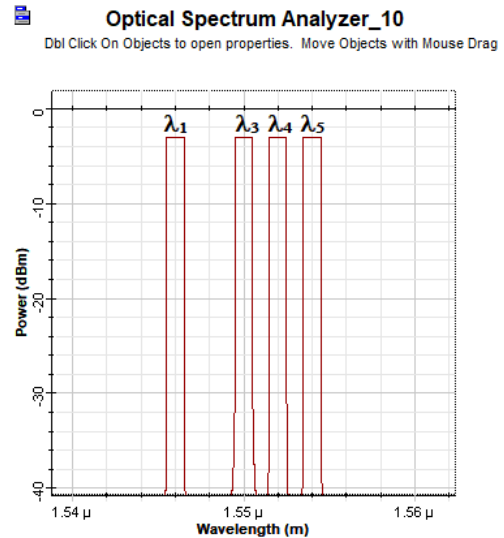
(b)

Figure 4.21 Spectra after coupling with lower optical coupler#2 when bit “1” was transmitted (a) Port#1, (b) Port#2

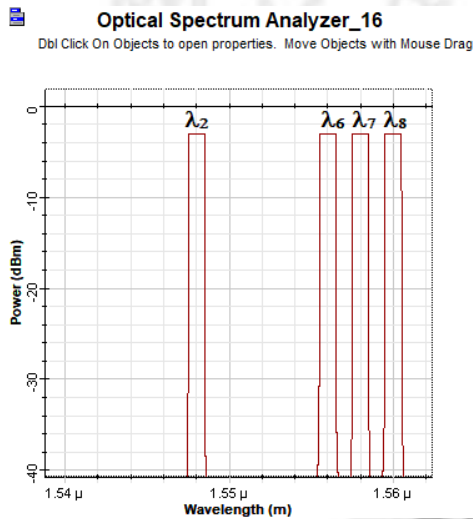
Figure 4.22 demonstrates the measured spectra when bit “1” was transmitted after passing over the polarization splitter.



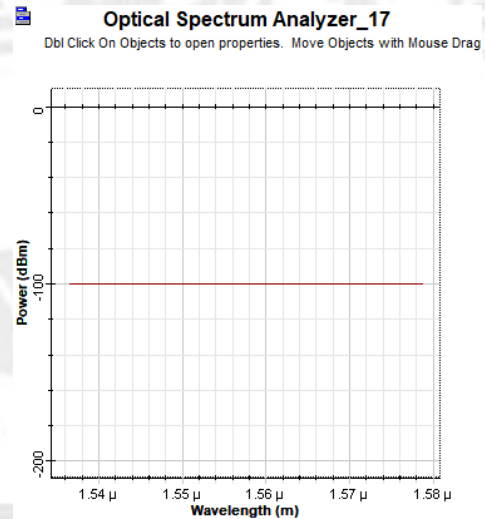
(a)



(b)



(c)



(d)

Figure 4.22 Encoded spectra after polarization splitting when bit “1” was transmitted (a) Horizontal polarization at upper side, (b) Vertical polarization at upper side, (c) Horizontal polarization at lower side, (d) Vertical polarization at lower side

Figure 4.22(a) reveals the measured spectra at the upper side, no spectra were measured at horizontal polarization. Figure 4.22(b) displays the measured spectra at the upper side,  $\lambda_1, \lambda_3, \lambda_4, \lambda_5$  were measured at vertical polarization, the light intensities were -3 dBm. Figure 4.22(c) illustrates the measured spectra at the lower side,  $\lambda_2, \lambda_6, \lambda_7, \lambda_8$  were measured at horizontal polarization with light intensities of -3 dBm. Figure 4.22(d) presents the measured spectra at the lower



side; no spectra were measured for vertical polarization.

Figure 4.23 presents the measured spectra after combined with polarization combiner when bit “1” was transmitted,  $\lambda_1, \lambda_2, \lambda_3, \lambda_4, \lambda_5, \lambda_6, \lambda_7, \lambda_8$  were measured with the light intensities of -3 dBm.

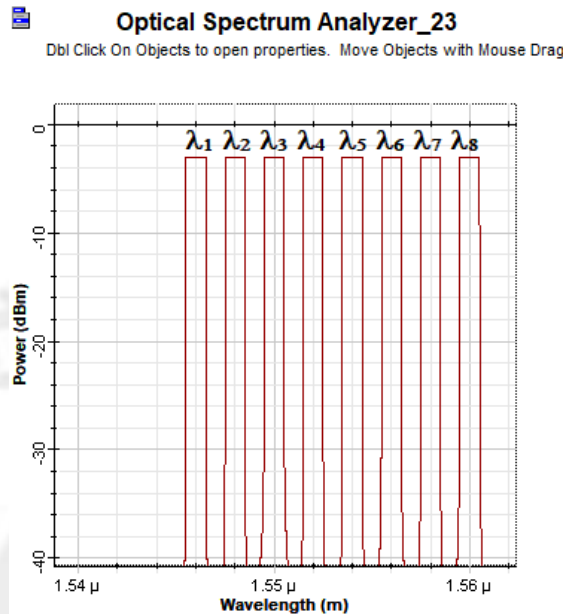


Figure 4.23 Spectra after combined with polarization combiner when bit “1” was transmitted

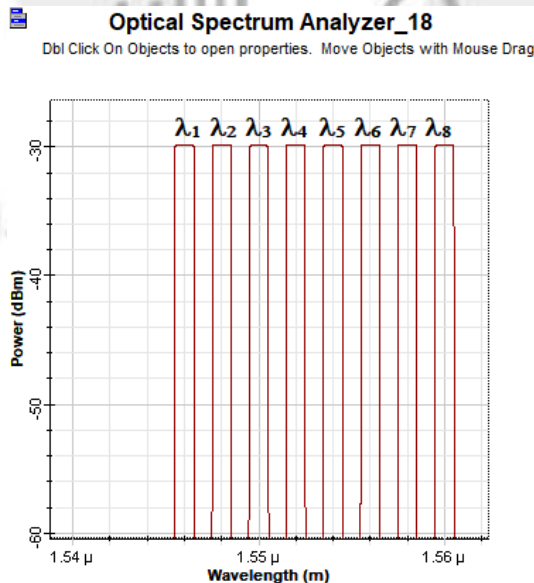


Figure 4.24 Spectra after passing through free-space optics channel when bit “1” was transmitted

Figure 4.24 reveals the measured spectra when bit “1” was transmitted after passing through the FSO channel,  $\lambda_1, \lambda_2, \lambda_3, \lambda_4, \lambda_5, \lambda_6, \lambda_7, \lambda_8$  were measured with the light intensities were -30 dBm. The power was deteriorated by about -27 dBm after transmission through free-space channel with parameter showed in Table 3.3.

Figure 4.25 depicts the measured spectra after polarization splitting when bit “1” was transmitted. Figure 4.25(a) indicates the encoded spectra for the horizontal polarization,  $\lambda_2, \lambda_6, \lambda_7, \lambda_8$  were measured with light intensities of -30 dBm. Figure 4.25(b) displays the encoded spectra for the vertical polarization,  $\lambda_1, \lambda_3, \lambda_4, \lambda_5$  were measured, the light intensities were -30 dBm.

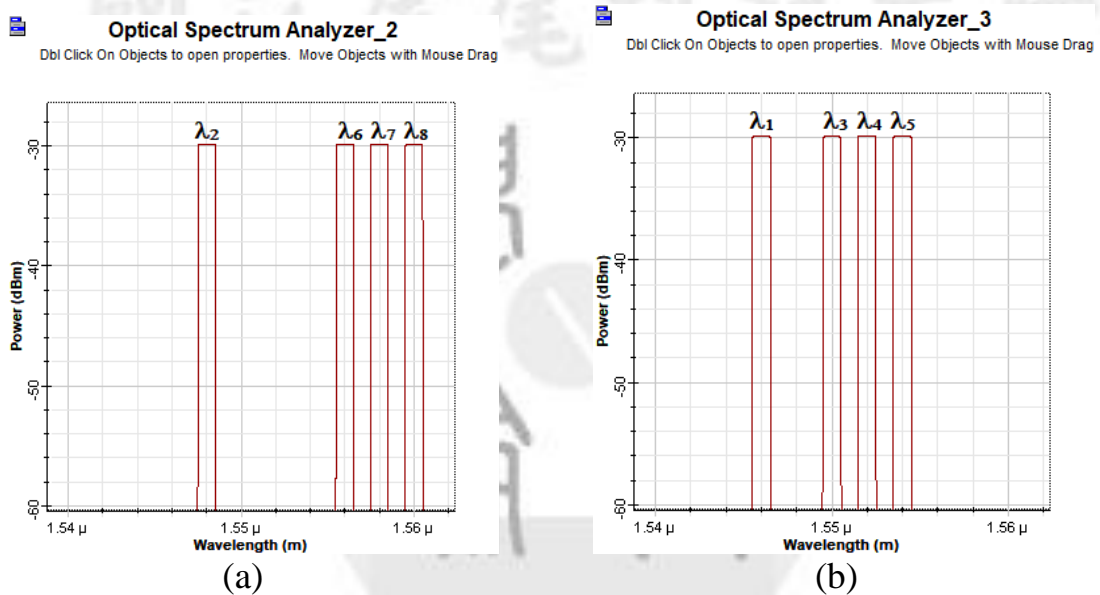


Figure 4.25 Output spectra after polarization splitting when bit “1” was transmitted (a) Horizontal polarization, (b) Vertical polarization

Figure 4.26 illustrates the measured spectra before the optical signals entered the upper and lower photodetector when data bit “1” was sent. Wavelength of  $\lambda_2, \lambda_6, \lambda_7, \lambda_8$  with horizontal polarization were transmitted by first series of FBG to the upper branch while  $\lambda_1, \lambda_3, \lambda_4, \lambda_5$  with vertical polarization were transmitted by second series of FBG to the upper branch. Figure 4.26(a) presents the measured spectra for horizontal polarization at the upper branch,  $\lambda_2, \lambda_6, \lambda_7, \lambda_8$  were measured with light intensities of -30 dBm. Figure 4.26(b) shows the measured spectra for vertical polarization at the upper branch,  $\lambda_1, \lambda_3, \lambda_4, \lambda_5$  were measured,

the light intensities were -30 dBm. Figure 4.26(c) depicts the total measured spectra at the upper branch,  $\lambda_1, \lambda_2, \lambda_3, \lambda_4, \lambda_5, \lambda_6, \lambda_7, \lambda_8$  were measured with the light intensities of -30 dBm. Figure 4.26(d) indicates the measured spectra for horizontal polarization at the lower branch, no spectra was measured. Figure 4.26(e) displays the measured spectra for vertical polarization at the lower branch, no spectra was measured. Figure 4.26(f) presents the total measured spectra at the lower branch; no spectra was measured.

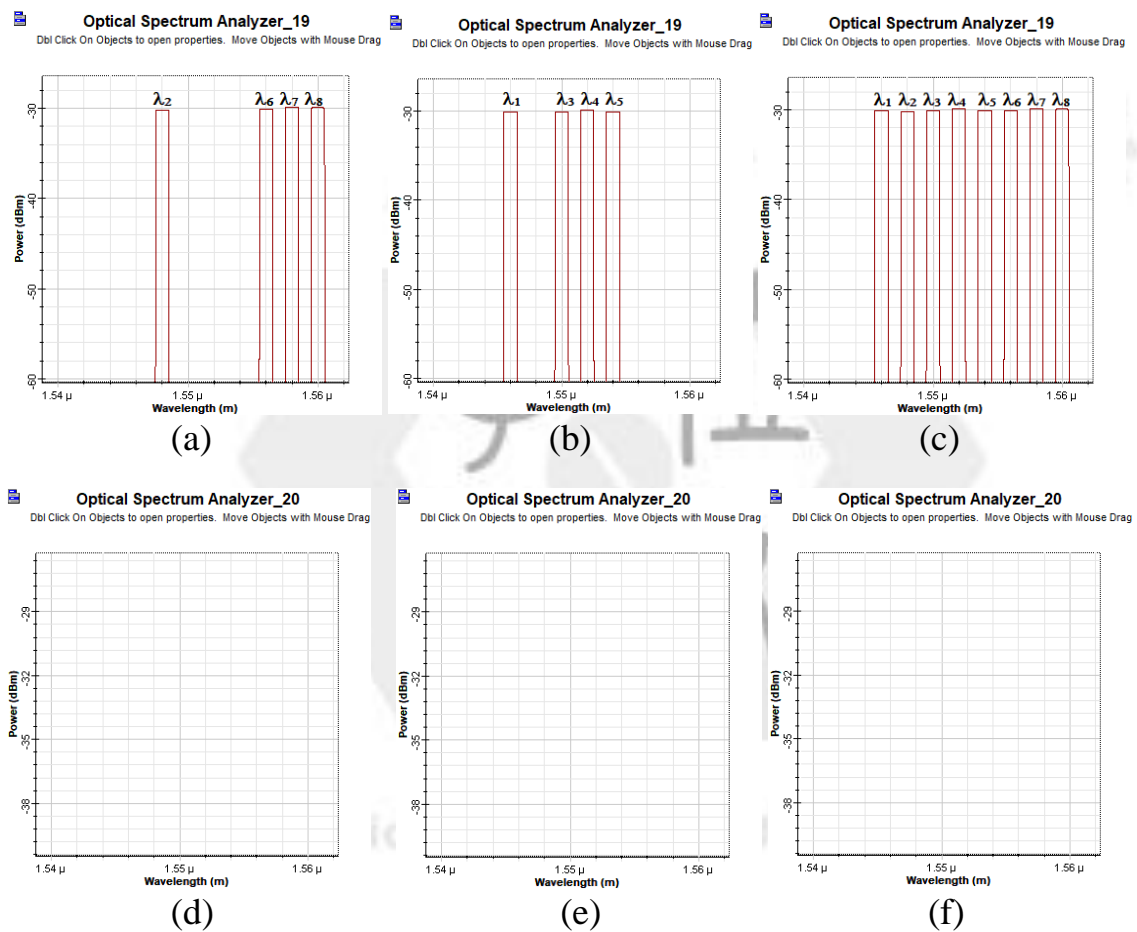


Figure 4.26 Output spectra before photodetection when bit “1” was transmitted  
 (a) Horizontal polarization at upper branch, (b) Vertical polarization at upper branch, (c) Total signals at upper branch, (d) Horizontal polarization at lower branch, (e) Vertical polarization at lower branch, (f) Total signals at lower branch

From Figure 4.26(c) and 4.26(f), eight spectral chips were appeared at the upper branch and no spectral chip at the lower branch, the electrical subtraction

between upper and lower branch resulted in positive signal amplitude, represents the positive parts “+1” of the bipolar scheme.

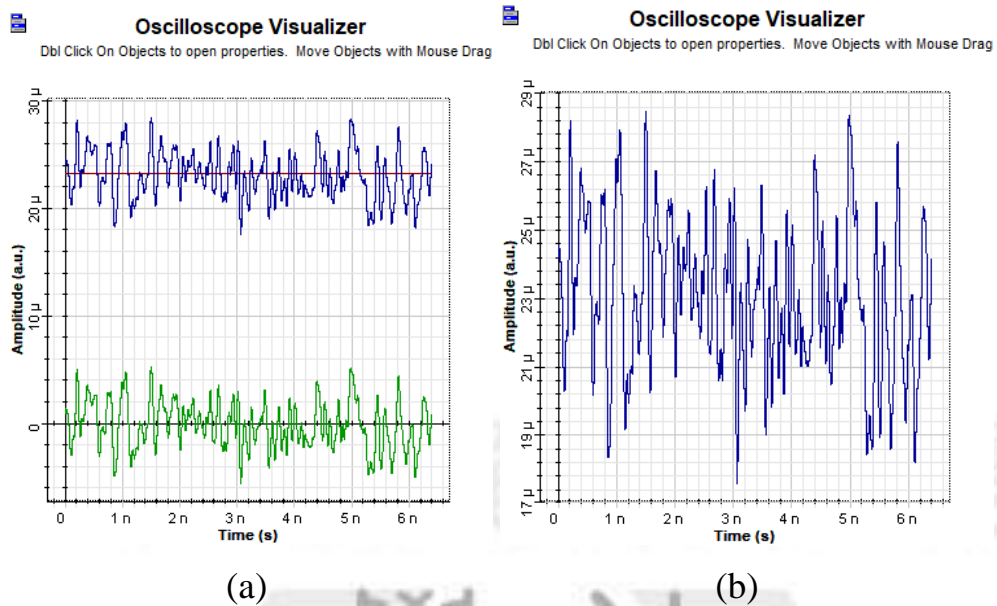


Figure 4.27 Output electrical signals of the proposed Bi-OCDMA system when bit “1” was transmitted (a) Separated electrical and noise signals, (b) Combined electrical and noise signals

Figure 4.27 depicts the output electrical signals (blue color) and noise signals (green color) after balanced photodetection process. Figure 4.27(a) displays the separated electrical signals and noise signals while Figure 4.27(b) illustrates the combined electrical signals and noise signals. From the figure can be seen that the electrical signals amplitude is positive, represents the positive parts “+1” of the bipolar scheme.

The first simulation results proved the feasibility of bipolar scheme from the proposed bi-OCDMA with phase modulator model. Further verification was done by transmitting series of user data bit with alternating bit between “0” and “1”. Figure 4.28 illustrates the user’s information generated from PRBS which generate binary bit sequence between bit “0” and “1”.

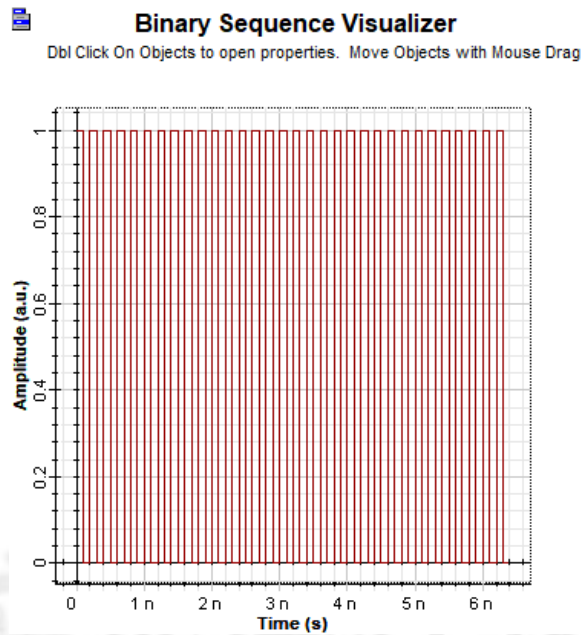


Figure 4.28 Binary sequence generated from PRBS

After transmitted through the proposed Bi-OCDMA system, Figure 4.29 depicts the result in bipolar signals at decoder-end with signals amplitude between  $-20\mu\text{V}$ . and  $20\mu\text{V}$ .

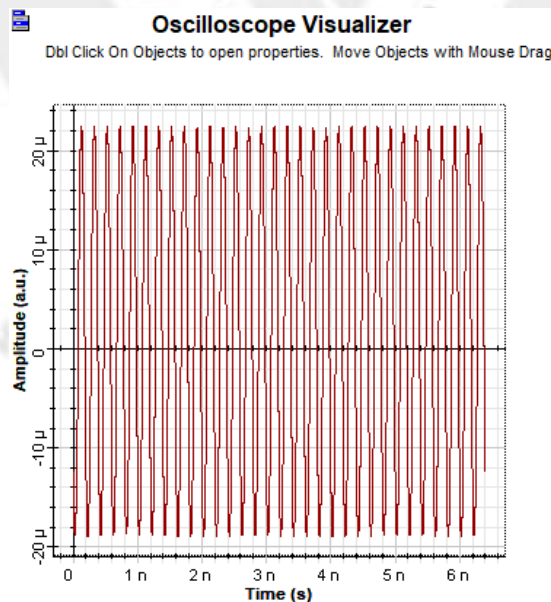


Figure 4.29 Output signals from the proposed bi-OCDMA system without noise

Figure 4.30 displays the bipolar signals resulted at decoder-end with the effect of noise where the noise parameter is defined in Table 3.3. The noise impact on signals amplitude fluctuation and further will affect the system performance.

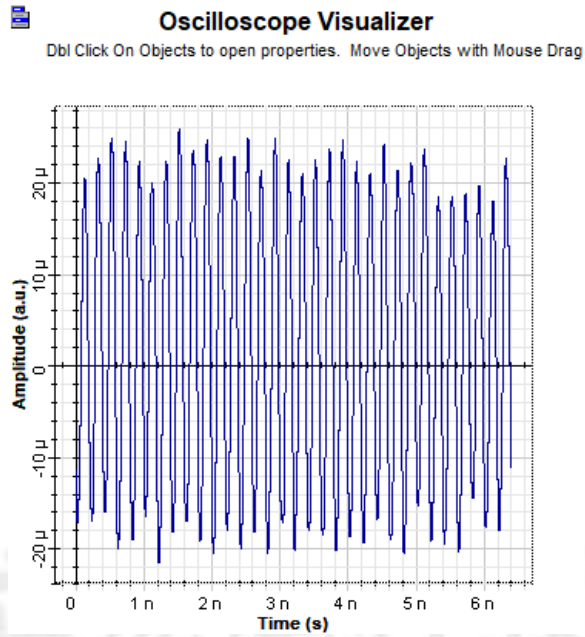


Figure 4.30 Output signals from the proposed bi-OCDMA system with the effects of noise

The proposed bipolar OCDMA system maintain the SAC feature of MAI elimination. In order to verify the MAI elimination property, further simulation was conducted with case of mismatch decoder.

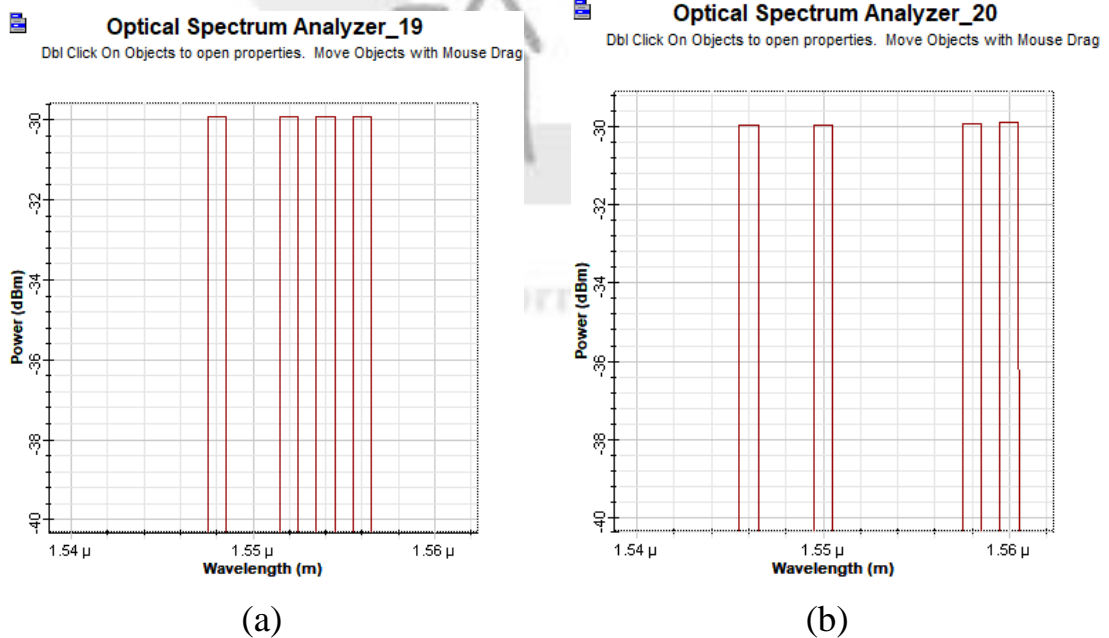


Figure 4.31 Output spectra before photodetection for mismatch decoder when bit “0” was transmitted (a) Total signals at upper branch, (b) Total signals at lower branch

The MAI cancellation feature was evaluated with the mismatch scenario. The encoder was using user#1 signature code from modified M-sequence, i.e. 10111000 while the decoder was implemented with user#2 signature code from modified M-sequence, i.e. 01110010, demonstrated the mismatch decoder. Figure 4.31 indicates the output spectra before photodetection when bit “0” was sent. Figure 4.31(a) reveals the measured spectra at upper branch,  $\lambda_2, \lambda_4, \lambda_5, \lambda_6$  were measured with light intensities of -30 dBm. Figure 4.31(b) displays the measured spectra at lower branch,  $\lambda_1, \lambda_3, \lambda_7, \lambda_8$  were measured, the light intensities were -30 dBm.

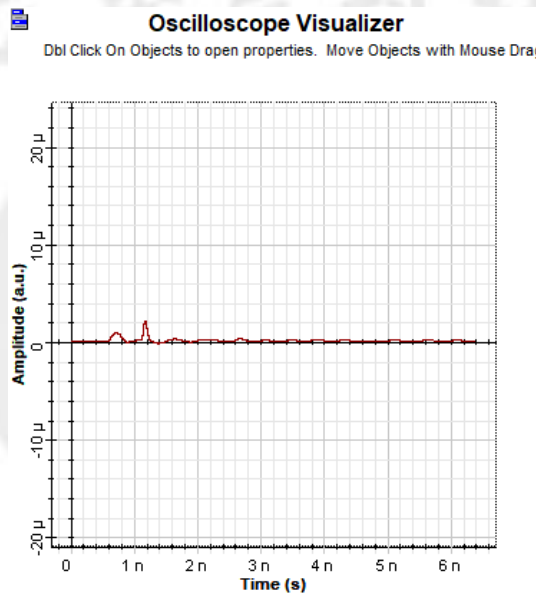


Figure 4.32 Output electrical signals of the proposed Bi-OCDMA system for mismatch decoder when bit “0” was transmitted

From Figure 4.31(a) and 4.31(b), four spectral chips were appeared at the upper branch and four spectral chips were also measured at the lower branch, the electrical subtraction between upper and lower branch resulted in zero signal amplitude, proved the MAI elimination of the bipolar scheme. Figure 4.32 illustrates the output after balanced detection in case of mismatch decoder when bit “0” was sent. A small acceptable signal was measured, resulted from imperfect filter of FBG decoder.

## 4.2 Performance of Bipolar OCDMA System with Phase Modulator Scheme for Multi-User in Different Channel Condition

Second simulation was conducted to testify the proposed Bi-OCDMA in different channel condition. The simulation was demonstrated by using architecture showed in Figure 3.3 with two simultaneous users. Noises were used in the simulation in order to perform the closely-real environment of the free-space optical system. The noise includes ASE noise, thermal noise, and shot noise with gaussian distribution where the parameter were defined in Table 3.3.

There are two channel conditions implemented in the second simulation, namely, AWGN channel and turbulence-induced fading channel. The AWGN channel was created by adding white light source with power of -130 dBm to the optical signals before transmitting through the FSO. Further, Gamma-Gamma distribution was applied to model the turbulence-induced fading channel in this simulation. Performance of the system was observed for the optimum performance in the form of minimum Log of BER and maximum Q-Factor.

Since the performance of OCDMA system is determined by several factor, one of them is input optical power, the second simulation was initiated with the analysis of the system performance for different input power of optical signals. The performance comparison was testified with modified M-sequence as signature code for input power of -15 dBm, -10 dBm, -5 dBm, and 0 dBm in two different channels, AWGN only and AWGN with medium turbulence-induced channel. Each channel was set to clear air weather conditions.

Figure 4.33 shows the performance comparison in the AWGN channel for different input power. For input power of -15 dBm, maximum distance to achieve the acceptable BER and Q-factor performance is 200 m while for -10 dBm input power the acceptable performance still can be achieved at the maximum distance of 450 m. Both input power of -5 dBm and 0 dBm achieved superior performance



for distance up to 500 m where for 0 dBm input power, the proposed system obtains relatively stable performance or low performance degradation, i.e., 1,5.

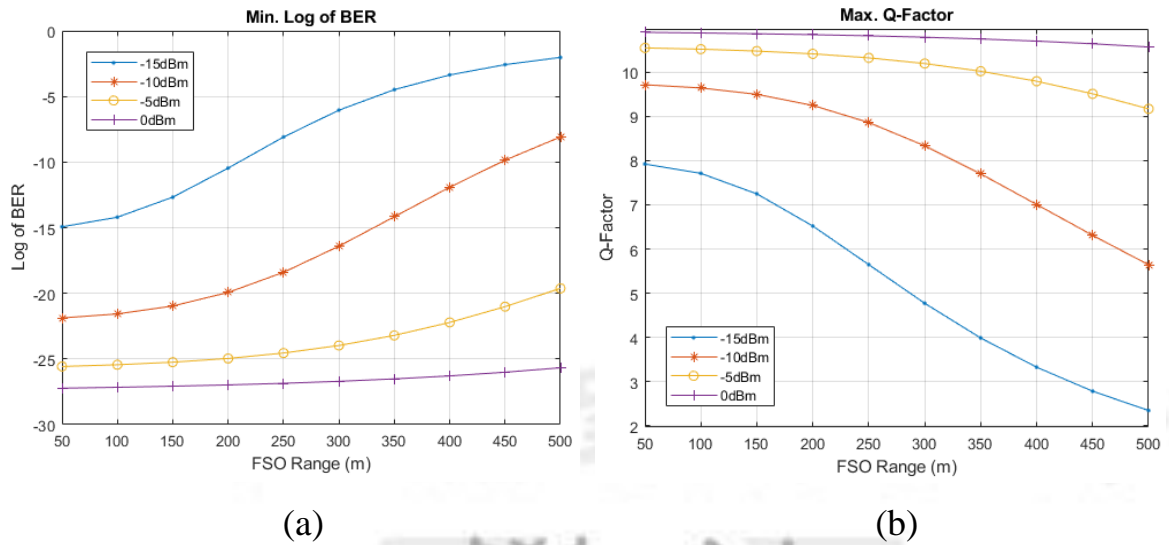


Figure 4.33 Performance of the proposed system in AWGN channel with different input power (a) Min. Log of BER, (b) Max. Q-Factor

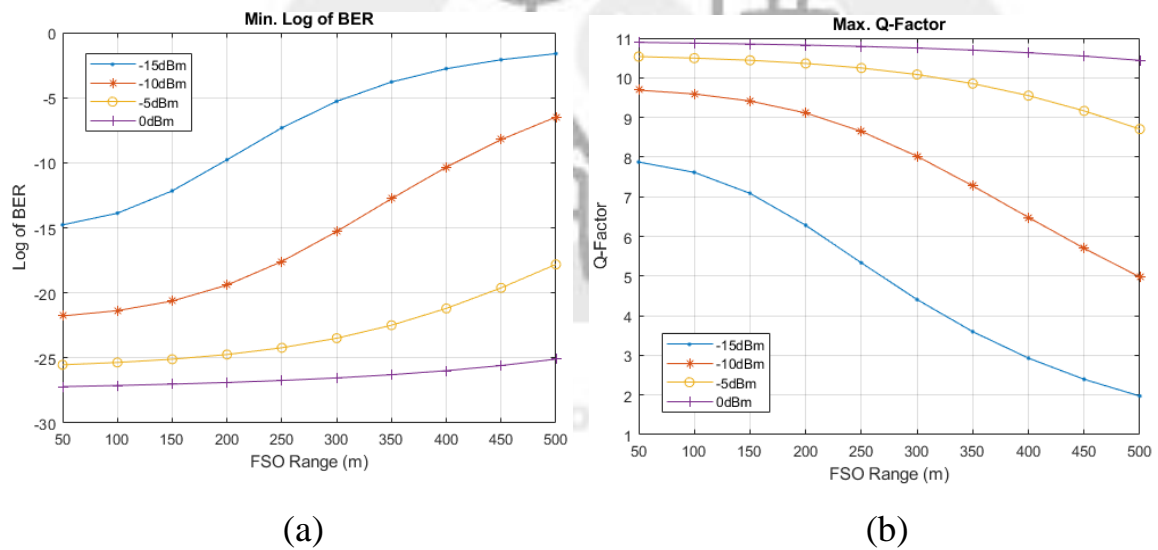


Figure 4.34 Performance of the proposed system in AWGN and turbulence-induced fading channel with different input power (a) Min. Log of BER, (b) Max. Q-Factor

Figure 4.34 displays the performance comparison in the AWGN and turbulence-induced fading channel for different input power. For input power of -15 dBm, acceptable BER and Q-factor performance can be achieved at the maximum

distance of 200 m while for -10 dBm input power, the acceptable performance can be obtained at the maximum distance of 400 m. Both input power of -5 dBm and 0 dBm achieved higher performance for distance up to 500 m. The proposed system exhibits relatively stable performance or low performance deterioration for 0 dBm input power, i.e., 2. The performance degradation for all SAC codes in the AWGN and turbulence-induced fading channel were greater compare to the performance deterioration in the AWGN only channel. Based on the simulation results displayed in Figure 4.33 and 4.34, input power of 0 dBm that imposed relatively stable performance was implemented in the proposed bipolar OCDMA system for the rest of simulation in this paper.

Since photodetector is the important component in the receiver-end of an optical system, two different types of photodetector were tested with modified M-sequence as the signature code.

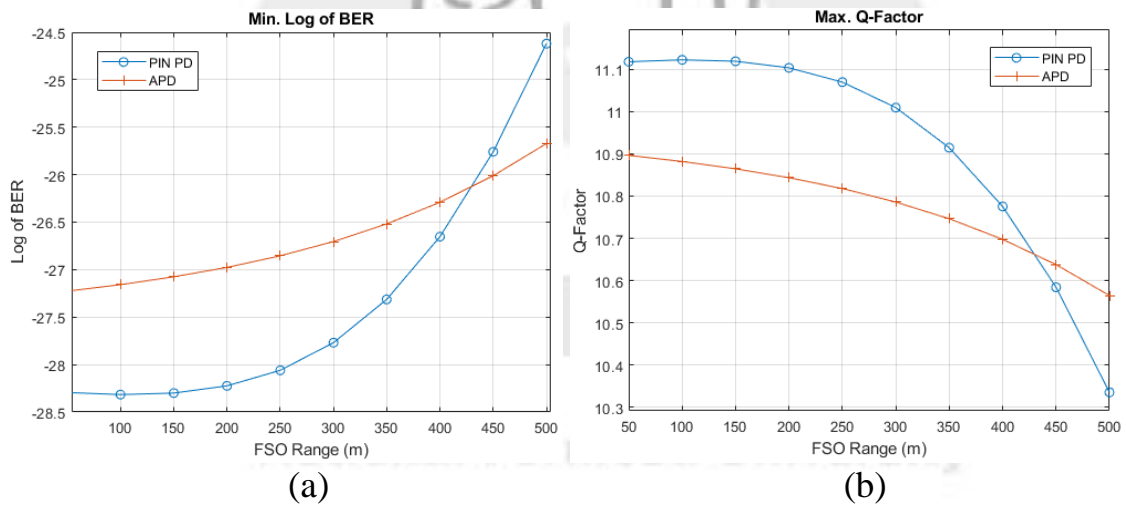


Figure 4.35 Performance of photodetector in AWGN channel (a) Min. Log of BER, (b) Max. Q-Factor

Figure 4.35 indicates the performance comparison between PIN PD and APD in the AWGN channel. For short range FSO, PIN PD exhibited the better performance compare to APD, but for medium range FSO, i.e., after 430 m, APD achieved superior performance than the PIN PD. In other words, APD more persist with the increasing of FSO distance.

Further, Figure 4.36 compare the performance between PIN PD and APD for

the AWGN and turbulence-induced fading channel. In this channel condition, PIN PD also achieved better performance for short range FSO, while for medium range FSO, APD attained the better performance. APD exceeded PIN PD performance after 400 m, verified that APD more tolerate with the increasing of FSO range compare to PIN PD, either in AWGN only or AWGN with fading channel conditions.

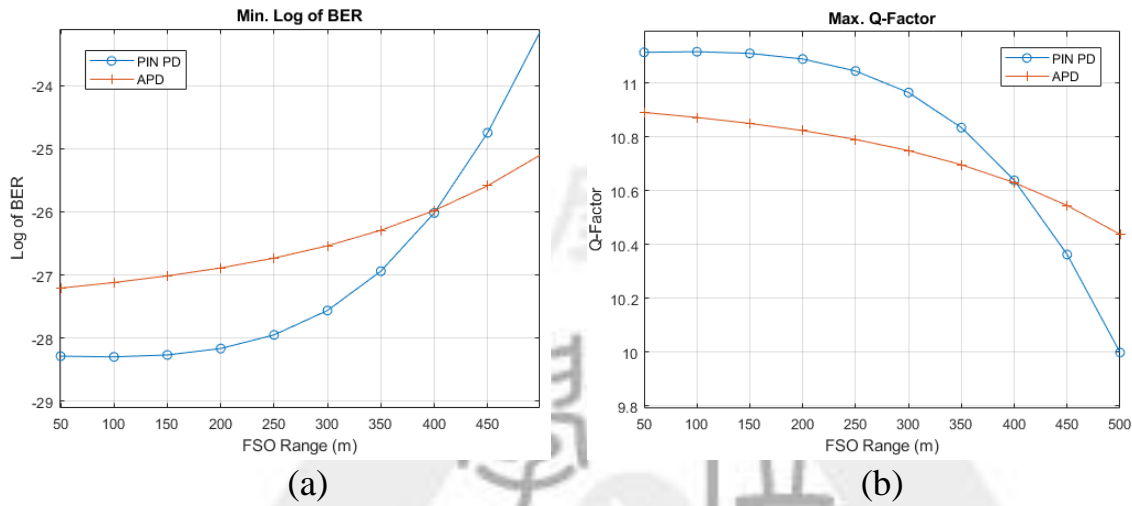


Figure 4.36 Performance of photodetector in AWGN and turbulence-induced fading channel (a) Min. Log of BER, (b) Max. Q-Factor

Based on the simulation results displayed in Figure 4.35 and 4.36, APD was chosen as photodetector in the proposed model for the rest of simulation in this paper.

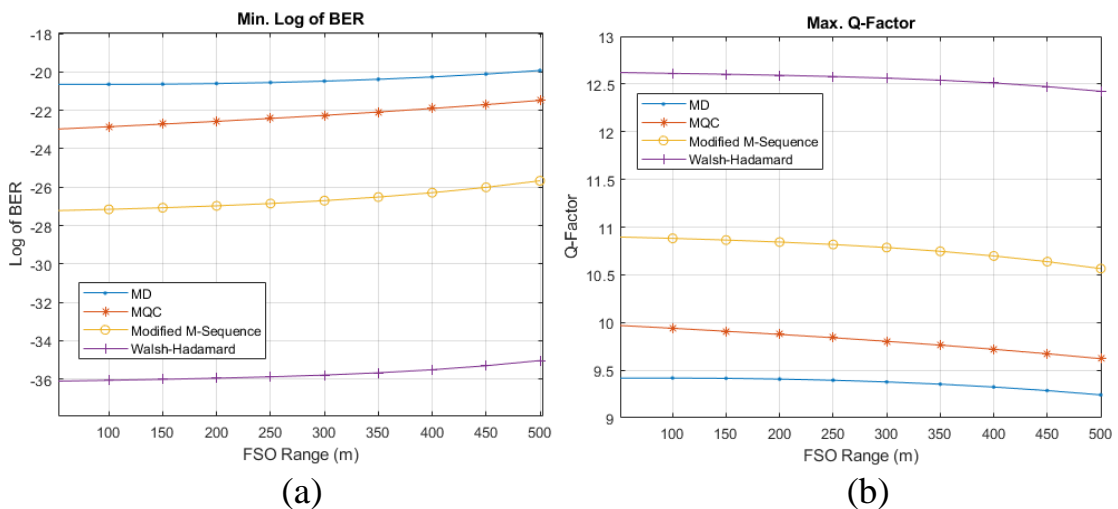


Figure 4.37 Performance of the proposed system in drizzle weather condition for AWGN channel (a) Min. Log of BER, (b) Max. Q-Factor

Farther simulation was conducted in the AWGN channel for different weather condition based on propagation data standard for the terrestrial free-space optical links design from ITU-R P.1817 [53] showed in Table 3.4. Four well-known SAC-OCDMA codes, i.e., MD code, MQC code, modified M-sequence code, and Walsh-Hadamard code were implemented in this simulation.

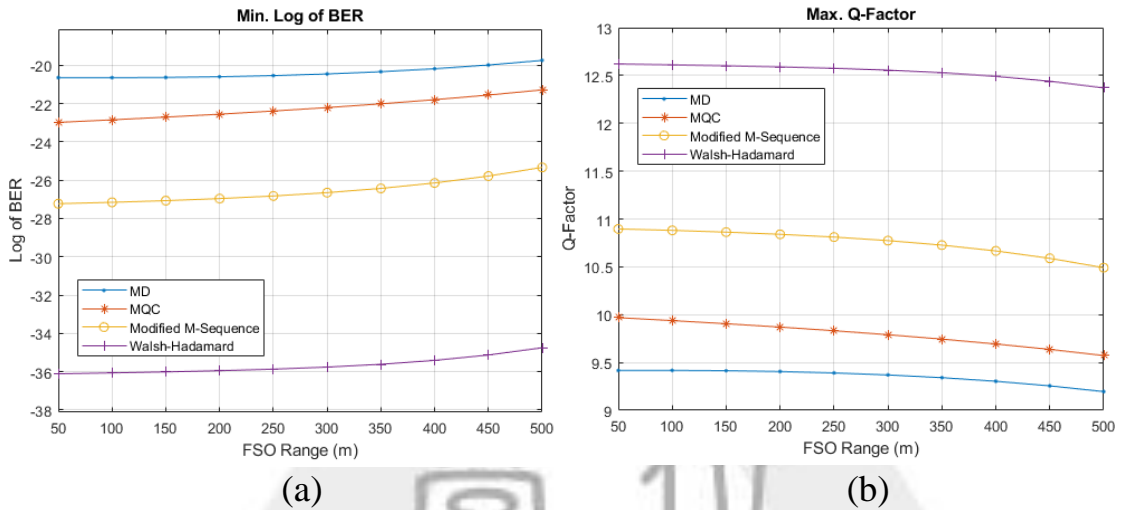


Figure 4.38 Performance of the proposed system in light rain weather condition for AWGN channel (a) Min. Log of BER, (b) Max. Q-Factor

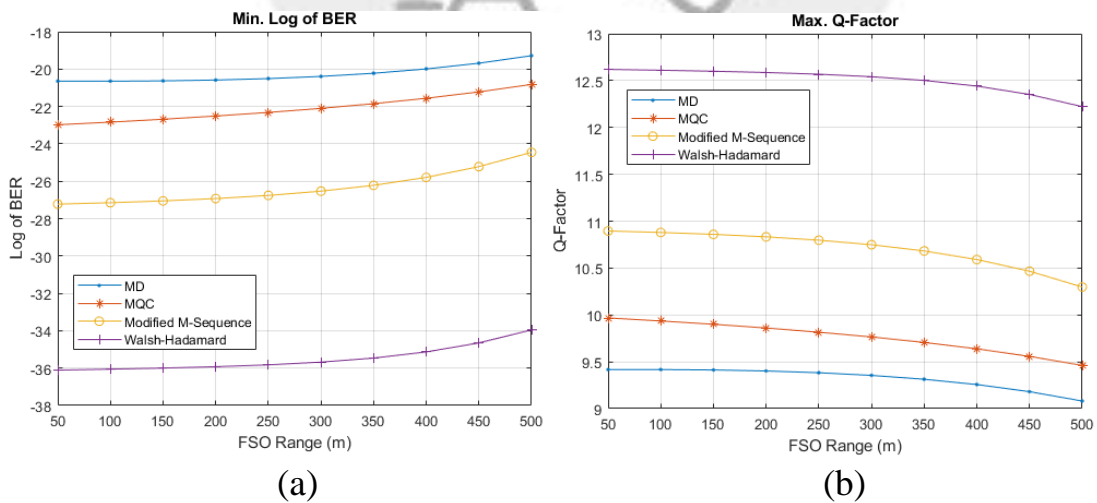


Figure 4.39 Performance of the proposed system in average rain weather condition for AWGN channel (a) Min. Log of BER, (b) Max. Q-Factor

Figure 4.37 until 4.39 presents the performance of the proposed Bi-OCDMA system for AWGN channel with four different codes in drizzle, light rain, and average rain weather conditions, respectively. In these three weather conditions,

the Bi-OCDMA system suffered relatively low performance deterioration with the increasing of FSO distance, showed in min. Log of BER and max. Q-Factor. The simulation results revealed that Walsh-Hadamard code had the best performance, followed by modified M-sequence code, MQC code, and MD code. In terms of resistance to the increasing of FSO range, MD code showed the lowest performance degradation, means that MD code more persist for the longer FSO distance application. Conversely, modified M-sequence code got the greatest impact from the increasing of FSO range.

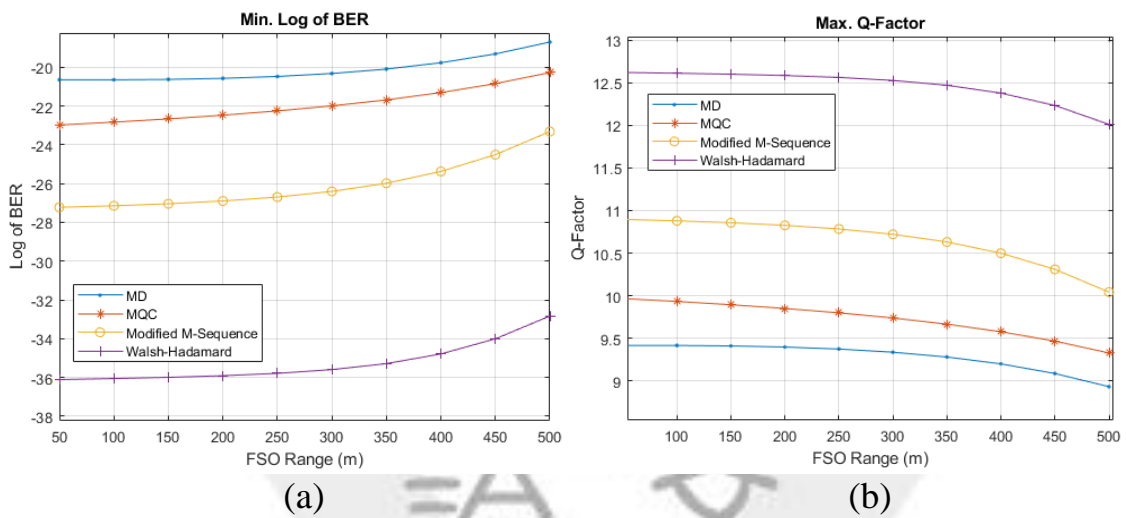


Figure 4.40 Performance of the proposed system in strong rain weather condition for AWGN channel (a) Min. Log of BER, (b) Max. Q-Factor

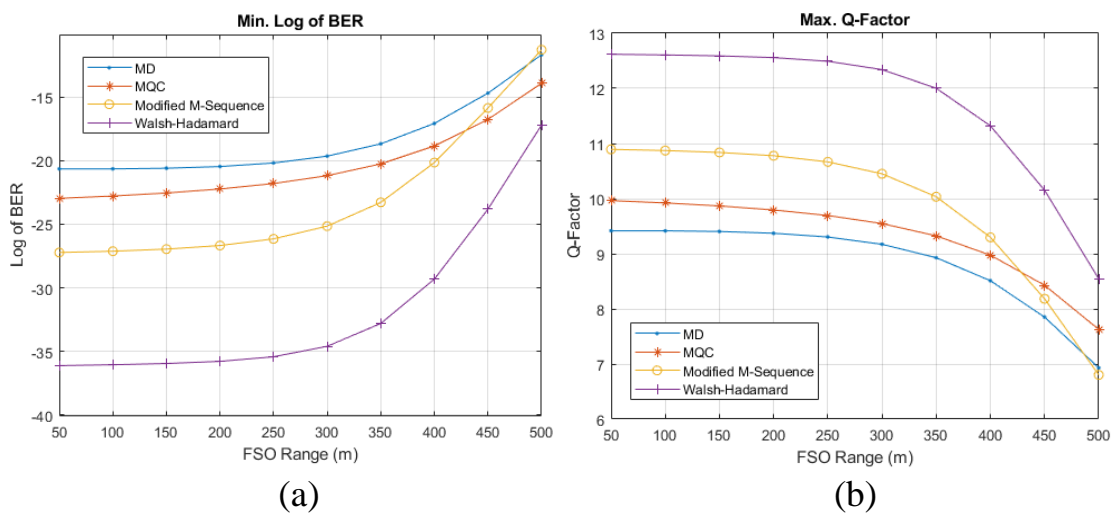


Figure 4.41 Performance of the proposed system in storm weather condition for AWGN channel (a) Min. Log of BER, (b) Max. Q-Factor

Figure 4.40 and 4.41 illustrates the performance of the proposed Bi-OCDMA system with four different codes in strong rain and storm weather conditions for AWGN channel. The simulation results illustrate that Walsh-Hadamard code obtained the best performance, followed by modified M-sequence code, MQC code, and MD code. All code suffered higher impact from these two weather conditions, especially in the storm weather. In strong rain conditions, modified M-sequence code had the worst performance degradation with the increasing of FSO range while in storm conditions, Walsh-Hadamard code suffered the worst performance deterioration. This result shows that the Walsh-Hadamard code got the greatest impact from signal attenuation because of storm condition. However, Walsh-Hadamard code still achieved the superior performance after 500 m FSO range because this code had the best performance in the proposed Bi-OCDMA scheme. In storm condition, after 430 m, modified M-sequence code worsen than MQC code and after 500 m suffered the worst performance.

The simulation results of performance degradation for different weather conditions in AWGN channel were presented in Table 4.1

Table 4.1 Performance degradation with the increasing of FSO range in AWGN channel

<b>Weather Condition</b>	<b>Code</b>	<b>Min. Log of BER (a.u.)</b>	<b>Max. Q-Factor (a.u.)</b>
Drizzle	MD	0.7183	0.17561
	MQC	1.4987	0.34863
	Modified M-Sequence	1.5545	0.3314
	Walsh-Hadamard	1.0729	0.1967
Light Rain	MD	0.9007	0.22062
	MQC	1.6977	0.39587
	Modified M-Sequence	1.8944	0.4051
	Walsh-Hadamard	1.359	0.2496
Average Rain	MD	1.3613	0.33527
	MQC	2.1599	0.5065
	Modified M-Sequence	2.7705	0.5975
	Walsh-Hadamard	2.1531	0.3973

Table 4.1 Performance degradation with the increasing of FSO range in AWGN channel (continue)

Weather Condition	Code	Min. Log of BER (a.u.)	Max. Q-Factor (a.u.)
Strong Rain	MD	1.9466	0.48296
	MQC	2.7031	0.63817
	Modified M-Sequence	3.9077	0.8524
	Walsh-Hadamard	3.2771	0.6095
Storm	MD	8.9661	2.48757
	MQC	9.0417	2.33693
	Modified M-Sequence	15.9262	4.0917
	Walsh-Hadamard	18.8968	4.07411

In addition to the AWGN effects, next simulation included turbulence-induced fading to the channel with medium turbulence condition based on (89). Simulation also conducted for different weather conditions based on Table 3.4.

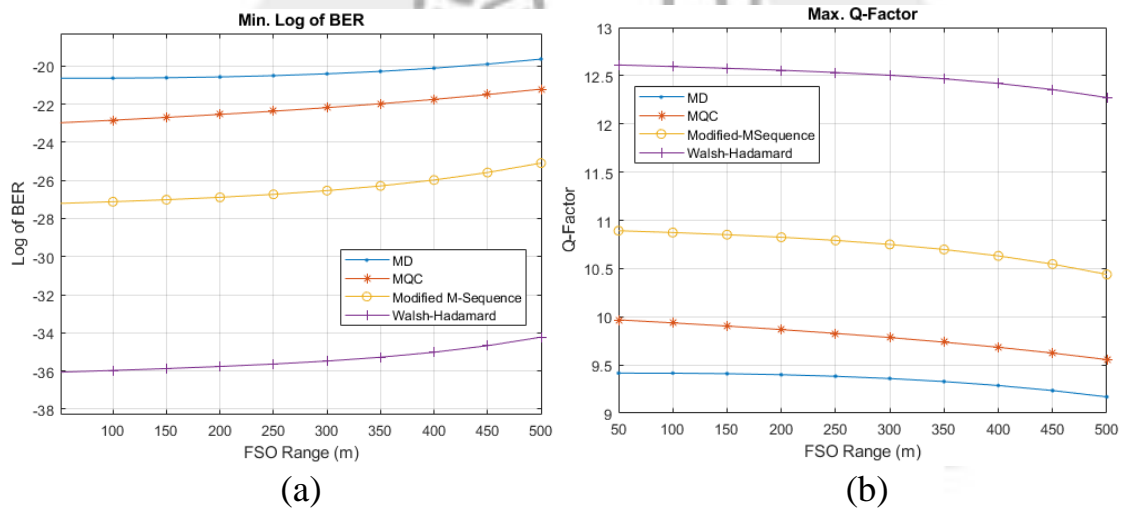


Figure 4.42 Performance of the proposed system in drizzle weather condition for AWGN and turbulence-induced fading channel (a) Min. Log of BER, (b) Max. Q-Factor

Figure 4.42 until 4.43 shows the performance of the proposed Bi-OCDMA system with four different codes in drizzle, light rain, and average rain weather conditions for AWGN and turbulence-induced fading channel. The simulation results indicate that Walsh-Hadamard code had the best performance, followed by modified M-sequence code, MQC code, and MD code. Turbulence-induced

fading impact on the higher magnitude of performance deterioration for all of codes compare to AWGN only channel.

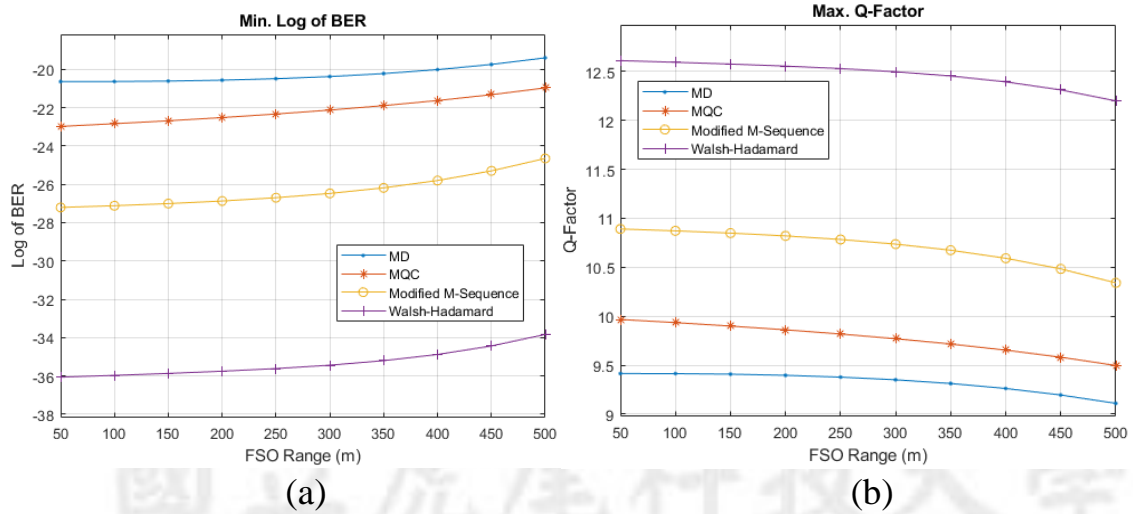


Figure 4.43 Performance of the proposed system in light rain weather condition for AWGN and turbulence-induced fading channel (a) Min. Log of BER, (b) Max. Q-Factor

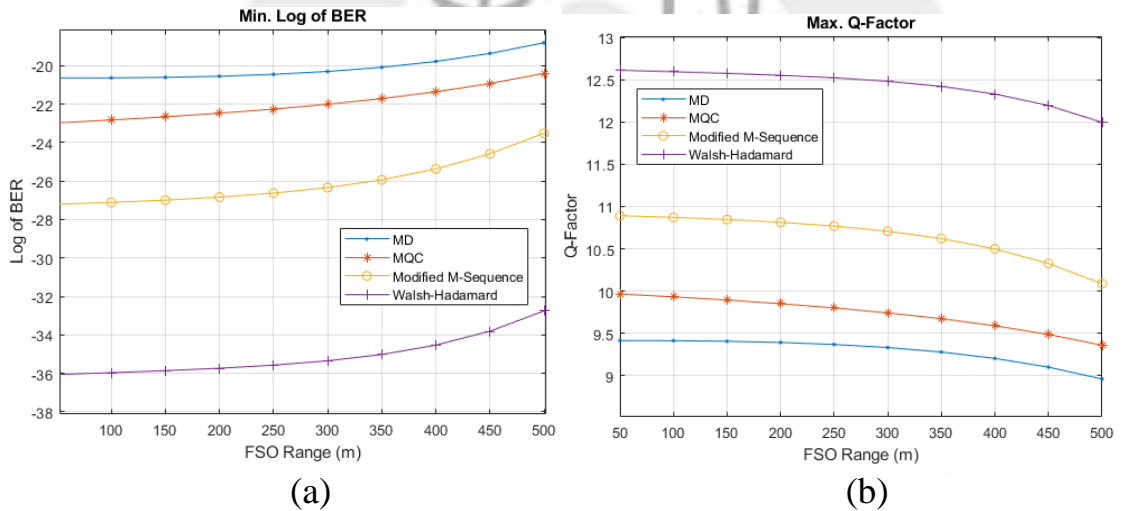


Figure 4.44 Performance of the proposed system in average rain weather condition for AWGN and turbulence-induced fading channel (a) Min. Log of BER, (b) Max. Q-Factor

Modified M-sequence code suffered the highest performance degradation with the increasing of FSO range in these three weather conditions. In other hand, MD code achieved the lowest performance degradation with the increasing of FSO distance, confirmed that MD code can be used for medium range FSO application



in this proposed Bi-OCDMA system.

Figure 4.45 and 4.46 depicts the minimum Log of BER and maximum Q-Factor achieved by each codes in strong rain and storm weather conditions for AWGN and turbulence-induced fading channel.

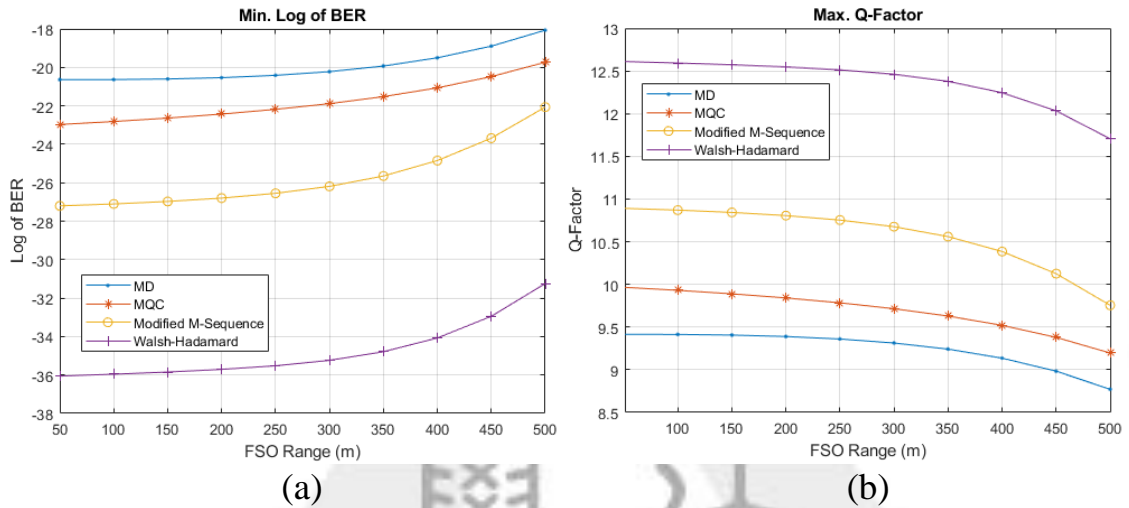


Figure 4.45 Performance of the proposed system in strong rain weather condition for AWGN and turbulence-induced fading channel (a) Min. Log of BER, (b) Max. Q-Factor

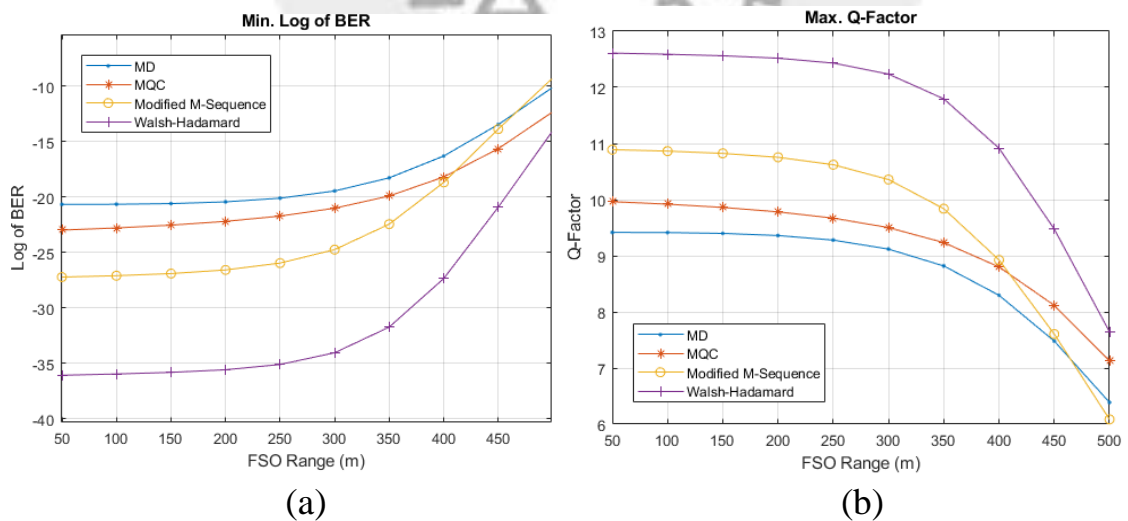


Figure 4.46 Performance of the proposed system in storm weather condition for AWGN and turbulence-induced fading channel (a) Min. Log of BER, (b) Max. Q-Factor

The simulation results indicates that Walsh-Hadamard code had the superior performance, followed by modified M-sequence code, MQC code, and MD code.

All of codes suffered from relatively high performance degradation with the increasing of FSO distance in strong rain condition and became more worst in storm condition. MD code still had the lowest performance deterioration compare to other codes in these two weather conditions.

Table 4.2 Performance degradation with the increasing of FSO range in AWGN and turbulence-induced fading channel

<b>Weather Condition</b>	<b>Code</b>	<b>Min. Log of BER (a.u.)</b>	<b>Max. Q-Factor (a.u.)</b>
Drizzle	MD	1.0025	0.24587
	MQC	1.767	0.41239
	Modified M-Sequence	2.1138	0.4531
	Walsh-Hadamard	1.8359	0.3382
Light Rain	MD	1.2379	0.30446
	MQC	2.0073	0.46985
	Modified M-Sequence	2.5563	0.5503
	Walsh-Hadamard	2.2282	0.4116
Average Rain	MD	1.8296	0.45332
	MQC	2.571	0.606
	Modified M-Sequence	3.691	0.8037
	Walsh-Hadamard	3.309	0.616
Strong Rain	MD	2.5724	0.64368
	MQC	3.2382	0.76975
	Modified M-Sequence	5.1366	1.13579
	Walsh-Hadamard	4.8101	0.9055
Storm	MD	10.5638	3.02852
	MQC	10.6674	2.8358
	Modified M-Sequence	17.96109	4.80502
	Walsh-Hadamard	22.0608	4.96498

The highest performance degradation in strong rain condition was suffered by modified M-sequence code while in storm condition, Walsh-Hadamard code experienced the worst performance degradation even though still achieve higher performance than other codes, indicates that Walsh-Hadamard code suffered great impact from optical signal attenuation in storm weather. Further, in storm

condition, after 410 m, modified M-sequence code got worsen than MQC code and after 470 m showed the worst performance among other codes.

The simulation results of performance degradation for different weather conditions in AWGN and turbulence-induced fading channel were displayed in Table 4.2

Final simulations tested the proposed Bi-OCDMA system in different turbulence conditions. Figure 4.47 until 4.49 present the performance of different SAC codes implemented in the proposed Bi-OCDMA system in different turbulence conditions based on (89).

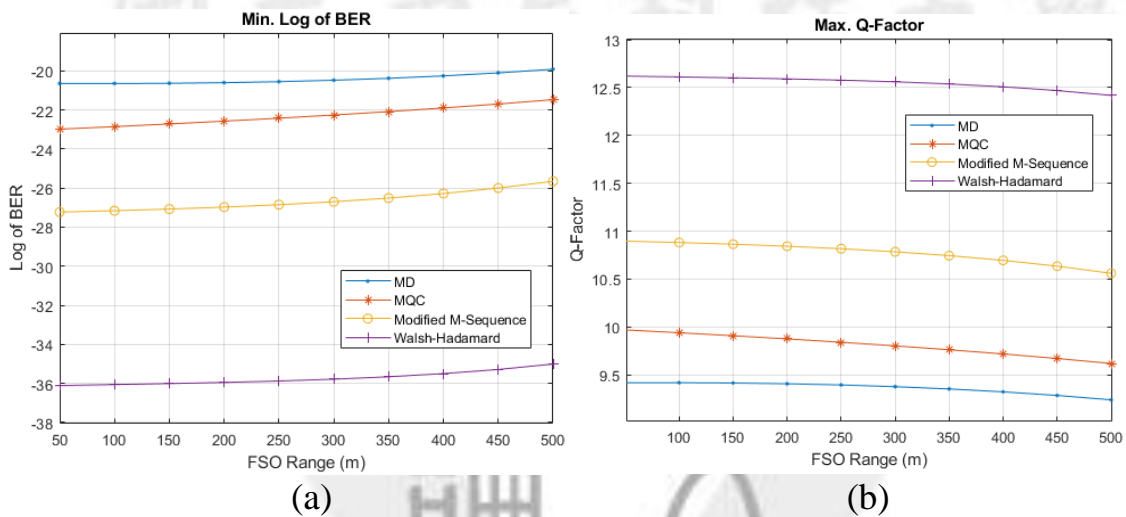


Figure 4.47 Performance of the proposed system in weak turbulence condition  
(a) Min. Log of BER, (b) Max. Q-Factor

The simulation results reveals that Walsh-Hadamard code had the best performance, followed by modified M-sequence code, MQC code, and MD code. In all turbulence conditions, MD code achieved the lowest performance degradation with the increasing of FSO range, revealed that MD code can be applied for medium distance FSO in the proposed Bi-OCDMA system. In weak and medium turbulence, simulation results indicate that modified M-sequence code suffered the worst performance deterioration with the increasing of FSO range, while in strong turbulence condition, Walsh-Hadamard code got the worst performance degradation. These results proved that the performance of modified

M-sequence code effected by the FSO range while Walsh-Hadamard code effected most by turbulence condition beside the increasing of FSO range.

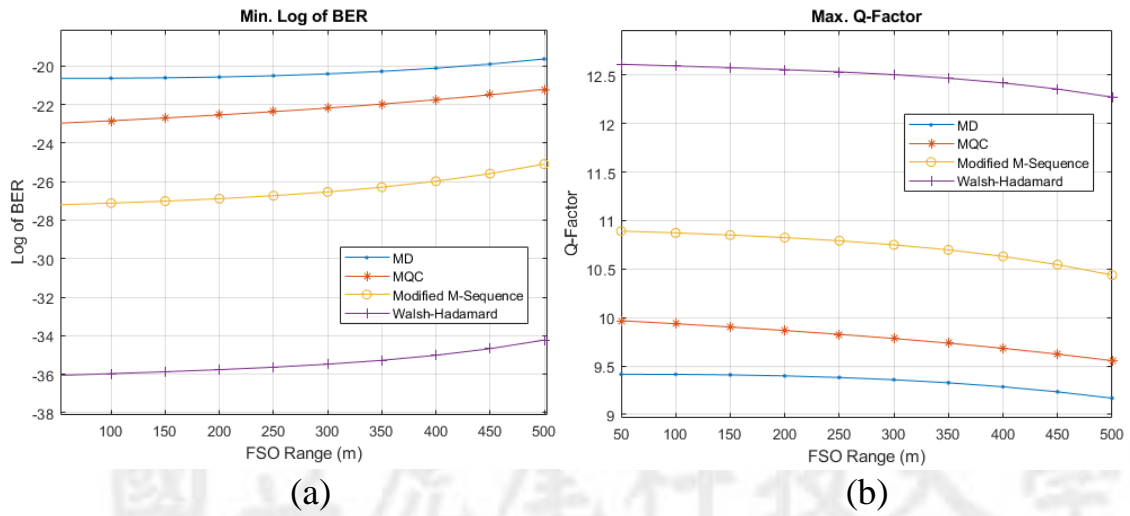


Figure 4.48 Performance of the proposed system in medium turbulence condition (a) Min. Log of BER, (b) Max. Q-Factor

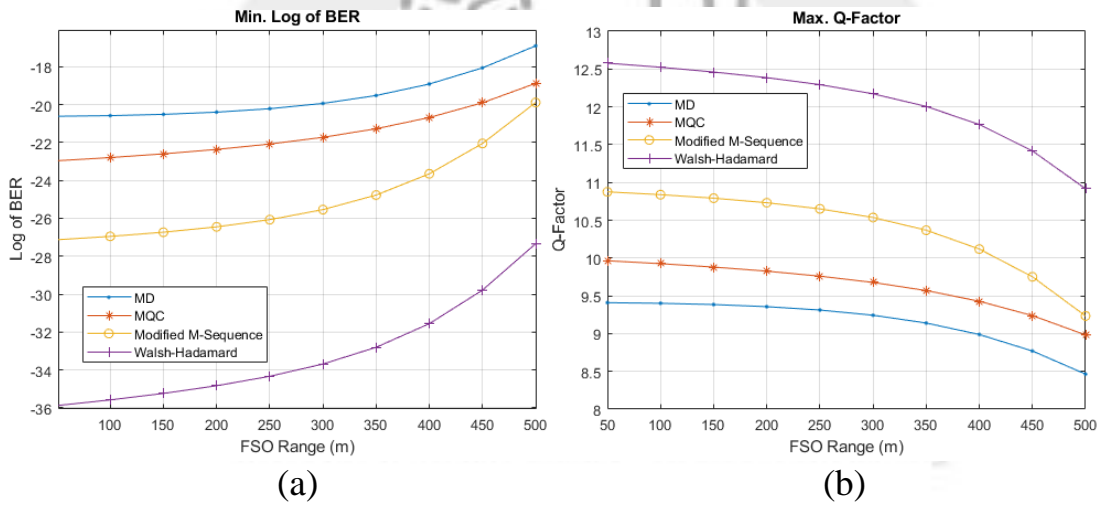


Figure 4.49 Performance of the proposed system in strong turbulence condition (a) Min. Log of BER, (b) Max. Q-Factor

The simulation results of performance degradation for different turbulence conditions were presented in Table 4.3

Table 4.3 Performance degradation with the increasing of FSO range in different turbulence condition

<b>Weather Condition</b>	<b>Code</b>	<b>Min. Log of BER (a.u.)</b>	<b>Max. Q-Factor (a.u.)</b>
Weak Turbulence	MD	0.7285	0.17811
	MQC	1.5086	0.35096
	Modified M-Sequence	1.5746	0.3357
	Walsh-Hadamard	1.1005	0.2018
Medium Turbulence	MD	1.0025	0.24587
	MQC	1.767	0.41239
	Modified M-Sequence	2.1138	0.4531
	Walsh-Hadamard	1.8359	0.3382
Strong Turbulence	MD	3.7143	0.94502
	MQC	4.0829	0.98137
	Modified M-Sequence	7.2407	1.6425
	Walsh-Hadamard	8.5379	1.6617

## Chapter 5 Conclusion

In this dissertation, the feasibility of Bipolar OCDMA system design with phase modulator for polarization coding in free-space optical channel was successfully implemented and validated. The proposed scheme increases the transmission rate compare to the previous Bi-OCDMA with optical switch and dual EOM scheme. The first simulation results verified that the proposed Bi-OCDMA could generated bipolar signals and appropriately decoded the original signal from its corresponding encoder. Since the proposed bipolar OCDMA scheme maintain the property of SAC-OCDMA, MAI elimination also proved in the simulation with mismatch decoder scenario. The balance photodetection scheme relieved the MAI in this mismatch decoder case. Second simulation measured the performance of the proposed bipolar OCDMA and were simulated in different weather condition, first for AWGN channel and second for AWGN and turbulence-induced fading channel by implementing four different OCDMA codes as signature code. The proposed Bi-OCDMA system was further applied in different turbulence condition. The initial simulation conducted for two channel conditions presents that APD was more resistance with the increasing of FSO distance compare to the PIN photodetector. Another test shows that input power of 0 dBm produced relatively stable performance with the increasing of FSO range, for both channel condition. The simulation results revealed that Walsh-Hadamard code had the best performance among others code for the proposed scheme. The simulations also exhibited that in terms of FSO range, MD code is the most resistant to the increasing of FSO distance, indicated by the lowest performance deterioration, while modified M-sequence code suffered the highest performance degradation in almost all weather and turbulence condition. These results denote that MD code can be used for medium range FSO application in the proposed Bi-OCDMA system. For the extreme weather condition, i.e., storm

condition and strong turbulence, Walsh-Hadamard code suffered the highest performance deterioration, show that Walsh-Hadamard code performance in the proposed Bi-OCDMA system was most effected by optical signal attenuation due to extreme weather and turbulence condition.

Future work can investigate the proposed Bi-OCDMA technique in the long range optical wireless channel (OWC) in correlation with different atmospheric conditions for higher multi-user scheme. Several different channel model can be implemented to testify the bipolar OCDMA performance. The performance measurement with some parameters, such as BER, Q-factor, and eye diagram can be done, including the MAI mitigation for performance improvements with several optimization techniques. Further work can observe the proposed Bi-OCDMA technique experimentally and can be investigated for higher-order intensity modulation signal with different codes.

## Reference

- [1]. G.Y. Liu and D.J. Jiang, "5G: Vision and Requirements for Mobile Communication System towards Year 2020," *Chin. J. Eng.*, pp. 1-8, 2016. (<https://doi.org/10.1155/2016/5974586>)
- [2]. M.N.O. Sadiku, S.M. Musa, and S.R. Nelatury, "Free Space Optical Communications: An Overview," *Eur. Sci. J.*, vol. 12, pp. 1857-7881, 2016. (<https://doi.org/10.19044/esj.2016.v12n9p55>)
- [3]. F. Bai, Y.W. Su, and T. Sato, "Performance Analysis of Polarization Modulated Direct Detection Optical CDMA Systems over Turbulent FSO Links Modeled by the Gamma-Gamma Distribution," *Photonics*, vol. 2, pp. 139-155, 2015. (<https://doi.org/10.3390/photonics2010139>)
- [4]. Z.-Y. Chen, L.-S. Yan, Y. Pan, L. Jiang, A.-L. Yi, W. Pan, and B. Luo, "Use of Polarization Freedom Beyond Polarization-Division Multiplexing to Support High-Speed and Spectral-Efficient Data Transmission," *Light Sci. Appl.*, vol. 6, pp. e16207, 2016. (<https://doi.org/10.1038/lsa.2016.207>)
- [5]. H.C. Cheng, E. Wijanto, T.C. Lien, P.H. Lai, and S.P. Tseng, "Multiple Access Techniques for Bipolar Optical Code Division in Wireless Optical Communications," *IEEE Access*, vol. 8, pp. 83511-83523, 2020. (<https://doi.org/10.1109/ACCESS.2020.2991071>)
- [6]. S.P. Tseng, E. Wijanto, P.H. Lai, and H.C. Cheng, "Bipolar Optical Code Division Multiple Access Techniques using a Dual Electro-Optical Modulator Implemented in Free-Space Optics Communications," *Sensors*, vol. 20, no. 12, pp. 3583, 2020. (<https://doi.org/10.3390/s20123583>)
- [7]. R.Q. Hui, M.O. Sullivan, *Fiber Optic Measurement Techniques*, Academic Press, Elsevier, United States, 2009.



- [8]. M. Chakkour, O. Aghzout, and F. Chaoui, "Theoretical Analysis of a Novel WDM Optical Long-Haul Network using the Split-Step Fourier Method," *Int. J. Opt.*, pp. 1-9, 2020. (<https://doi.org/10.1155/2020/3436729>)
- [9]. M. Singh and J. Malhotra, "A High-Speed Long-Haul Wavelength Division Multiplexing–Based Inter-Satellite Optical Wireless Communication Link using Spectral-Efficient 2-D Orthogonal Modulation Scheme," *Int J Commun Syst.*, vol. 33, pp. e4293, 2020. (<https://doi.org/10.1002/dac.4293>)
- [10]. V. Mishra, R. Upadhyay, U. Bhatt, and A. Kumar, "DEC TDMA: A Delay Controlled and Energy Efficient Clustered TDMA Mechanism for FiWi Access Network," *Optik*, vol. 164921, 2020. (<https://doi.org/10.1016/j.ijleo.2020.164921>)
- [11]. J. Zhang and A.B. Sharma, "High-Speed Optical Time-Division Multiple-Access (OTDMA) Networks using Optical Signal Processing," *Photonic Netw. Commun.*, vol. 1, pp. 273–285, 1999. (<https://doi.org/10.1023/A:1010070632272>)
- [12]. M. Moghaddasi, G. Mamdoohi, A.S.M. Noor, M.A. Mahdi, and S.B.A. Anas, "Development of SAC–OCDMA in FSO with multi-wavelength laser source," *Opt. Commun.*, vol. 356, pp. 282-289, 2015. (<https://doi.org/10.1016/j.optcom.2015.07.075>)
- [13]. S.A.A. Mottaleb, H. Fayed, A. Aziz, and M. Aly, "Enhanced Spectral Amplitude Coding OCDMA System Utilizing a Single Photodiode Detection," *Appl. Sci.* vol. 8, no. 10, pp. 1861, 2018.
- [14]. S. Thakur and A. Shah, "A Systematic Review on OCDMA Network Having Different Detection Techniques," *Int. J. Adv. Sci. Technol.*, vol. 29, no. 10s, pp. 1509 – 1513, 2020.
- [15]. A. Aissaoui and L. Hacini, "Performance Comparison of Different SAC-OCDMA-FSO Detection Techniques in Presence of Atmospheric Losses," in *6th International Conference on Image and Signal Processing and their*

- Applications (ISPA)*, Mostaganem, Algeria, 2019, pp. 1-5.  
(<https://doi.org/10.1109/ISPA48434.2019.8966876>)
- [16]. S. Boukricha, K. Ghoumid, S. Mekaoui, E. Ar-Reyouchi, H. Bourouina, and R. Yahiaoui, "SAC-OCDMA System Performance using Narrowband Bragg Filter Encoders and Decoders," *SN Appl. Sci.*, vol. 2, no. 1002, 2020.  
(<https://doi.org/10.1007/s42452-020-2700-9>)
- [17]. A.O. Aldhaibani, S.A. Aljunid, M.S. Anuar, and A.R. Arief, "Increasing Performance of SAC-OCDMA by Combine OFDM Technique," *J Theor Appl Inf Technol*, vol. 66, no. 2, pp. 2005-2014, 2014.
- [18]. X. Wang, N. Wada, T. Hamanaka, T. Miyazaki, G. Cincotti, and K. Kitayama, "OCDMA over WDM Transmission," in *9th International Conference on Transparent Optical Networks*, Rome, Italy, 2007, pp. 110-113. (<https://doi.org/10.1109/ICTON.2007.4296043>)
- [19]. U. Bhanja and C. Panda, "Performance Analysis of Hybrid SAC-OCDMA-OFDM Model over Free-space Optical Communication," *CCF Trans. Netw.*, vol. 3, pp. 272-285, 2020. (<https://doi.org/10.1007/s42045-020-00039-6>)
- [20]. S.J. Park, B.K. Kim, and B. Kim, "An OCDMA Scheme to Reduce Multiple Access Interference and Enhance Performance for Optical Subscriber Access Networks," *ETRI J*, vol. 24, no. 1, pp. 13-20, 2004.  
(<https://doi.org/10.4218/etrij.04.0103.0002>)
- [21]. P.T. Dat, A. Kanno, K. Inagaki, T. Umezawa, N. Yamamoto, and T. Kawanishi, "Hybrid Optical Wireless-mmWave: Ultra High-Speed Indoor Communications for Beyond 5G," *IEEE Conference on Computer Communications Workshops*, Paris, France, 2019, pp. 1003-1004.  
(<https://doi.org/10.1109/INFCOMW.2019.8845283>)
- [22]. D. Nguyen, J. Bohata, J. Spacil, D. Dousek, M. Komanec, S. Zvanovec, Z. Ghassemlooy, and B. Ortega, "M-QAM Transmission over Hybrid Microwave Photonic Links at the K-Band," *Opt. Express*, vol. 27, pp. 33745-33756, 2019.

- [23]. S.P. Patel and S. Gupta, "Novel Bipolar Reconfigurable Code for OCDMA Network," *Int. J. Adv. Eng. Res. Dev.*, vol. 5, pp. 493-500, 2018.
- [24]. H.M.R. Al-Khafaji, S.A. Aljunid, and H.A. Fadhil, "Spectral Efficiency Comparison of SAC-OCDMA Systems using Unipolar and Bipolar Encoding Techniques," in *2nd International Conference on Photonics*, Kota Kinabalu, Malaysia, 2011, pp. 1-5. (<https://doi.org/10.1109/ICP.2011.6106822>)
- [25]. M.R. Zefreh and J.A. Salehi, "Theoretical Studies of Ultrashort Light Pulse Spectrally-Phase-Encoded OCDMA System Using Power-Cubic Optical Nonlinear Preprocessor," *IEEE J. Light. Technol.*, vol. 33, pp. 5062-5072, 2015. (<https://doi.org/10.1109/JLT.2015.2495334>)
- [26]. H. Al-Khafaji, R. Ngah, S. Aljunid, and T. Rahman, "A New Two-Code Keying Scheme for SAC-OCDMA Systems Enabling Bipolar Encoding," *J Mod Opt*, vol. 62, no. 5, pp. 327-335, 2015. (<https://doi.org/10.1080/09500340.2014.978914>)
- [27]. C.T. Yen and W. Chen, "A Study of Bipolar Walsh-Hadamard Coding Method in Optical CDMA Networks," *Appl. Mech. Mater.*, vol. 284-287, pp. 2667-2671, 2013. (<https://doi.org/10.4028/www.scientific.net/AMM.284-287.2667>)
- [28]. H.M.R. Al-Khafaji, S.A. Aljunid, and H.A. Fadhil, "Spectral Efficiency Analysis of Bipolar Spectral Amplitude Coding Optical Code-Division Multiple Access Systems using Different One-Dimensional Codes," *IET Optoelectron.*, vol. 6, pp. 215-222, 2012. (<https://doi.org/10.1049/iet-opt.2011.0051>)
- [29]. S. Gupta and A. Goel, "New Bipolar Spectral Amplitude Code for Cardinality Enhancement in OCDMA Network," *J Opt*, vol. 49, no. 9, pp. 1-8, 2020. (<https://doi.org/10.1007/s12596-020-00589-4>)
- [30]. M. Cha, R. Yen, K. Dimiyati, and M. Abdullah, "Using Bipolar Codes in Non-coherent Optical CDMA Systems to Stabilize Decision Threshold for

- BER Performance Improvement,” *J. Opt. Commun.*, vol. 27, no. 6, pp. 324-328, 2006. (<https://doi.org/10.1515/JOC.2006.27.6.324>)
- [31]. S. Tseng, "A New Polarization-SAC Scheme Suitable for Compact OCDMA-FSO Networks," *IEEE Systems Journal*, vol. 13, no. 2, pp. 1332-1335, 2019. (<https://doi.org/10.1109/JSYST.2018.2875042>)
- [32]. Y.-T. Chang, S.-P. Tseng, B.-R. Huang, K.-X. Zhang, and H.-C. Cheng, “Experiment of Wireless Optical Communication Applied to Hybrid SAC/PDM OCDMA Scheme with FBG-Based Fiber Lasers,” *Opt Laser Technol*, vol. 105, pp. 288-305, 2018. (<https://doi.org/10.1016/j.optlastec.2018.03.007>)
- [33]. Y. Chang, C. Shao, B. Huang, and H. Cheng, "Experimental Investigation of SAC/PDM-Based OCDMA Scheme with FBG-Based Lasers over Wireless Transmission Channel," in *International Workshop on Fiber Optics in Access Network (FOAN)*, Brno, Czech Republic, 2015, pp. 17-21. (<https://doi.org/10.1109/FOAN.2015.7318292>)
- [34]. J.F. Huang, C.T. Yen, and B.H. Chen, “Optical CDMA with Embedded Spectral-Polarization Coding over Double Balanced Differential-Detector,”. *Lecture Notes of the Institute for Computer Sciences, Social Informatics and Telecommunications Engineering*, vol 6, Springer, Berlin, Heidelberg, 2009. ([https://doi.org/10.1007/978-3-642-04648-3\\_33](https://doi.org/10.1007/978-3-642-04648-3_33))
- [35]. C.T. Yen, “Optical Code-Division Multiple-Access Embedded with a Polarisation Diversity Scheme for Radio-over-Fibre Transmissions,” *Optoelectronics, IET*, vol. 6, pp. 131-139, 2012. (<https://doi.org/10.1049/iet-opt.2010.0074>)
- [36]. M. Morant, J. Pérez, and R. Llorente, "Polarization Division Multiplexing of OFDM Radio-over-Fiber Signals in Passive Optical Networks," *Adv. Opt. Technol.*, vol. 2014, 2014. (<https://doi.org/10.1155/2014/269524>)
- [37]. Z. Gao, X. Wang, N. Kataoka, and N. Wada, “Rapid Reconfigurable OCDMA System using Single-Phase Modulator for Time-Domain Spectral

- Phase Encoding/Decoding and DPSK Data Modulation,” *J. Light. Technol.*, vol. 29, no. 3, pp. 348-354, 2011. (<https://doi.org/10.1109/JLT.2010.2093558>)
- [38]. X. Wang, Z.S. Gao, N. Kataoka, and N. Wada, “Time Domain Spectral Phase Encoding/DPSK Data Modulation using Single Phase Modulator for OCDMA Application,” *Opt. Express*, vol. 18, no. 9880-91, 2010. (<https://doi.org/10.1364/OE.18.009879>)
- [39]. J.F. Huang, C.C. Yang, and I.M. Chiu, “Hybrid MQC/*M*-Matrices Coding over Non-Coherent Spectral/Spatial Optical CDMA Networks,” *International Journal of Microwave and Optical Technology*, vol. 1, no. 2, pp. 592-595, 2006.
- [40]. Z. Wei, H.M.H. Shalaby, and H.G. Shiraz, "Modified Quadratic Congruence Codes for Fiber Bragg-Grating-Based Spectral-Amplitude-Coding Optical CDMA Systems," *J. Light. Technol.*, vol. 19, no. 9, pp. 1274-1281, 2001. (<https://doi.org/10.1109/50.948274>)
- [41]. I.A.M. Ashour, H.M.H. Shalaby, S. Shaari, and P.S. Menon, "Simulation of MQC Code of SAC/Optical CDMA and WDM Hybrid Overlay System," in *Fourth International Conference on Modeling, Simulation and Applied Optimization*, Kuala Lumpur, Malaysia, 2011, pp. 1-5. (<https://doi.org/10.1109/ICMSAO.2011.5775501>)
- [42]. J.F. Huang, C.C. Yang, and S.P. Tseng, “Complementary Walsh–Hadamard Coded Optical CDMA Coder/Decoders Structured over Arrayed-Waveguide Grating Routers,” *Opt. Commun.*, vol. 229, no. 1, pp. 241-248, 2004. (<https://doi.org/10.1016/j.optcom.2003.11.007>)
- [43]. C.C. Yang, J.F. Huang, and S.P. Tseng, “Optical CDMA Network Codes Structured with M-sequence Codes over Waveguide-Grating Routers,” *IEEE Photon. Technol. Lett.*, vol. 16, no. 2, pp. 641-643, 2004. (<https://doi.org/10.1109/LPT.2003.823089>)

- [44]. T. Abd, S.A. Aljunid, H.A. Fadhil, R.B. Ahmad, and M.N.M. Saad, "Design and Simulation a New Code with Zero Cross-Correlation for SAC-OCDMA Networks," *Aust. J. Basic & Appl. Sci*, vol. 6, no. 3, pp. 112-119, 2012.
- [45]. M. Motealleh and M. Mohsen, "Simulation of a SAC-OCDMA 10 User  $\times$ 15 Gb/s System Using MD Code," *International Journal of Optics and Applications*, vol. 4, no. 1, pp. 20-26, 2014. (<https://doi.org/10.5923/j.optics.20140401.04>)
- [46]. R. Fayadh, M. Wali, and M. Bonneya, "Establishment Network by Using FSO Link Based on MD Code for Hybrid SCM-SAC-OCDMA Wireless System," *Int. J. Electr. Comput. Eng.*, vol. 8, no. 6, pp. 5107, 2018. (<https://doi.org/10.11591/ijece.v8i6.pp5107-5117>)
- [47]. S. Rana and A. Gupta, "Performance of Different OCDMA Codes with FWM and XPM Nonlinear Effects," *J. Opt. Commun.*, vol. 38, no. 3, 2016. (<https://doi.org/10.1515/joc-2016-0093>)
- [48]. S. Kaur and S. Singh, "Review on Developments in All-Optical Spectral Amplitude Coding Techniques," *Opt. Eng.*, vol. 57, no. 1, 2018. (<https://doi.org/10.1117/1.OE.57.11.116102>)
- [49]. H. Al-Khafaji, R. Ngah, S. Aljunid, and T. Rahman, "A New Two-Code Keying Scheme for SAC-OCDMA Systems Enabling Bipolar Encoding," *J Mod Opt*, vol. 62, no. 5, pp. 327-335, 2015. (<https://doi.org/10.1080/09500340.2014.978914>)
- [50]. C.-T. Yen, H.-C. Cheng, Y.-T. Chang, and W.-B. Chen, "Performance Analysis of Dual Unipolar/Bipolar Spectral Code in Optical CDMA Systems," *J. Appl. Res. Technol.*, vol. 11, pp. 235-241, 2013. ([https://doi.org/10.1016/S1665-6423\(13\)71533-5](https://doi.org/10.1016/S1665-6423(13)71533-5))
- [51]. H. Mrabet, S. Mhatli, I. Dayoub, and E. Giacoumidis, "Performance Analysis of AO-OFDM-CDMA with Advanced 2D-Hybrid Coding for

Amplifier-Free LR-PONs,” *IET Optoelectron.*, vol. 12, 2018.  
(<https://doi.org/10.1049/iet-opt.2018.5042>)

[52]. N. Dong-Nhat, M.A. Elsherif, and A. Malekmohammadi, “Investigations of High-Speed Optical Transmission Systems Employing Absolute Added Correlative Coding (AACC),” *Opt. Fiber Technol.*, vol. 30, pp. 23–31, 2016.

[53]. International Telecommunication Union, *Propagation data required for the design of terrestrial free-space optical links*, P Series Radiowave propagation, P.1817-1, 2012.

國立虎尾科技大學



National Formosa University

# **Design of Bipolar Optical Code Division Multiple Access Techniques Using Phase Modulator for Polarization Coding in Wireless Optical Communication**

無線光通信中使用相位調製器極化編碼的雙極光碼  
分多址技術的設計

Student : Eddy Wijanto

Advisor : Prof. Hsu-Chih Cheng  
Prof. Chun-Ming Huang

Department of Electro-Optical Engineering  
National Formosa University

## **Abstract**

In this dissertation, bipolar optical code division multiple access (Bi-OCDMA) scheme was proposed by using phase modulator to realize the polarization coding through the free-space optical channel. The proposed scheme based on the spectral amplitude coding (SAC) technique. First simulation aims to prove the feasibility of bipolar scheme of the proposed structure by utilizing modified maximal-length (M)-sequence as signature code. The initial simulation results exhibit that the proposed Bi-OCDMA system could be implemented in the free-space optical communication. The structure of the proposed system alleviates the multiple access interference (MAI). The second simulation observed the performance of several different well-known SAC codes, i.e., modified quadratic congruence (MQC) code, multi-diagonal (MD) code, modified M-sequence code, and Walsh-Hadamard code, with the proposed Bi-OCDMA architecture for two users in different weather conditions, both for additive white Gaussian noise (AWGN) and turbulence-induced fading channel. The simulations results indicated that Walsh-Hadamard code has the superior performance among others code.

Keywords: bipolar, free-space optical communication, multiple access interference (MAI), optical code division multiple access (OCDMA), phase modulator, polarization coding



# Chapter 1 Introduction

The fifth generation (5G) network demands become challenging with the significantly increasing of complexity. Due to its high reliability, low latency, high bandwidth, accurate synchronization, and flexible application, optical network is one of the promising technologies to meet the increasing demands of the upcoming 5G technology. Free-space optical (FSO) communication has become one of the preferable methods with comparable data rate and very low error rate compare to the optical fiber cable, although the biggest challenge is power attenuation due to the atmospheric turbulence under various weather conditions.

Another technical aspect in the real environment is the multiple access technology. Optical code division multiple access (OCDMA) gets increasing attention in the field of optical communication due to its asynchronous transmission, flexibility, security, and scalability. Among OCDMA technologies, spectral amplitude coding (SAC) is proposed to minimize the effect of multiple access interference (MAI) and relieve the impact of phase induced intensity noise (PIIN) with fixed in phase cross-correlation.

In the demodulation scheme of optical signals, OCDMA can be categorized into two categories, non-coherent and coherent OCDMA. The commonly used encoding method in non-coherent OCDMA is unipolar encoding. Meanwhile, the coherent systems utilize bipolar coding with the advantages in spectral efficiency. The performance of bipolar encoding is better than the unipolar encoding.

## Chapter 2 Simulation Design

Figure 1 depicts the design of the bipolar OCDMA (Bi-OCDMA) encoder with phase modulator scheme proposed in this dissertation. First, two continues wave (CW) laser arrays are employed to emit wavelengths according to the assigned modified maximal-length (M)-sequence codeword, where CW laser array#1 (or #2) sends out the wavelength correlated with chip “1” of the codeword. Since the modified M-sequence codeword  $X_1 = [1\ 0\ 1\ 1\ 1\ 0\ 0\ 0]$  is assigned to

user#1, the wavelengths of CW laser array#1 and #2 are  $(\lambda_1, \lambda_3, \lambda_4, \lambda_5)$  and  $(\lambda_2, \lambda_6, \lambda_7, \lambda_8)$ , respectively.

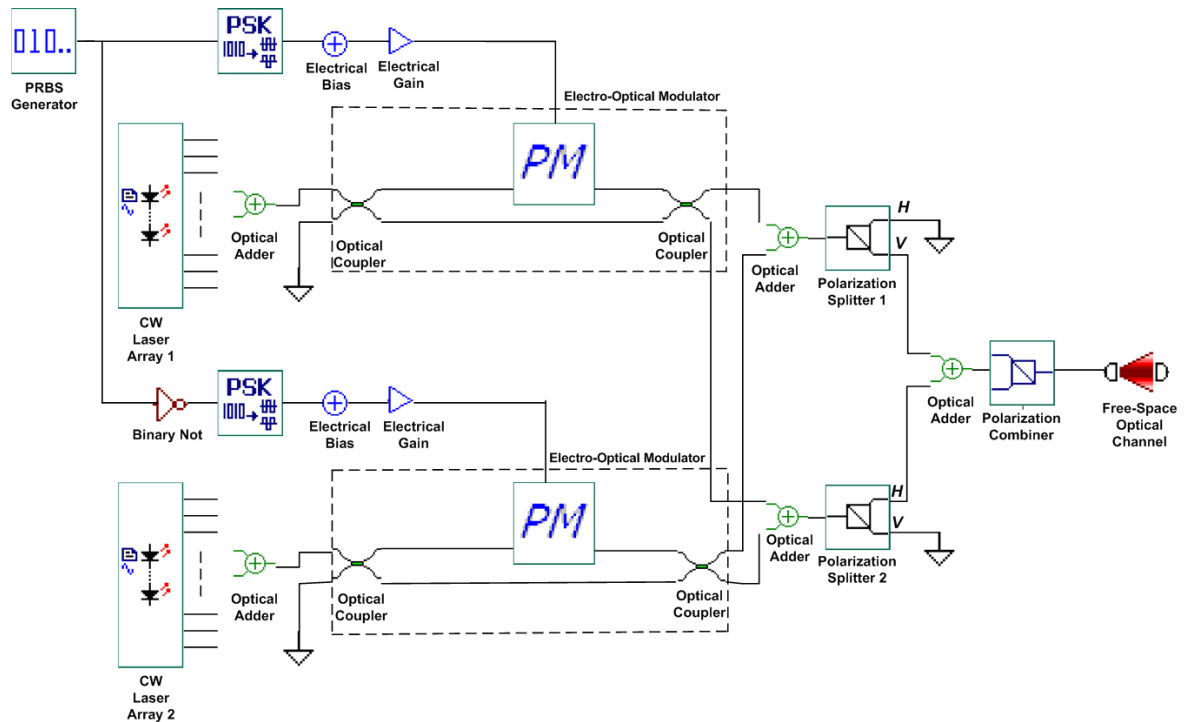


Figure 1. Proposed Bi-OCDMA encoder with phase modulator scheme

When the data bit of “0” (or “1”) is sent, only the first (or second) output of optical couplers will have the signals and pass into the upper (or lower) polarization splitter to polarize the signals into vertical (or horizontal) polarization state. Then, these polarized signals are combined through the polarization combiner. Finally, the output from the encoder is transmitted via a FSO channel.

Figure 2 displays the structure of the proposed Bi-OCDMA decoder. The received optical signals are depolarized through the polarization splitter and then are sent to the following two circulators, each of port#2 are connected to two series of fiber Bragg gratings (FBGs), respectively. The wavelengths of these two series of FBGs are determined by the assigned codewords. The reflected signals subsequently enter port#3 of the circulator, while the transmitted signals of the two series of FBGs are collected into the upper optical adder. The optical signals from each of port#3 from two optical circulators are gathered by the lower optical adder.

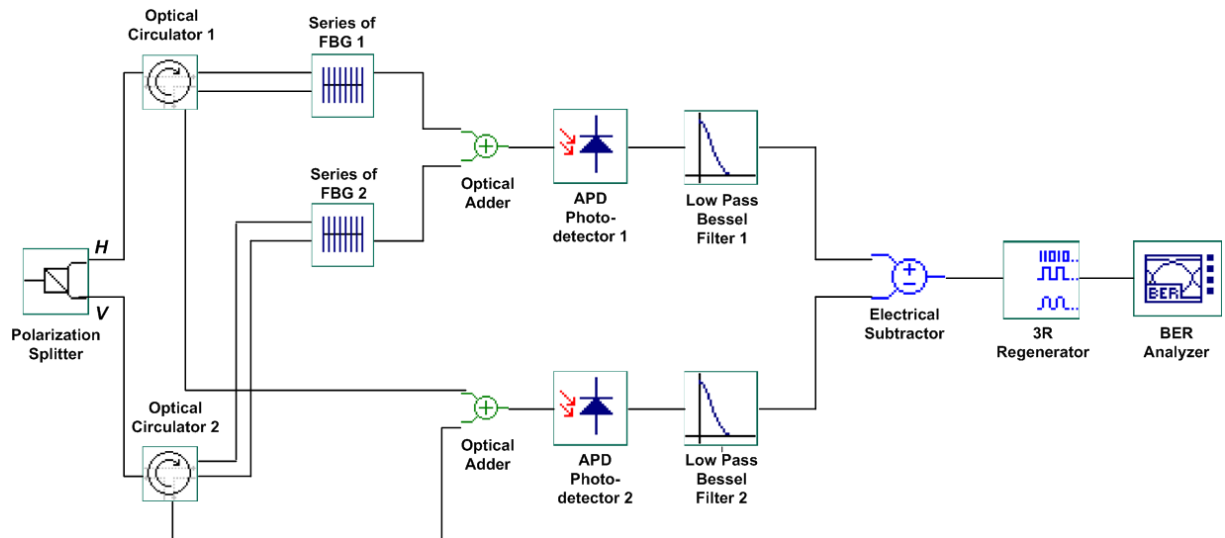


Figure 2. Proposed Bi-OCDMA decoder with phase modulator scheme

## Chapter 3 Simulation Results

Figure 3 shows the observed spectra before the optical signals passed to the upper and lower photodetector in case of data bit “0” was sent.

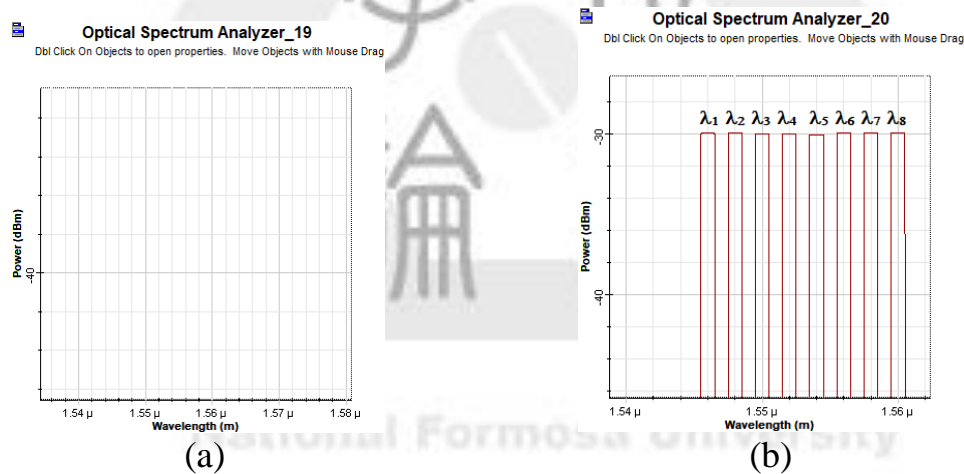


Figure 3. Output spectra before photodetection when bit “0” was transmitted (a) Total signals at upper branch, (b) Total signals at lower branch

Wavelength of  $\lambda_1, \lambda_3, \lambda_4, \lambda_5$  with horizontal polarization were reflected by first series of FBG to the lower branch while  $\lambda_2, \lambda_6, \lambda_7, \lambda_8$  were reflected by second series of FBG to the lower branch. From Figure 3(a) and (b), no spectral chip at the upper branch and eight spectral chips were appeared at the lower branch, the electrical subtraction between upper and lower branch resulted in negative signal

amplitude, represents the negative parts “-1” of the bipolar scheme.

Figure 4 depicts the performance of Bi-OCDMA system in storm weather conditions for additive white Gaussian noise (AWGN) and turbulence-induced fading channel. The simulation results indicates that Walsh-Hadamard code had the superior performance.

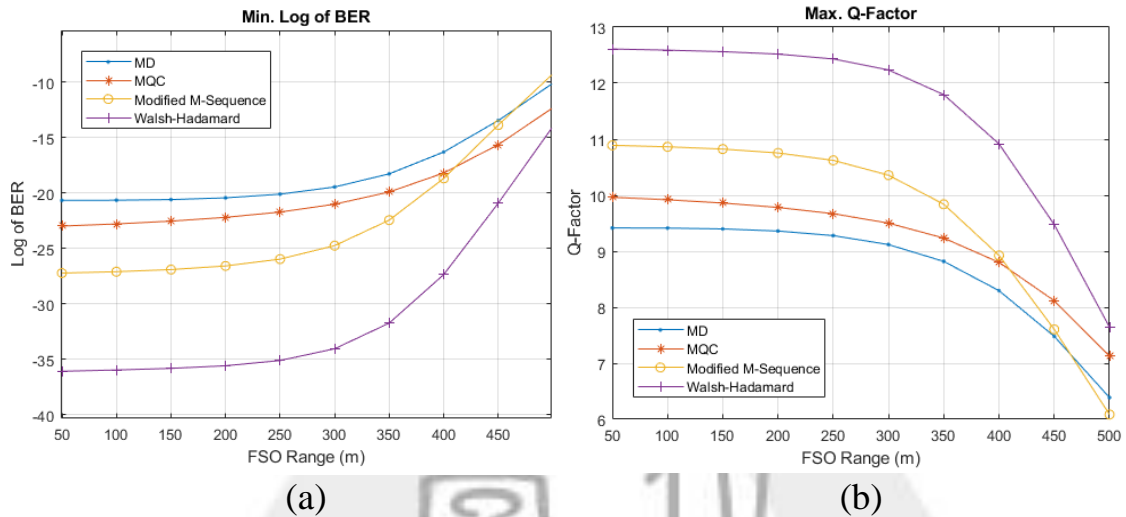


Figure 4. Performance of the proposed system in storm weather condition for AWGN and turbulence-induced fading channel (a) Min. Log of BER, (b) Max. Q-Factor

## Chapter 4 Conclusions

In this dissertation, the feasibility of Bi-OCDMA with phase modulator scheme for polarization coding in free-space optics environments with short to medium range was successfully implemented and validated. The proposed system was designed based on the SAC-OCDMA techniques that theoretically relieve the MAI effect. The performance measurements were simulated in different weather condition, first for AWGN channel and second for AWGN and turbulence-induced fading channel by utilizing four different OCDMA codes.